Republic of Iraq
Ministry of Higher Education
and Scientific Research
University of Babylon
College of Engineering

MEMS accelerometer, design and characterization

A Thesis

Submitted to the College of Engineering, University of Babylon in Partial Fulfillment of the Requirements for the Degree of Master in Engineering /Electrical Engineering /industrial Electronic

By

Idris Ahmed Muriei Salman

Supervised by

Asst. prof. Dr. Haider Al-Mumen

2022 A.D. **1443 A.H**

بسم الله الرحمن الرحيم

قُلْ هَلْ يَسْتَوِي الَّذِينَ يَعْلَمُونَ وَالَّذِينَ لَا يَعْلَمُونَ

إِنَّمَا يَتَذَكَّرُ أُولُوا الْأَلْبَابِ❋

صدق الله العلي العظيم

Supervisor Certification

We certify that this thesis titled (**MEMS accelerometer, design and characterization)** which is being submitted by **Idris Ahmed Muriei, w**as prepared under my supervision at the University of Babylon as a partial fulfillment of the requirement for the degree of Master of Science in Electrical Engineering.

Signature:

Name: **Asst. Prof. Dr. Haider Al-Mumen**

(Supervisor)

Data: / / 2022

In view of the available recommendation, I forward this thesis for debated by the examination committee.

Signature:

Name: **Asst. Prof. Dr. Shamam Fadhil Alwash**

(Head of Electrical Eng. Dept.)

Data: / / 2022

Examining Committee Certificate

We certify that we have read this thesis entitled **(MEMS accelerometer, design and characterization),** and as an examining committee examined the student **Idris Ahmed Muriei,** in its contents and that in our opinion it meets standard of a thesis for the degree of Master of Science in Electrical Engineering / Industrial Electronic.

Signature:
Name: **Prof. Dr. Qais K. Omran**
(Member)
Date: / / 2022

Signature:
Name: **Asst. Prof. Dr. Hameed R. Frhan**
(Member)
Date: / / 2022

Signature:
Name: **Asst. Prof. Dr. Haider Al-Mumen**
(Supervisor)
Date: / / 2022

Signature:
Name: **Prof. Dr. Hassan Jassim Motlak**
(Chairman)
Date: / / 2022

Signature:
Name: **Asst. Prof. Dr. Shamam Fadhil Alwash**
(Head of Electrical Eng. Dept.)
Date: / / 2022

Signature:
Name: **Prof. Dr. Hatem Hadi Obeid**
(Dean of College of Engineering)
Date: / / 2022

Dedication

I would like to dedicate my work to my father, may God have mercy on him, and my mother, may God take care of her, and all my family. I also dedicate this work to those who supported me throughout the study period without feeling bored or tired of my dear wife, may God protect her.

Acknowledgment

In the name of God, praise be to God, prayer and peace be upon the messenger of Allah.

All praises and thanks be to Allah for easting my task to accomplish this work despite all the hardships.

I would like to express my deepest sincere thanks to my supervisor, Asst. prof. Dr Haider Al-Mumen for their guidance, patience, advice, and constant support during my M.Sc. Research.

I would like to thank the staff of the Electrical Engineering Department at the University of Babylon, for providing the support needed to complete this thesis.

I would like to thank my best friend, M.Sc. Eng. Hamed Al-Ghanimi, for helping me with the preparatory year.

Also, I would like to warmly thank my wife and all family for their spiritual support in all aspects of my life.

Idris Ahmed

2022

Abstract

Enhanced 1-D, 2-D, and 3-D MEMS capacitive accelerometers were designed, simulated and characterized. COMSOL Multiphasics5.5 was used to simulate the device operation. The work demonstrated how to improve the capacitive sensitivity of the accelerometer by optimizing the dimension of the proof-mass and the sense fingers for the designed structure. However, we observed that improving the capacitive sensitivity in this way is limited by the linearity of the accelerometer.

The 1-D model has a length, width, and thickness of 1200 µm, 558 µm, and 30 µm respectively. The device has fast damping ratio of 0.265, an undamped natural frequency of 42578.4 rad/ sec, and a rise time of 0.05 ms. The device has an acceptable resonance frequency of 6500 Hz and bandwidth at -3dB of 1200 Hz. The device has a resolution of 0.05 g. The maximum measured acceleration before device collapse was 112 g. The output DC voltage sensitivity of 1-D accelerometers was measured to be 0.607 V/g.

The 2-D model has a length, width, and thickness of 1200, µm, 1000µm, and 30 µm respectively. The device has fast a damping ratio of 0.2251, an undamped natural frequency of 42980.32 rad/ sec, a rise time of 0.05 ms. The device has an acceptable resonance frequency of 6500 Hz and bandwidth at -3dB is1200Hz. The device has a resolution of 0.05 g for each axis and the maximum measured acceleration before device collapse was 96 g. The output DC voltage sensitivity of 2-D accelerometers was measured to be 1.45 V/g.

The 3-D model has a length, width, and thickness of 1200, µm, 1000 µm, and 30 µm respectively. The device has fast damping ratio of 0.2251, an undamped natural frequency of 42980.32 rad/ sec a rise time of 0.05 ms for x and y axes and a damping ratio of 0.2, an undamped natural frequency of 48073.4 rad/s, a rise time of 0.035 ms for z-axis. The device has an acceptable resonance frequency of 6500 Hz and bandwidth at -3dB is1200Hz for x and y axes, and resonance frequency 8000 Hz and bandwidth at -3dB is1000Hz for z-axis. The device has a resolution of 0.05 g for each axis and the maximum measured acceleration before device collapse was 96 g for x and y axes and while it was 165 g for z-axis. The output DC voltage sensitivity of 3-D

accelerometer was measured to be 1.45 V/g for x and y axes and 0.944 V/g for z-axis.

Table of Contents

CHAPTER ONE
INTRODUCTION

CHAPTER TWO
THEORY OF ACCELEROMETERS

CHAPTER THREE
DESIGN MODELS

CHAPTER FOUR
SIMULATION RESULTS

CHAPTER FIVE

CONCLUSION & FUTURE WORK

REFERENCES

List of Figures

List of Tables

List of Abbreviations

Abbreviation	Definition
AM	Amplitude modulation
CMOS	Complementary Metal Oxide Semiconductor
CVC	Capacitor to Voltage Converter
IMUs	Inertial Measurement Units
MEMS	Micro electromechanical Systems
QPD	Quadrant Photo Detector
SCS	Single Crystalline Silicon
SDI	Silicon Designs, Inc.
UTS	ultimate strength

List of Symbols

Symbol	Description
a	Acceleration
A	Overlap area
c	Damping coefficient
$\mathbf{C_0}$	The capacitance at a=0
C_{PE}	The piezoelectric transducer’s electrical capacitance
d_0	Capacitance gap at a=0
d_t	The distance between the tunneling tips at the point when the tunneling current appears
E	The young's modulus
$F_{applied}$	Applied force
$F_{damping}$	Damping force
F_{spring}	Spring force
g	ground acceleration
H1	Thickness of proof-mass
h_2	Beams thickness
I	Moment of inertia of the beam
I_S	The reverse bias saturation current
I_t	The tunnel sensor current
k	Spring constant

L	Beam length
$L_{effected}$	Effected beam Length
L1	Length of proof-mass
L_f	Finger length
L_R	The length of resistor at a=0
m	proof-mass
N	Number of finger
Q_{PE}	The piezoelectric transducer’s charge sensitivity
R	The resistor at a=0
S	The mechanical sensitivity
V	proof-mass volume
V_{in}	(peak voltage) of an alternating input voltage
V_O	Output DC voltage
V_{PE}	The piezoelectric transducer’s voltage sensitivity
V_S	The sense voltage (peak voltage)
V_T	The thermal voltage
W1	Width of proof-mass
W_2	Beam Width
$W_{\underline{n}}$	undamped resonance frequency
X	The displacement
ΔC	difference between tow sided capacitance
ΔL_R	The variation in length of resistor
ΔR	Variation resistor according to acceleration value

ν	Poisson ratio
ξ	Damping ratio
ρ	Material density
σ	Bending stress
Φ	The effective barrier height
V_t	The tunnel sensor voltage,
δ	deflection of the beam

1

Chapter One

INTRODUCTION

CHAPTER ONE

INTRODUCTION

1.1 Introduction

A micro-accelerometer is an electromechanical device which measures many modes of accelerations , Micro-accelerometers are used in several important applications like vibration, satellites, rockets[1-3], planes, trains[4], smart phone , laptop devices, and automatic braking systems [5-10], so it has become one of the most important to research for. A micro-accelerometers are most common currently used because they have the advantages of low-temperature dependence, low power consumption, high reliability, satisfactory accuracy[11], small dimensions, high sensitivity, high linearity, easy integration with electronics, low cost, and compatibility with Micro electromechanical Systems (MEMS) and Complementary Metal Oxide Semiconductor (CMOS) fabrication process [5, 12].

1.2 MEMS accelerometer overview

Micro-Electro-Mechanical Systems (MEMS) are small integrated devices which are usually fabricated on a silicon substrate and able to combine electrical and mechanical elements for sensing or actuating purposes. Examples of MEMS components include accelerometers, MEMS switches, microphones, and micro-resonators. Other new applications are rising as existing technologies are applied to miniaturize and integrate conventional devices [13-17]. .

With advances made in miniaturizing electronics, sizes of physical sensors have also reduced significantly, all thanks to MEMS. The MEMS comprises electronic and mechanical (moving) components, which perform different functions such as, transduction, actuation, signal processing. MEMS are fabricated using the same techniques used for CMOS electronic devices, such as etching, lithography patterning, material deposition [1]. Lithography is a technique used to make patterns of a required design for the sensor onto the semiconductor wafer, which then can be used as a reference to etch out some material or to deposit a patterned thin film. A combination of these steps is used to make a three-dimensional structure of the MEMS device. One of the best examples is the formation of free suspended beams used in a MEMS accelerometer, which is the focus of this thesis work. Most of the mechanical structures in MEMS are made out of semiconductor material such as, silicon, poly-silicon, silicon oxide. This because of the eas of fabrication due to the well-established fabrication technology for silicon. However, other materials may also be used depending on the application.

MEMS technology is used in the production of accelerometers, which sense forces along three axes of motions and output this data as an analog or digital signal.The most application of this technology has been in the automotive industry, where high _ gravity sensors are used for airbag deployment and low gravity sensors for active suspension and vehicle stabilization.

Accelerometers and gyroscopes measure angular velocities around the three axes of motion to obtain in situ data about the system. In theory, this concept can provide the users with accurate and intelligent compensation, for example, automated navigation and localization. MEMS accelerometers like other sensors suffer from various sources of error such us noise, nonlinearities , bias and sensitivity that lead to large errors in the data output . These errors are called random walk.

These MEMS sensor can be used in the robotic application as it can reduce the cost of the robot particularly if it used in the household task.In addition, with the increasing of the performance of the low-cost sensors, recent technology devices will begin to shift towards replacing the expensive sensors with lower-cost MEMS sensors that have the same performance.

1.3 Design Process of MEMS

The design and implementation of MEMS technology is very challenging task due to the many systems interaction and the multidisciplinary nature of the system. The design of complete system may require the cooperation of several people with different specialties such as electronics, physics, mechanics, etc. With the advent of well-established MEMS process technologies, researchers, about 15 years ago, were started to use several simulation design software's that enable top-down MEMS design, such as CoventorWare, MEMSPro, IntelliSuite, COMSOLMmultiphysics,.. etc, which made less time consuming for the design process.

1.4 Silicon Material in MEMS Technology

Silicon is an element with very special properties, for that it is used for electronic devices. Silicon's electrical properties can be modified through a process called doping [18] because it is wide study and documented properties, Silicon Designs, Inc. (SDI) has been the leader in capacitive MEMS accelerometer technology for over 25 years. Process technology combines integrated circuit and bulk silicon micro machined capacitive MEMS technology to produce a highly trusted, exceptionally rugged, capacitive acceleration sensor.

Single crystalline silicon (SCS) can be used as a pressure conductive layer or a drilling stop layer in wet drilling by doping with appropriate atoms. But it is especially used in displacement sensors as a structural material just like pressure sensors and accelerometers. According to a structural material, the most important mechanical factor is Young's modulus, which is a measure of a material's elasticity. SCS has mechanical anisotropy, which makes the crystallization direction of Young's modulus dependent.

1.5 Literature Review

- **Wong, W.C., I.A. Azid, and B.Y.J.S.v.-J.o.M.E, 2010 [19]** are derived and solve equations for the constant stiffness and effective mass of a folded and suspended beam in a small MEMS 1-D accelerometer. The stiffness constant is determined by Castigliano displacement theory. They found that the best way to find a constant for any shape of the beams is to use a superposition method that means calculating the effect of each beam separately and then summing their effects**.**

- **Benmessaoud, M. and M.M.J.M.t. Nasreddine, 2013 [20]** are explained the difference and relationship between the design improvement of the capacitive-folded comb 1-D accelerometer device and the sensitivity of the device like width of the beam, length of the beam, and proof-mass size. Based on their analysis, an improved design of the MEMS comb capacitance accelerometer was implemented.

- **Jun, J., et al., 2017 [21]** designed a 3-axis type acceleration system, which contain an interfacing circuit to the MEMS capacitance accelerometer. This interfacing circuit contains a capacitor to voltage converter (CVC) to achieve an output voltage, which is proportional to the acceleration.

- **Xu, W., et al 2017 [22]** fabricated a fully symmetric beam 1-D accelerometer which made of all-silicon sandwich structure. Its high consistency is ensured by the specially developed wet etching technology. Its all-silicon monolithic structure can avoid the shortcomings of thermal coefficient mismatch and bring a tight seal at the wafer scale. The fabricated prototype showed good stability and linearity at low bias, which experimentally demonstrates the effectiveness of their proposed design and fabrication techniques.

- **Mohammed, Z., I.A.M. Elfadel, and M.J.M. Rasras, 2018 [23]** designed an innovative single proof-mass for 3 axis acceleration measurement. They took advantages of its small size and low cost. Furthermore, they avoided the disadvantages such as undermining the comb fingers, and nonlinearity which leads to a lack of sensitivity and noise.

- **Alfaifi, A., et al., 2018 [17]** are proposed a three-dimensional accelerometer using CMOS-compatible MEMS technology. Capacitance gap was designed to be narrow to get a highly sensitive accelerometer to overcome the problem of off-vertical displacement. They figured out that the device symmetry was important approach to reduce the off-axis sensitivity.

- **Sarode, N., et al. 2018 [24]** are proposed 3-D comb capacitance accelerometer design enclosed a proof-mass suspension by four beams as spring structures. The spring structure is chosen to get the highest flexibility and obtain the proper displacement of the proof mass and sensing areas.

- **Ganji, B.A. and K.D.J.I.M. Hemmati, 2020 [25]** The number of differential capacitance used to measure acceleration on the z-axis is two, while the number of differential capacitance used to measure acceleration on the x-axis and y-axis are four groups. The reason for using different capacitive combinations is that the device, in addition to measuring the acceleration in each axis direction, can separately and accurately assume the amount of acceleration for each axis.
- **Wang, Y., X. Zhao, and D.J.S. Wen, 2020 [26]** In this study, a three-axis dual-beam accelerometer was designed and fabricated using MEMS technology and the effects of average two-beam structure sizes on the sensitivity of the proposed accelerometer provide potential. To further improve the performance of the 3-axis accelerometers..

1.6 Aims of the thesis

The thesis aim is to design and characterization three-models of capacitive accelerometers. The first model is a one-dimensional capacitive accelerometer; the second model is a two-dimensional capacitive accelerometer; while the third model is a three-dimensional capacitive accelerometer. Models are characterized through the following points

1- Acceleration vs. displacement

2- Acceleration vs. difference of capacitance

3- Maximum Stress

4-Time response of the models

5- Frequency responses of 1-D model

6-The sense voltage vs. acceleration of the models

7- Maximum acceleration before models collapse

8- Minimum resolution

9- Output dc voltages vs. acceleration of the models

1.7 Thesis outline:

Chapter 1: This chapter provides an introduction of the thesis

Chapter 2: This chapter explains the requirements and theories of Accelerometer.

Chapter 3: This chapter explains the designing accelerometers for three models.

Chapter 4: This chapter provides the simulation and results for three designed models using COMSOLmultiphisices software**.**

Chapter 5: This chapter contains conclusions and future works of this thesis.

2

Chapter Two

THEORY OF ACCELEROMETER

CHAPTER TWO

THEORY OF ACCELEROMETERS

2.1 Introduction

An accelerometer is a device that can measure the physical acceleration to which an object is subjected due to inertial forces or mechanical excitation.

In this chapter, we will discuss the most common types of accelerometers, depending on their principle of operation. Having presented the advantages and disadvantages of each type, we will choose the one that will be the subject of this letter. Then present the theory of the chosen type with analysis.

.

2.2 Types of Accelerometer

There are several types of accelerometers that are classified according to their principle of operation [23]:

1- Piezoresistive accelerometer.
2- Piezoelectric accelerometer.
3- Tunneling accelerometer.
4- Optical accelerometer.
5- Capacitive accelerometer.

2.2.1 Piezoresistive accelerometer

The principle of operation is a resistant materials varying according to the pressure with a resistor. The pressure applied on the resistant materials is proportional with acceleration. The Illustration of piezoresistive accelerometer is shown in figure 2.1 [27, 28].

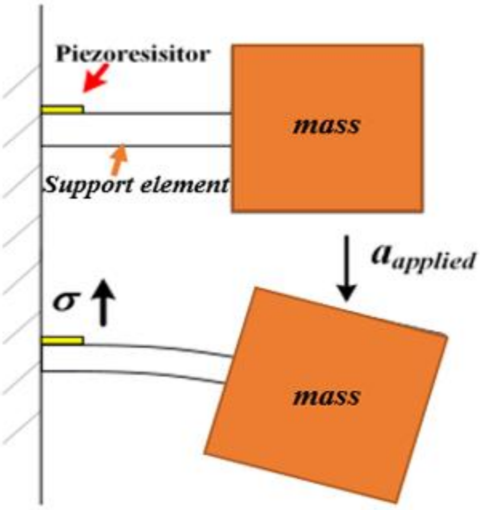

Figure 2.1 The Illustration of piezoresistive accelerometer [27]

$$[\Delta R/R] = (1 + 2\,\nu)\,(\Delta L/L) + \Delta\,\rho/\rho \qquad (2.1)$$

Where,

ΔR: variation resistor according to acceleration value,

R is the resistor at a=0,

ΔL is the variation in length of resistor,

ν: is Poisson ratio,

L is the length of resistor at a=0

Δρ is the resistivity variation and ρ is the resistivity of resistor.

2.2.2 Piezoelectric accelerometer

The principle operation of piezoelectric accelerometer is when applying acceleration on the device; the proof-mass will be moved with a certain displacement causes a stress occurs in the beam. The beam is made from piezoelectric material as shown in figure 2.2. The stress causes a difference potential occurs between electrodes on each sides of the beam as equation 1.2 [29, 30].

$$V_{PE} = \frac{Q_{PE}}{C_{PE}} \qquad (2.2)$$

Where V_{PE} is the PE transducer's voltage sensitivity (mv/g),

C_{PE} is the PE transducer's electrical capacitance,

Q_{PE} is the PE transducer's charge sensitivity.

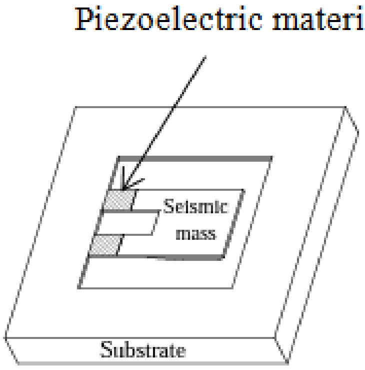

Figure 2.3 The Illustration of piezoelectric accelerometer [29]

2.2.3 Tunneling accelerometer

The principle operation of the tunneling accelerometer is when applying acceleration on the device, the proof-mass will be move with a certain displacement, causing the tunneling current to change suddenly. The Tunneling accelerometer contains proof-mass, beams, and electrodes placed on the anchor plan as shown in figure 2.3. The tunneling current accelerometer is proportional exponentially on the distance d and is defined by[31, 32]:

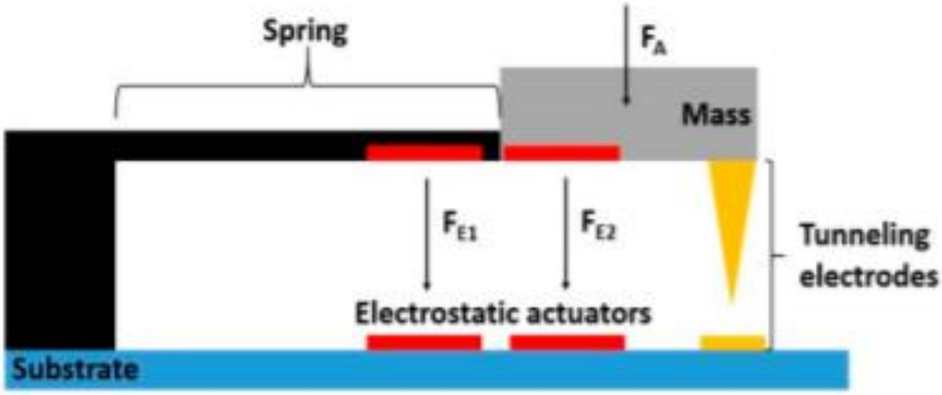

Figure 2.3 The Illustration of tunneling accelerometer [31]

$$I = V\,(-\propto\sqrt{\Phi}d) \qquad (2.3)$$

Where,

V the tunnel sensor voltage,

$\propto = 1.024\ eV^{-0.5}\text{Å}^{-1}$,

Φ is the effective barrier height

d: is the distance between the tunneling tips at the point when the tunneling current appears

2.2.4 Optical accelerometer

The principle operation of the optical accelerometer is that when applying acceleration on the device, the proof-mass will be move with a certain displacement up and down, causing shift the projected light spot. The optical accelerometer contains proof-mass, beams, light spot, mirrors, and four-quadrant photo detector QPD [33, 34] as shown in figure 2.4**.**

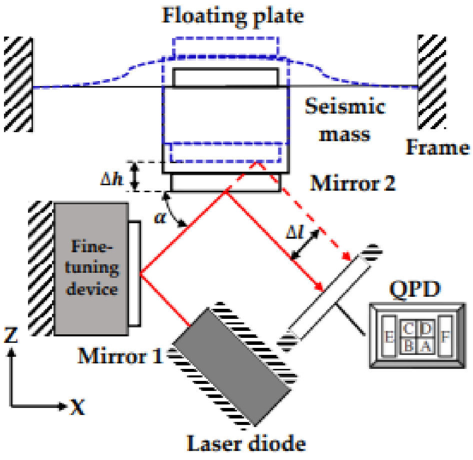

Figure 2.4 The Illustration of an optical accelerometer [33]

2.2.5 Capacitive accelerometer

Mechanical movement causes changes in distance between electrodes causes changes induces capacitance that can be measured by capacitance to voltage converter.

Capacitive accelerometer consists of four parts spring, proof mass, sense electrodes, and anchor as shown in figure 2.5. When an acceleration is applied the proof-mass is move with a certain displacement, this displacement causes varying in capacitance this varying depend on acceleration, by using capacitive to voltage convertor we can find the amount of acceleration[35, 36] .

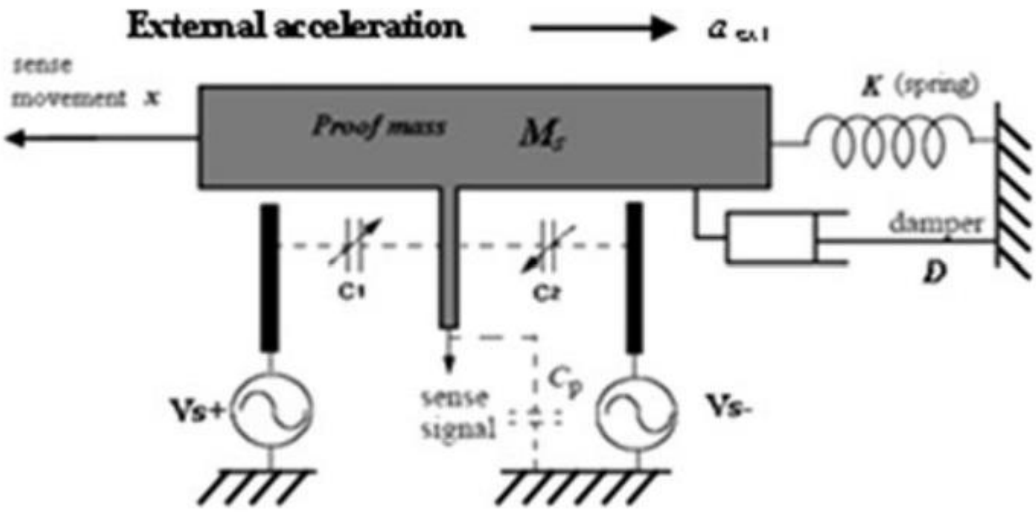

Figure 2.5 Schematic of the capacitive accelerometer [35]

2.3 Comparison of the different types of accelerometers

Table 2.1 Comparison of the many types of accelerometers in terms of advantages and disadvantages.

Accelerometer type	advantages	disadvantages
Piezoresistive accelerometer	-Simple design, -Simple Fabrication, -Simple readout circuit	-Low sensitivity -Large temperature sensitivity -Large and bulky designs
Piezoelectric accelerometer.	-Self-powered -Digital output -Simple interference circuit	-Bad DC response -large size
Tunneling accelerometer.	-High sensitivity -low foot print	-large noise level -Highly expensive fabrication
Optical accelerometer.	-Highly sensitive -very high noise immunity EMI	-Difficult integrate with electronic readout
Capacitive accelerometer.	-Good DC performance -High sensitivity -low temperature sensitivity -low noise-low drift	-Susceptible electromagnetic interference

2.4 Theory of capacitive accelerometer

Mechanical movement causes changes in distance between electrodes. This change in distance causes changes induces capacitance that can be measured by capacitance to voltage converter (CVC)[8, 37].

Capacitive accelerometer consists of four parts spring, proof mass, sense electrodes, and anchor as shown in figure 2.6. When the structure is moved the proof mass is move with displacement. This displacement causes varying in capacitance. By using capacitive to voltage convertor we can find the amount of acceleration[38].

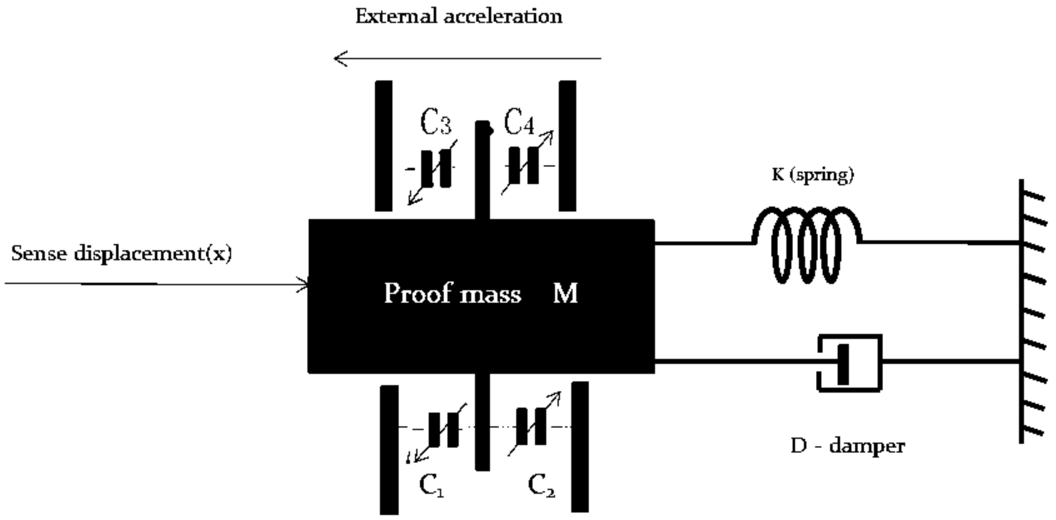

Figure 2.6 Illustration of a capacitive accelerometer

When an acceleration equal to zero (a=0), the proof-mass is resting in the middle with its fingers of the left and right fixed fingers. This cause C_1, C_2, C_3 and C_4 are equal. When acceleration not equal to zero along horizontal direction the proof-mass (m) experiences an inertial force = - m x a. Therefore, the spring deflects and the proof-mass with its fingers move with a certain displacement along inertial force direction.

These causes change gaps of the left and right capacitances; causes the capacitances C_1, C_2, C_3, and C_4 to be varied**.**

Mechanical movement causes changes in distance between electrodes. This change in distance causes changes induces capacitance that can be measured by capacitance to voltage converter (CVC)[8, 37].

2.5 Mechanical analysis

The basic Concepts of accelerometers are based on second law of Newton's of motion [39].

$$F_{applied} - F_{damping} - F_{spring} = m \frac{d^2x}{dt^2} \qquad (2.4)$$

Where,

m is the mass of the proof mass

Thus,

$$m\frac{d^2x}{dt^2} + c\frac{dx}{dt} + kx = m\,a\,(t)$$

Where,

c = damping coefficient

k = spring constant

by Taking Laplace transform:

$$[ms^2 + cs + k]\,x(s) = ma(s)$$

$$[s^2 + \frac{c}{m}\,s + \frac{k}{m}]\,x(s) = a(s)$$

Therefore, the T.F. is:

$$\frac{x(s)}{a(s)} = \frac{1}{s^2 + \frac{c}{m}s + \frac{k}{m}} \qquad (2.5)$$

Where,

$s^2 + \frac{c}{m}s + \frac{k}{m} = 0$ is called characteristic equation

By comparing the characteristic equation with general form,

$$s^2 + 2\xi w_n s + w_n^2 = 0$$

Then,

$$w_n^2 = \frac{k}{m}$$

$$w_n = \sqrt{\frac{k}{m}} \qquad (2.6)$$

Where, w_n is undamped frequency.

$$2\xi w_n = \frac{c}{m}$$

Thus,

$$\xi = c/2\sqrt{km} \qquad (2.7)$$

Where, ξ is damping ratio

The mechanical sensitivity S of the accelerometer is defined by[40]:

$$S = x/g \qquad (2.8)$$

Where, X is the displacement and g is the gravity.

2.6 MEMS capacitive analysis

MEMS capacitor is a parallel plate separated by a distance d with overlapping area A have a Capacitance equal to[36, 41-44]:

$$C = \frac{\in_0 . \in_r . A}{\mathrm{d}} \tag{2.9}$$

Where,

$\in_0 = 8.85 \times 10^{-12}$ F/m is the free space Permittivity ,

$\in_r$ is the dielectric medium relative permittivity ($\in_r = 1$ for air)

At a=0 , $C1 = C_2 = C_3 = C_4 = C_0$

$$\mathrm{C}_0 = \frac{\in_0 . \in_r . A}{d} \tag{2.10}$$

$$\mathrm{C}_0 = \frac{\mathrm{N}_f \in_0 . \in_r . A}{d} \tag{2.11}$$

For N_f , no. of pair finger

At a≠0 on x-axis then the proof mass with proof-mass fingers move with certain displacement x the capacitance are change as[25]

$$\mathrm{c}_1 = \mathrm{c}_3 = \frac{\mathrm{N}_f \in_0 . \in_r . A}{d+x} \tag{2.12}$$

$$\mathrm{c}_2 = \mathrm{c}_4 = \frac{\mathrm{N}_f \in_0 . \in_r . A}{d-x} \tag{2.13}$$

Deference Capacitive sensitivity

$\Delta C = C_2 - C_1$

$$\Delta c = \mathrm{c}_2 - \mathrm{c}_1 = \frac{\mathrm{N}_f \in_0 . \in_r A}{d-X} - \frac{\mathrm{N}_f \in_0 . \in_r A}{d+X}$$

$$\Delta c = \frac{\mathrm{N}_f \in_0 . \in_r . A}{d} \left(\frac{1}{1-X/d} - \frac{1}{1+X/d}\right)$$

$$\Delta \mathrm{c} = \mathrm{c}_0 \left(\frac{1}{1-X/d} - \frac{1}{1+X/d}\right) \tag{2.14}$$

$$\text{Capacitive sensitivity} = \Delta C / \mathrm{g} \tag{2.15}$$

3

Chapter Three

DESIGN MODELS

CHAPTER THREE

DESIGN MODELS

3.1 Introduction

The three models of accelerometers were built by the required calculations. The dimensions of the designed accelerometers parts were chosen based on these calculations, as well as through the trial and error technique.

Various aspects are taken into consideration before finalizing the

Configurations of the accelerometers. Special attention is paid to the available fabrication processes, signal conditioning electronic circuits, material selection.

The proof-mass sizes and spring stiffness are selected in such a way that there shall be a capacitance change for 0.05 g (minimum resolution). This limitation comes from the capacitance signal that can be handled comfortably by the electronics scheme.

For calculating the proof-mass to electrode gap and damping aspects, the micro structure is considered as working under ambient pressure conditions. This is due to fabrication facility limitation in chip level sealing under vacuum.

3.2 Structure design 1-D capacitive accelerometer

Figure 3.1 and figure 3.2 shows a one-dimension model of the prototyped differential accelerometer designed using MEMS technology, the sensor has overall dimensions of approximately 620μm × 530μm with a structural thickness of 30 μ m.

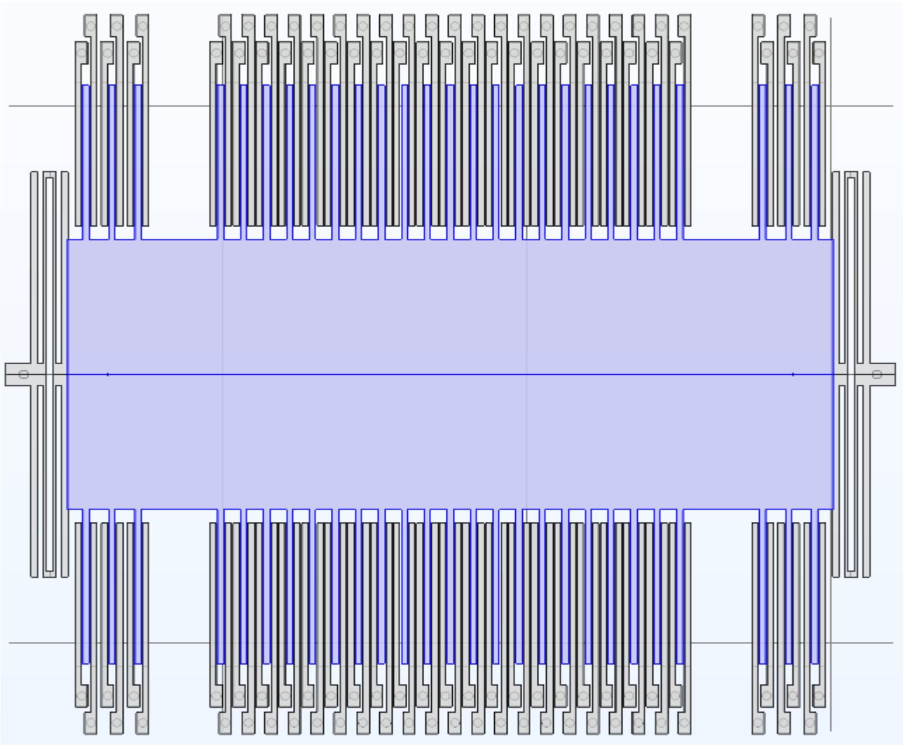

Figure 3.1 The middle layer of structural model of the differential accelerometer

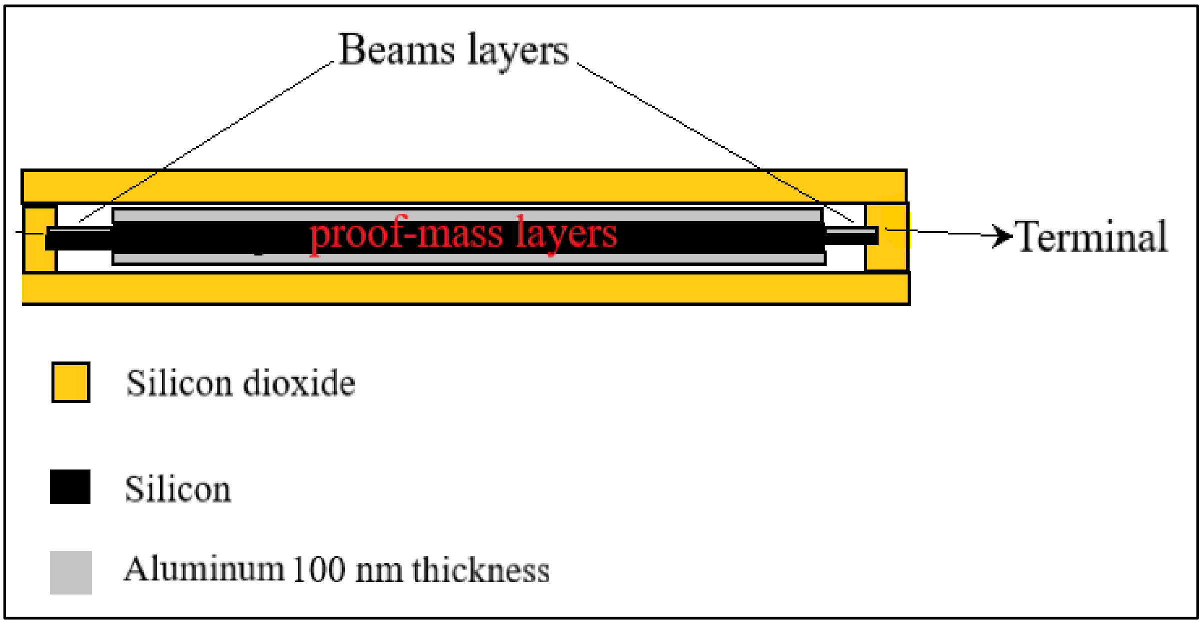

Figure 3.2 Layers of structural model of the 1-D accelerometer

The geometrical and physical parameters of One-dimensional capacitive accelerometer are shown in table 3.1.

Table 3.1 Geometrical and physical parameters of 1-D model.

Parameters	**Designed value**
Device length	620 µm
Device width	530 µm
Device thickness	30 µm
Mass width W_1	200 µm
Mass length L_1	500 µm
Mass thickness H_1	6 µm
Beam half-length L_X	150 µm
Beams width W_2	2 µm
Beams thickness h_2	2 µm
Capacitance gap d_0	1 µm
Right finger length	120 µm
Left finger length	140 µm
Finger width	4 µm
Finger thickness h_f	6 µm
Finger overlap length	100 µm
Number of sensing fingers	40 pairs
Young’s Modulus E	160 GPa
The density of poly-Si	2320 kg/m^3

The model has three layers the top layer is made of silicon dioxide with a thickness of 14 μ m. The middle layer, wich have the proof-mass , beams, and electrodes are made of silicon matrial coated by alminum material with overal thickness equal to 6 μ m, and the bottom layer is made of silicon dioxide with thickness of 10 μ m.

The air-gap between the moving sensor fingers and the fixed sensor fingers is one micrometer.

The capacitances air-gap between the moveable fingers and fixed fingers and damping aspects were calculated under ambient conditions. Terminal is the output sense voltage sensing acceleration.

3.3 Material selection

Single-crystalline silicon (100) is chosen for the beams and proof-mass because its properties are as light as aluminum and have the same young's modulus as steel. Furthermore, The coefficient of thermal expansion is much lower than that of thermal expansion, which makes it dimensionally stable even at high temperatures.

The proof mass should be coated with aluminum material to take advantage of its conductive property. The upper and lower part of the anchor plan for the sensor fingers, and the beams are made from silicon dioxide in order to take its advantage of the insulating property and to avoid static electricity. As for the sensor fingers, they are made of aluminum.

3.4 Analytical design of 1-D accelerometer

3.4.1 Mass of the proof-mass (m)

The dimensions of the proof mass were selected to be compatible with the dimensions of the beams to obtain the required accuracy, sensitivity, frequency, and bandwidth of the sensor. The designed dimension of this work is shown in table 3.2.

Table 3.2 The designed proof-mass dimension of 1-D model

Parameter	Designed
Length of proof-mass L_1	500 µm
Width of proof-mass W_1	200 µm
Thickness of proof-mass H_1	6 µm
Number of finger N	40+12
Finger length L_f	114 µm

Thus,

$$V = L_1 x W_1 \text{ x } H_1 + N\,(L_f \text{ x } W_f \text{ x } h_f) \qquad (3.1)$$

$$V=500\times10^{-6}\times200\times10^{-6}\times6\times10^{-6}+40(114\times10^{-6}\times4\times10^{-6}\times6\times10^{-6})$$

$$V=709.44\times10^{-18}\mathrm{m}^3$$

$$\text{Mass of proof-mass (m)} = \rho.\,V \qquad (3.2)$$

$$=2320\times709.44\times10^{-18}=1.6459\times10^{-9}\text{ kg}$$

3.4.2 The initial force on the proof-mass of 1-D model

The Initial force that acts on the proof mass F, at applies acceleration 1 g is:

$$F = -\,m.a \qquad (3.3)$$

Where,

a is the acceleration,

m is the mass of the proof-mass.

Then,

$F = 1.6459 \times 10^{-9}$ kg $\times 1 \times 9.8 = 1.61298 \times 10^{-8}$N

This force is applied on four beams, therefore, the force applied on a single beam is:

$F_{beam} = F/4 = 0.4 \times 10^{-8}$ N

3.4.3 Beams deflection

The first end of the folded beam is attached to the proof-mass. While, the second end is connected to the anchor plan. To calculate the parameters of the system, the four folded beam was considered as a spring, as shown in figure 3.3. When applied acceleration, initial force c moves the proof mass and then a deflection on the beams. This deflection is depending on the spring constant, k.

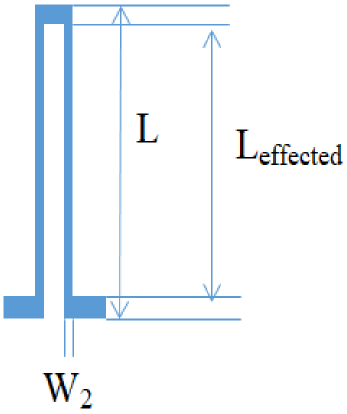

Figure 3.3 The structure of the folded beam

The deflection of the beam can be calculated as follows:

$L_{effected} = 158 - (4+4) = 150$ µm

$$\delta = \frac{F_{beam} \times L^{3}_{\text{effected}}}{12EI} \qquad (3.4)$$

Where,

E is the young's modulus for silicon E=1.6 × 10^{11} N/m^2,

I is the moment of inertia of the beam.

$$I = \frac{h_2 \times W_2^3}{12} = 1.33333 \times 10^{-24}\ m^4$$

The displacement x = δ =0.0054 µm

From equation 2.8, the displacement sensitivity (S) of the accelerometer is:

$$S = \frac{x}{g}$$

S= 0.0054 µm/g

For maximum deflection, a=60 g, the Maximum displacement is 0.0053µm/g x 60g and the maximum displacement = 0.324 µm

3.4.4 Bending stress of the beam

To calculating the bending stress (σ) under simple bending on a beam, the following derivation was used:

$$\sigma = \frac{M}{I} \times y \qquad (3.5)$$

Where,

M is the moment acting on the beam,

y is the deflection distance.

At 60 g acceleration on x-axis:

M = F_{beam} * L x 60

$M = 0.4 \times 10^{-8} \times 150 \times 10^{-6} \times 60$

$M = 0.36 \times 10^{-10}$ Nm

To find the maximum bending stress, which is at maximum displacement, y=0.324 µm, Thus:

$$\sigma = \frac{0.36 \times 10^{-10}}{1.3333 \times 10^{-24}} \times 0.324 \times 10^{-6}$$

$$\sigma = 8.75\ MPa$$

At acceleration of 60 g

3.4.5 Safety Factor

Safety Factor = ultimate strength / maximum stress (3.6)

From calculation the maximum stress when acceleration maximum at 60 g, and ultimate strength for silicon = 7000MPa

Thus

Safety Factor = ultimate strength / maximum stress (σ)

Safety Factor = 7000/8.75

= 800

3.4.6 Natural frequency

From equation 2.6

$$w_n = \sqrt{\frac{k}{m}}$$

$$f_n = \frac{1}{2\Pi}\sqrt{\frac{k}{m}}$$

$$K = \frac{F}{\delta} \qquad (3.7)$$

$$\mathrm{k} = \frac{F}{\delta} = \frac{1.61298\times 10^{-8}}{0.0054\mu\mathrm{m}} = \text{ 2.987 N/m}$$

Thus

$$\mathrm{f_n} = \frac{1}{2\Pi}\sqrt{\frac{2.987}{1.6459\times 10^{-9}}} \quad = 6.78 \text{ kHz}$$

3.4.7 Capacitance Sensitivity

Accelerometer Sensitivity for capacitive accelerometer is obtained from difference between tow sided capacitance. The air gap between movable finger and fixed finger is 1 µm. The capacitance for tow sided are equal and ∆C= 0. When applied 1 g acceleration The air gap was varied causes the capacitance in one side is increase and capacitance in other side is decrease.

From equation 2.11 for x-axis and y-axis

$$\mathrm{C_0} = \frac{\mathrm{N}_f \epsilon_0 . \epsilon_r . A}{d}$$

$A=L_f \times h_f=105 \times 10^{-6} \times 6\times 10^{-6}$

$A=630 * 10^{-12}\ m^2$

$$\mathrm{C_0} = \frac{40\times 8.85\times\ 10^{-12}\times 1\times 630\times 10^{-12}}{1\mathrm{x}10^{-6}} = \quad 223.02 \text{ f F}$$

From equation 2.14

$$\Delta\mathrm{c} = \mathrm{c_0}\left(\frac{1}{1-\frac{X}{d}} - \frac{1}{1+\frac{X}{d}}\right)$$

X is the displacement = δ at 1g= 0.0054 μm

$$\Delta c = 223.02\ (\frac{1}{1-0.0054} - \frac{1}{1+0.0054})$$

Δc =2.4087 f F

Capacitance sensitivity= $\Delta c/g$

Capacitance sensitivity =2.4087 f F/g

3.5 Structure design of 2-D capacitive accelerometer

Figure 3.4 shows a 2-dimension model of the prototyped differential accelerometer. It was designed using MEMS technology. The sensordimension is 1.2 mm × 1 mm with thickness of 30µm.

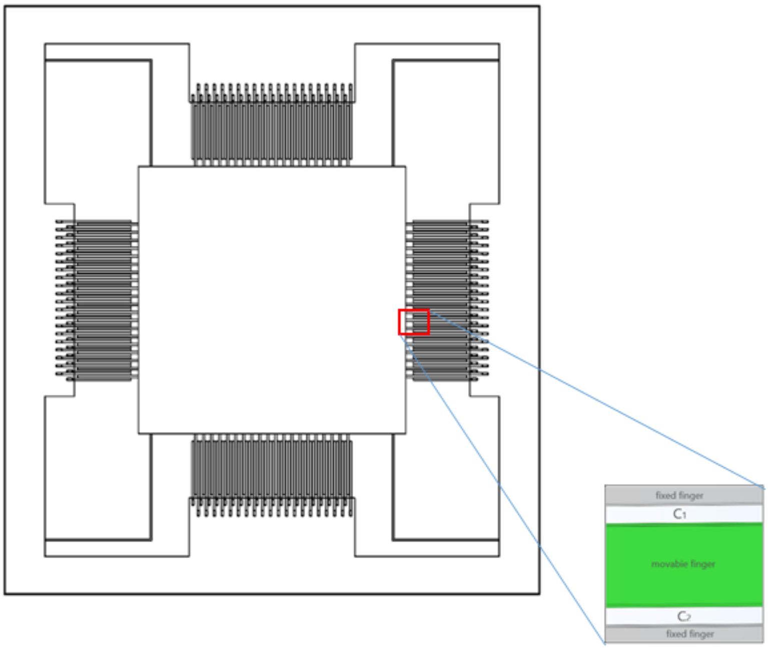

Figure 3.4 Structural model of the differential 2-D accelerometer

The model has three layers the top layer is from silicon dioxide with thickness of 10 µ m and the middle layer it wich have proof-mass , beams, and electrodes from silicon matrial coated by alminum material with overal thickness of 10 µ m , and the bottom layer is from silicon dioxide with thickness of 10 µ m. The layers are shown in figure 3.5.

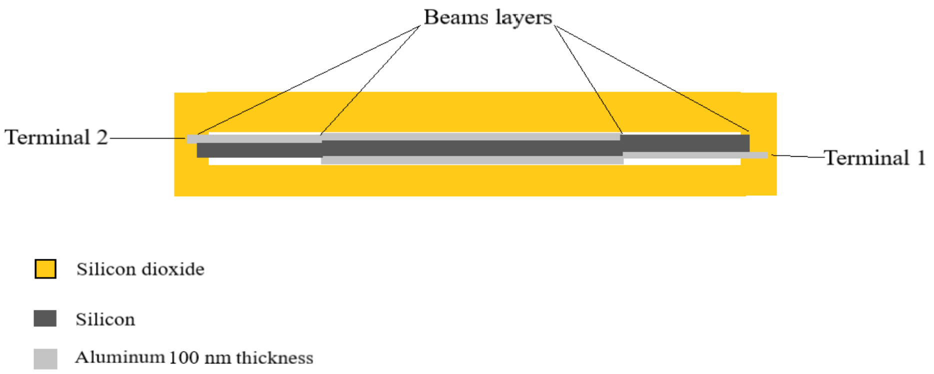

Figure 3.5 Layers of structural model of the 2-D accelerometer

Four operating electrodes are located on the proof-mass four sides. The number of fingers is compatible with the size of the proof-mass. The proof mass should be coated with aluminum material .To take advantage of the conductive property. But it is coated in a special way .Where all the fingers of the x-axis sensing which installed on the proof-mass are connected to each other as well as the y-axis. The proof mass connection of 2-Daccelerometer are shown in figure 3.6.

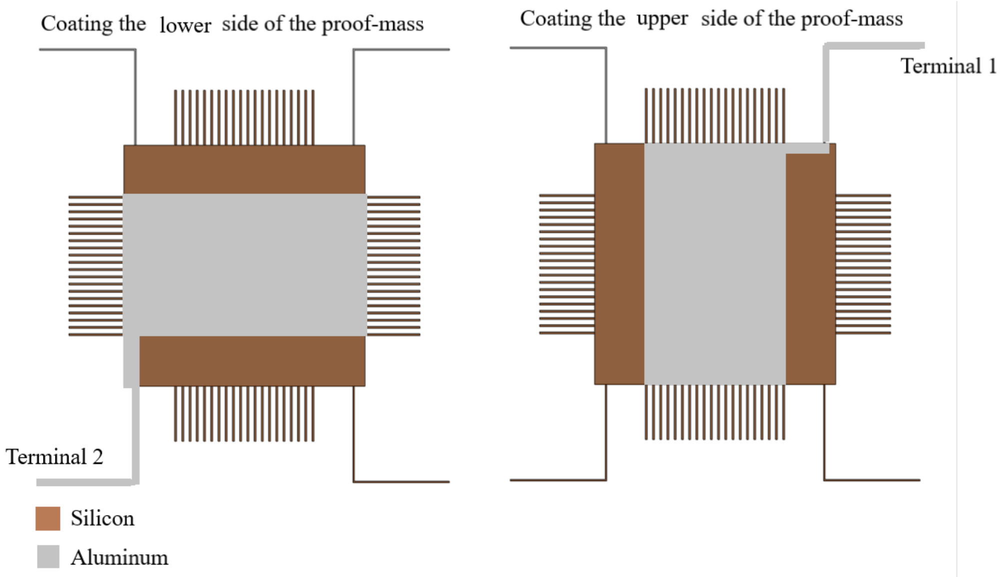

Figure 3.6 Proof mass connection of 2-D accelerometer

Thickness of aluminum is 100 nm. Terminal 1 is the output sense voltage sensing acceleration on x-axis. While terminal 2 is the output sense voltage sensing acceleration on y-axis. The geometrical and physical parameters of the 2-D model are shown in table 3.3.

Table 3.3 Geometrical and physical parameters of the 2-D model.

Parameters	**Design**
Device length	1100 µm
Device width	1000 µm
Device thickness	30 µm
Mass width W_1	500 µm
Mass length L_1	500 µm
Mass thickness H_1	10 µm
Beam length L_X	200 µm
Beam length L_Y	200 µm
Beams width W_2	3 µm
Beams thickness h_2	8 µm
Capacitance gap d_0	1 µm
Right finger length	120 µm
Left finger length	140 µm
Finger width	4 µm
Finger thickness h_f	10 µm
Finger overlap length	100 µm
Number of fingers	80 pair
Young’s Modulus E	160GPa
The density of poly-Si	2320 kg/m^3

3.6 Analytical design

3.6.1 Mass of proof-mass (m)

The dimensions of the proof mass were selected with the dimensions of the beams to obtain the required accuracy, sensitivity, frequency and bandwidth of the sensor for two dimensions(x, and y) axes. The designed dimension of this work is shown in table 3.4.

Table 3.4 the designed dimension of this work

Parameter	Designed
Length of proof-mass L_1	500 µm
Width 0f proof-mass W_1	500 µm
Thickness proof-mass H_1	10 µm
Number of finger N	80
Finger length L_f	114 µm

From equation (3.1)

$$V= L_1 \text{ x } W_1 \text{ x } H_1 + N\,(L_f \text{ x } W_f \text{ x } h_f)$$

$$V=500 \text{ x } 10^{-6} \text{ x } 500 \text{ x } 10^{-6} \text{ x } 10 \text{ x } 10^{-6} + 80(114 \text{ x } 4 \text{ x } 10)$$

$$V=2.8648 \text{ x } 10^{-12} m^3$$

From equation (3.2)

Mass of proof-mass (m) = ρ. V

$$=2320\ kg/m^3 \text{ x } 2.8648 \text{ x } 10^{-12}\ m^3 = 6.646 \text{ x } 10^{-9} kg$$

3.6.2 The initial force on the proof-mass of 2-D model

The initial force act on the proof-mass F, at apply acceleration 1 g is:

$$\mathrm{F} = -\mathrm{m.a}$$

$$\mathrm{F} = 6.646 \times 10^{-9}\mathrm{kg} \times 1 \times 9.8$$

$$= 6.5134 \times 10^{-8}\mathrm{N}$$

This force divided on four beams then the force per beam

$\mathrm{F}_{\mathrm{beam}} = \mathrm{F}/4 = 1.6283 \times 10^{-8}$ N

3.6.3 The beams deflection

The beam attached with proof mass and another side fixed with anchor plan. When applied acceleration on x-axis or y-axis, the initial force was moved the proof mass, causes deflection the beams. This deflection depends on spring coefficient k. Because of equal length of beams $L_x=L_y$, then equal coefficient $k_x=k_y$ and equal deflection $\delta_x=\delta_y$.

$$\delta x = \delta y = \frac{\mathrm{F}_{beam} \times L_x^3}{12EI} \qquad (3.9)$$

$$\mathrm{I} = \frac{\mathrm{h}_2 \times W_2^3}{12} = 18 \times 10^{-24}\ \mathrm{m}^4$$

$\delta x = \delta y =$ 0.0053μm

From equation 2.8 the mechanical sensitivity S of the accelerometer is

$$\mathrm{S} = \frac{\mathrm{X}}{\mathrm{g}}$$

$$\mathrm{S}_y = \mathrm{S}_x = \frac{\mathrm{X}}{\mathrm{g}} = 0.0053\mu\mathrm{m/g}$$

For maximum deflection g =60 on x-axis or y-axis then

Maximum g δx =0.0053μm/g × 60 g

Maximum δx =0.318 μm = Maximum δy

3.6.4 Bending stress of the beam

To calculating the bending stress under simple bending in a beam is given using equation (3.5):

$$\sigma = \frac{M}{I} \times y$$

$$\sigma_x = \frac{M}{I_x} \mathrm{X}\, y$$

$M = F_{beam} \times Lx \times 60$

$M = 1.6283 \times 10^{-8} \times 200 \times 10^{-6} \times 60$

$M = 1.954 \times 10^{-10}$ Nm

For maximum bending stress y = maximum displacement

Thus

$$\sigma_x = \frac{1.954 \times 10^{-10}}{18 \times 10^{-24}} \times 1 \times 10^{-6} = 10.867 \text{ MPa}$$

3.6.5 Safety Factor

From equation (3.6)

Safety Factor =ultimate strength / maximum stress

From calculation the maximum stress when acceleration maximum on z-axis at 60 g and ultimate strength for silicon = 7000MPa

Thus

Safety Factor = 7000/10.86 = 644.152

3.6.6 Natural frequency

From equation 2.6

$$w_n = \sqrt{\frac{k}{m}}$$

$$f_n = \frac{1}{2\Pi}\sqrt{\frac{k}{m}}$$

$$K = \frac{F}{\delta}$$

From calculation $\delta_x = \delta_y$ then $k_x = k_y$ and same natural frequency.

$$k_x = \frac{F}{\delta_x} = \frac{6.5134\times10^{-8}}{0.0053\mu m} = 12.2894 \text{ N/m}$$

Thus

$$f_n = \frac{1}{2\Pi}\sqrt{\frac{12.2894}{6.646\ \mu g}} = 6.844 \text{ kHz}$$

3.6.7 Accelerometer capacitance Sensitivity

From equation 2.11 for x-axis and y-axis

$$C_0 = \frac{N_f \epsilon_0 . \epsilon_r . A}{d}$$

$A = L_f \times h_f = 100 \times 10^{-6} \times 10\times10^{-6}$

$A = 1000 * 10^{-12}\ m^2$

$$C_0 = \frac{40\times8.85\times10^{-12}\times1\times1000\times10^{-12}}{1\times10^{-6}} = 354 \text{ f F}$$

From equation 2.14

$$\Delta c = c_0\left(\frac{1}{1-\frac{X}{d}} - \frac{1}{1+\frac{X}{d}}\right)$$

X is the displacement $= \delta x$ at 1g= 0.0053µm

Thus

$$\Delta c = 354\,\mathrm{f\,F}\left(\frac{1}{1-0.0053} - \frac{1}{1+0.0053}\right)$$

$\Delta c = 3.8$ f F

Capacitance sensitivity= $\Delta c/g$

Capacitance sensitivity for x-axis and y-axis=3.8 f F/g

3.7 Three-dimensional capacitive accelerometer

Figure 3.7 shows a three dimension model of the prototyped differential accelerometer designed using MEMS technology, the sensor has overall dimensions of approximately 1.1 mm × 1mm with a structural thickness of approximately 30 µ m.

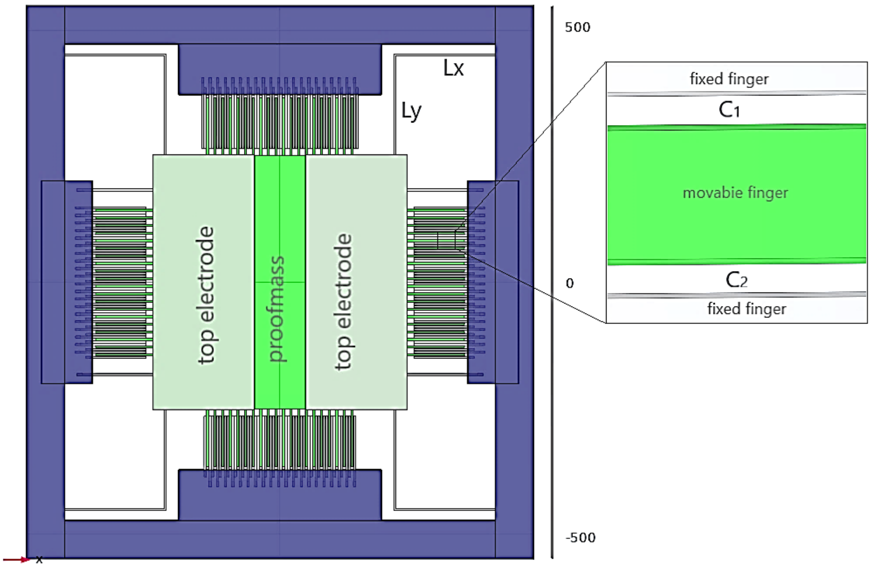

Figure 3.7 Structural of the 3-D differential accelerometer

The model has three layers the top layer is from silicon dioxide with thickness of 10 μ m and the middle layer it wich have proof-mass , beams, and electrodes from silicon matrial coated by alminum material with overal thickness of 10 μ m , and the bottom layer is from silicon dioxide with thickness of 10 μ m. The layers are shown in figure 3.8.

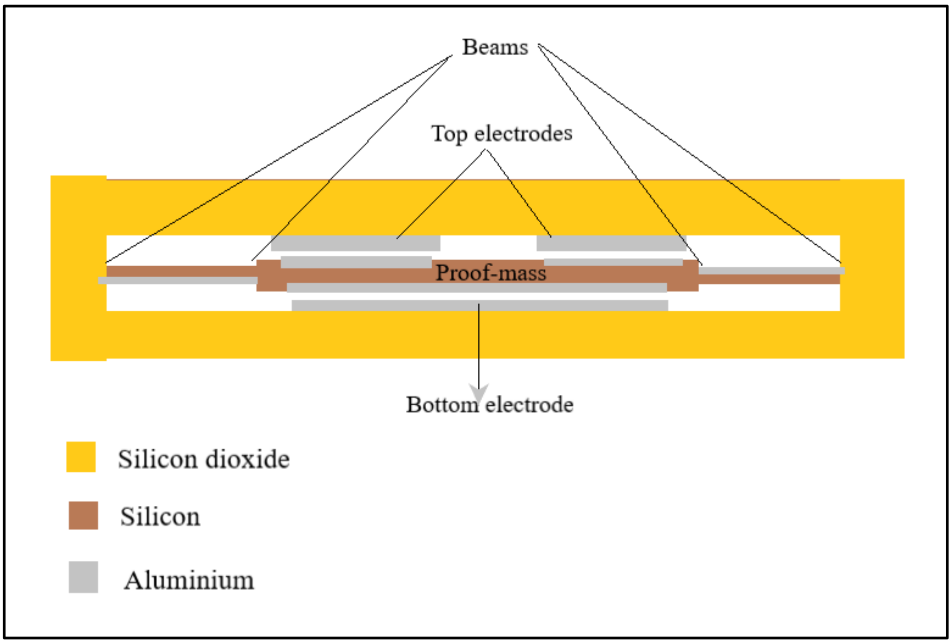

Figure 3.8 Layers of structural model of the 3-D accelerometer

Six operating electrodes are located on the four sides of the proof mass, and up and down of the proof mass. The number of fingers is compatible with by the size of the proof mass. The proof mass should be coated with aluminum material .To take advantage of the conductive property. But it is coated in a special way .Where all the fingers of the x-axis sensing which installed on the proof-mass are connected to each other as well as the y and z axes. The proof mass connection of 3-D accelerometer is shown in figure 3.9.

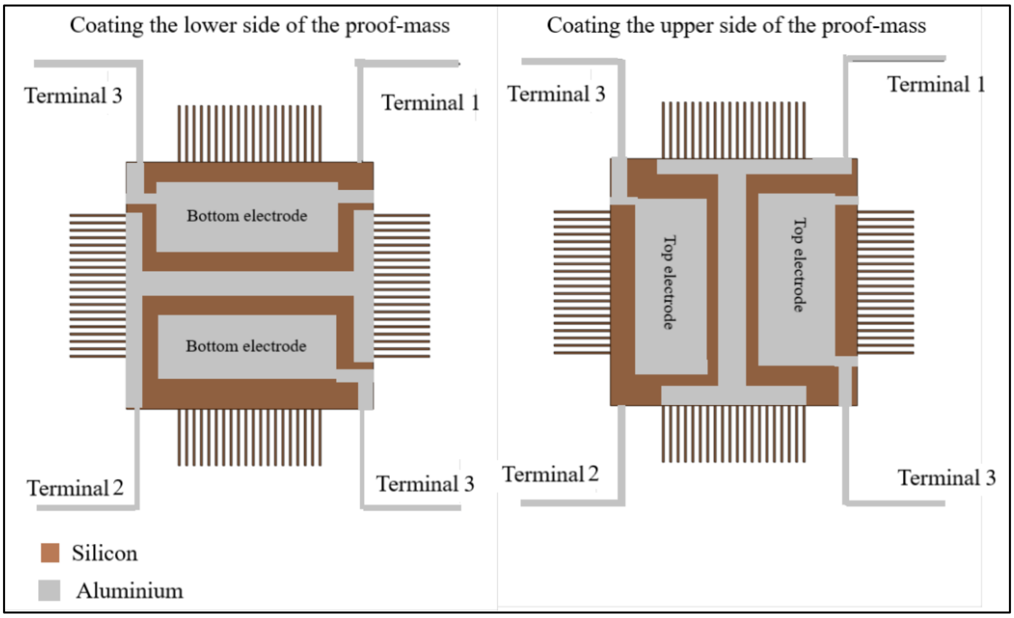

Figure 3.9 Proof mass connection of 2-D accelerometer

Thickness of aluminum is 100 nm. Terminal 1 is the output sense voltage sensing acceleration on x-axis. Terminal 2 is the output sense voltage sensing acceleration on y-axis. Terminal 3 is the output sense voltage sensing acceleration on z-axis.

3.7.1 Specifications of the accelerometer

The accelerometer is designed to sense the acceleration in three dimensions, the x and y dimensions, sensed by the sense fingers that are perpendicular to the direction of movement. The third dimension must be sensed by the upper two electrodes and the lower two electrodes. The sensing ranges -60g - 60g for three dimensions.

The proof mass is suspended in the center in a way that allows it to move when any acceleration and in all directions are applied to the structure. The motion of the proof mass causes a change in the distance between the electrodes, causing a change in the capacitance through which we can find the amount of acceleration.

The geometrical and physical parameters of the 3-D model are shown in table 3.5.

Table 3.5 Geometrical and physical parameters of the 3-D model

Parameters	**Design**
Device length	1100 µm
Device width	1000 µm
Device thickness	30 µm
Mass width W_1	500 µm
Mass length L_1	500 µm
Mass thickness H_1	10 µm
Beam length L_X	200 µm
Beam length L_Y	200 µm
Beams width W_2	3 µm
Beams thickness h_2	8 µm
Capacitance gap d_0	1 µm
Right finger length	120 µm
Left finger length	140 µm
Finger width	4 µm
finger thickness h_f	10 µm
Finger overlap length	100 µm
Number of sensing fingers	80 pair
Young’s Modulus E	160GPa
Spring constant $K_x = K_y$	16.3 N/m
Spring constant K_z total	19.17 N/m
The density of poly-Si	2320 kg/m^3

3.8 Material selection for 3-D model

Single-crystalline silicon (100) is chosen for the beams and proof-mass because its properties are as light as aluminum and have the same young's modulus as steel and the thermal expansion coefficient is much lower than that of steel making it dimensionally stable even at high temperatures

The proof mass should be coated with aluminum material .To take advantage of the conductive property. But it is coated in a special way .Where all the fingers of the x-axis sensing which installed on the proof-mass are connected to each other as well as the y-axis. while the electrodes of the z-axis, which are aluminum coating areas that connect with each other without prejudice to other connections. And the upper and lower part of the anchor plan for the sensor fingers and for the beams and from the sensor consists of silicon oxide in order to take advantage of the insulating property and to avoid static electricity. As for the sensor fingers and the upper and lower electrodes, they are made of aluminum.

3.9 Analytical design

3.9.1Mass of proof-mass (m)

The dimensions of the proof mass were selected with the dimensions of the beams to obtain the required accuracy, sensitivity, frequency and bandwidth of the sensor for three dimensions(x, y, and z).The designed dimension of this work is shown in table 3.6.

Table 3.6 the designed proof-mass dimension of 3-D model

Parameter	**Designed**
Length of Proof-mass L_1	500 µm
Width of Proof-mass W_1	500 µm
Thickness of Proof-mass H_1	10 µm
Number of finger N	80
Finger length L_f	114 µm

Thus

$$V = L_1 \times W_1 \times H_1 + N\,(L_f \times W_f \times h_f)$$

$$V = 500\times10^{-6} \times 500\times10^{-6} \times 10\times10^{-6} + 80(114 \times 4 \times 10) \times10^{-18}$$

$$V = 2.7944*10^{-12} m^3$$

Mass of proof-mass (m) = ρ. V (2.13)

$$= 2320\ kg/m^3 \times 2.5\times10^{-12}\ m^3 = 6.646\ \mu g$$

3.9.2 The initial force on the proof-mass of 3-D model

The initial force act on the proof-mass F, at apply acceleration 1 g is:

$$F = -m.a$$

$$F = 6.646 \times10^{-9} \times 1\times 9.8 = 6.513\times10^{-8} N$$

This force divided on four beams then the force per beam

$$F_{beam} = F/4 = 1.628 \times 10^{-8}\ N$$

3.9.3 The beams deflection

The beam attached with proof mass and another side fixed with anchor plan when applied acceleration on x-axis or y-axis the initial force causes move the proof mass causes deflection the beams, this deflection depend on spring coefficient k because of equal length of beams $L_x=L_y$ then equal coefficient $k_x=k_y$ and equal deflection $\delta_x=\delta_y$.

From equation (3.4)

$$\delta_x = \delta_y = \frac{\mathrm{F}_{beam} \times L_x^3}{12EI}$$

$$I=\frac{\mathrm{h}_2 \times W_2^3}{12} = 128 \times 10^{-24}\ \mathrm{m}^4$$

$$\delta_x = \delta_y = 0.0053\mu\mathrm{m}$$

From equation 2.8 the mechanical sensitivity S of the accelerometer is

$$\mathrm{S}=\frac{\mathrm{X}}{\mathrm{g}}$$

$$S_y = S_x = \frac{\mathrm{X}}{\mathrm{g}} = 0.0053\mu\mathrm{m/g}$$

For maximum deflection g =50 on x-axis or y-axis then

Maximum $\delta_x = 0.0053\mu\mathrm{m/g} \times 60\ \mathrm{g}$

Maximumδ_x =0.318 µm = Maximum δ_y

When the acceleration on z-axis the two beams are effective and the deflection equal to summation of deflection of the first beam plus deflection of second beam show figure 3.10.

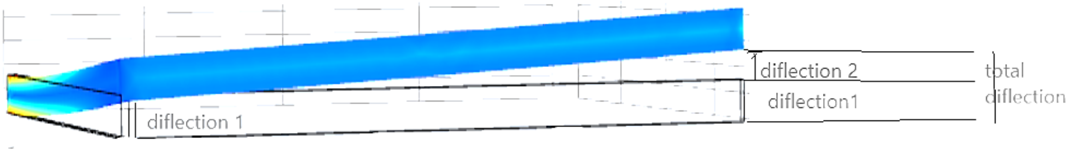

Figure 3.10 Shape of beams at acceleration on z-axis

The best method to calculate the deflection in this case is calculating constant of spring and then we can to calculate the deflection (displacement at 1 g acceleration on z-axis).

For one folded beam[19]

$$k=\frac{1}{2}E.h_2.(\frac{w_2}{L_X})^3 \tag{3.10}$$

For four folded beams

$$K_{Z\ Total}=2.E.w_2.(\frac{h_2}{L_X})^3$$

$$=15.36\ N/m$$

$$\delta_z = \frac{F}{k_z} = \frac{6.513 \times 10^{-8}}{15.36}$$

δ_z =0.00424 µm

From equation 2.8 the sensitivity s of the accelerometer for z-axis is

$$S= \frac{X}{g}$$

S_z =0.00424 µm/1g =0.00424 µm/g

Maximum deflection for z-axis $\delta_{z\ max} = 0.00424$ µm/g × 60

$\delta_{z\ max}$ =0.254 µm

3.9.4 Bending stress of the beam

The bending stress under simple bending in a beam is given using equation (3.5):

$$\sigma = \frac{M}{I} \times y$$

$$\sigma_x = \frac{M_x}{I_x} \times y$$

$M_x = M_Y = F \times Lx \times 60$

$M_x = 1.63 \times 10^{-8} \times 200 \times 10^{-6} \times 60$

$M_x = 1.956 \times 10^{-10}$ Nm

For maximum bending stress y = maximum displacement=1 µm

Thus

$$\sigma_x = \sigma_Y = \frac{1.956 \times 10^{-10}}{18 \times 10^{-24}} \times 1 \times 10^{-6}$$

$$\sigma_x = \sigma_Y = 10.867\ MPa$$

At acceleration of 60 g on z-axis

$M_Z = F \times (Lx + L_Y) \times 60$

$M_Z = 2 \times F \times Lx \times 60 = 2 \times 1.956 \times 10^{-10}$

$M_Z = 3.912 \times 10^{-10}$

$$\sigma_z = \frac{M}{I_z} \times y$$

$I_Z = \frac{w_2 \times h_2^3}{12} = 128 \times 10^{-24}$ m^4

For maximum bending stress $y = 1 \times 10^{-6}$

$$\sigma_z = \frac{3.912 \times 10^{-10}}{128 \times 10^{-24}} \times 1 \times 10^{-6}$$

$$\sigma_z = 3.05625\, MPa$$

3.9.5 Safety Factor

Safety factor is the ratio of the ultimate strength divided by the maximum stress that is in equation (3.6) :

Safety Factor =ultimate strength / maximum stress

From calculation the maximum stress when acceleration maximum on x-axis at 60 g and ultimate strength for silicon = 7000MPa

Thus

Safety Factor = ultimate strength / maximum stress (σ_x)

Safety Factor = 7000/10.867

= 644.152

3.9.6 Natural frequency

From equation 2.6

$$w_n = \sqrt{\frac{k}{m}}$$

$$f_n = \frac{1}{2\Pi} \sqrt{\frac{k}{m}}$$

From equation 3.7

$$K = \frac{F}{\delta}$$

From calculation $\delta_x = \delta_y$ then $k_x = k_y$ and same natural frequency but δ_z was different then $k_z \neq k_x$ and have different natural frequency.

$$k_x = \frac{F}{\delta_x} = \frac{6.52\times10^{-8}}{0.0053\mu m} = 11.8 \text{ N/m}$$

Thus

$$f_n = \frac{1}{2\Pi}\sqrt{\frac{11.8}{6.646\ \mu g}} = 6.706 \text{ kHz at acceleration on x and y axes}$$

At acceleration on z-axis

$$k_z = 15.36 \text{ N/m}$$

$$f_n = \frac{1}{2\Pi}\sqrt{\frac{15.36}{6.646\ \mu g}} = 7.655 \text{ kHz}$$

3.9.7 Accelerometer capacitance Sensitivity

Accelerometer Sensitivity for capacitive accelerometer is obtained from difference between tow sided capacitance, The air gap between movable finger and fixed finger is 1 µm and the capacitance for tow sided are equal and ΔC= 0 when applied 1 g acceleration The air gap was varied causes the capacitance in one side is increase and capacitance in other side is decrease.

From equation 2.11 for x-axis and y-axis

$$C_0 = \frac{N_f \in_0 . \in_r . A}{d}$$

$A = L_f \times h_f = 100 \times 10^{-6} \times 10 \times 10^{-6}$

$A = 1000 \times 10^{-12}\ m^2$

$$C_0 = \frac{40 \times 8.85 \times 10^{-12} \times 1 \times 1000 \times 10^{-12}}{1 \times 10^{-6}} = \quad 354\ fF$$

From equation 2.14

$$\Delta c = c_0 \left(\frac{1}{1 - \frac{X}{d}} - \frac{1}{1 + \frac{X}{d}}\right)$$

X is the displacement $= \delta x$ at 1g= 0.0053µm

Thus

$$\Delta c = 354 \left(\frac{1}{1 - 0.0053} - \frac{1}{1 + 0.0053}\right)$$

$\Delta c = 3.7724\ fF$

Capacitance sensitivity= $\Delta c / g$

Capacitance sensitivity for x-axis and y-axis=3.7724 f F/g

At acceleration on z-axis the capacitance between movable proof mass with top and bottom electrodes the air gap 1µm and when applied acceleration on z-axis the up gap is difference from down cap causing difference capacitance

Area of electrode $= 200 \times 10^{-6} \times 500 \times 10^{-6}$

$= 0.1 \times 10^{-6}\ m^2$

Thus

$$C_0 = \frac{8.85\times10^{-12}\times0.1\times10^{-6}}{1\times10^{-6}} = \quad 885 \text{ f F}$$

From equation 2.14

$$\Delta c = c_0\left(\frac{1}{1-\frac{X}{d}} - \frac{1}{1+\frac{X}{d}}\right)$$

X is the displacement $= \ \delta z$ at 1g$=0.0034$ µm

$$\Delta c = 885 \text{ f F } \left(\frac{1}{1-0.00424} - \frac{1}{1+0.00424}\right)$$

Δc =6.9 f F

Capacitance sensitivity= $\Delta c/g$

Capacitance sensitivity for z-axis =6.9 f F/g

4

Chapter Four

SIMULATION RESULTS

CHAPTER FOUR

SIMULATION RESULTS

4.1 FEM modeling and simulation

The Finite Element Method (FEM) is a general numerical method for solving partial differential equations in two or three space variables[45, 46]. It is a widely used for solving mathematical modeling equations that arise in engineering and mathematical modeling as well as areas of interest including mass transfer, structural analysis[47, 48], fluid flow, heat transfer, and electromagnetic potential.

To solve a problem, FEM breaks the large system into smaller and simpler parts. This is achieved through a specific estimation of space in the dimensions of space, which is carried out by creating a grid of the object[49, 50]. The FEM formulation of the boundary value problem eventually leads to the algebraic equations of the system. FEM approaches the unknown function in the field[51, 52].

Then the small equations representing these elements are combined into a bigger system of equations that represents the entire problem. Then FEM uses different methods to compute the differences to approximate the solution by reducing the associated error function[53-56].

Several FEM tools are commercially available for MEMS modeling and simulation such as Intellisuite [57], MEMS Pro [58], CoventorWare[12, 51, 59, 60], COMSOLMultiphysics[61], ..Etc. However, in this thesis COMSOLMultiphysics 5.5 was used to simulate three types of accelerometers, 1-D, 2-D, and 3-D.

4.2 Mesh convergence study

Mesh convergence study is determines how many elements in a model are required to guarantee the results of an analysis are not varied by changing the size of the mesh. Basically, system response will converge to a repeatable solution with increasing mesh density.

It is known that the higher the density of the mesh causes higher accuracy in the results. But when the density of the mesh is uniform, this leads to all the model points have the same density. The density of the mesh depends on the length of the element. This requires a large memory and a long time to solve a problem. But, when the mesh is distributed irregularly, the active places in the system will be high density and the size of the element is relatively small. While in the ineffective places the density is low and the size of the elements is relatively large.

The density of the mesh in the irregular distribution is depending on the followings:

1- Maximum element size.
2- Minimum element size.
3- Maximum element Growth rate.
4- Curvature factor.
5- Resolution of narrow regions.

4.3 Simulation of 1-D accelerometer

4.3.1 Mesh convergence study of 1-D accelerometer

Mesh convergence study of the 1-D model have a mesh parameters as shown in table 3.1.When an acceleration of 1g is applied to the model with different mesh parameters, as described in the previous section, the proof-mass displacement was calculated for each mesh. We noticed that when the density of the mesh is increases, the displacement will be increases too, which means increasing in measurement accuracy. However, at a certain limit of the number of elements, the displacement remains constant, as shown in Figure 4.1.

Table 4.1 Meshes convergence for 1-D model

Max. element (µm)	Min. element (µm)	Growth rate	Curvature factor	Resolution of narrow region	No. of element	Displacement (µm)
171	36	1.7	0.8	0.3	12108	0.004046
135	25.2	1.6	0.7	0.4	17648	0.004883
90	16.2	1.5	0.6	0.5	24090	0.008512
72	9	1.45	0.5	0.6	55501	0.008901
50	3.6	1.4	0.4	0.7	94762	0.008991
31.5	3	1.35	0.3	0.85	147045	0.00903
18	2	1.3	0.2	1	274771	0.009067
9	1	1.25	0.1	1	474834	0.009067

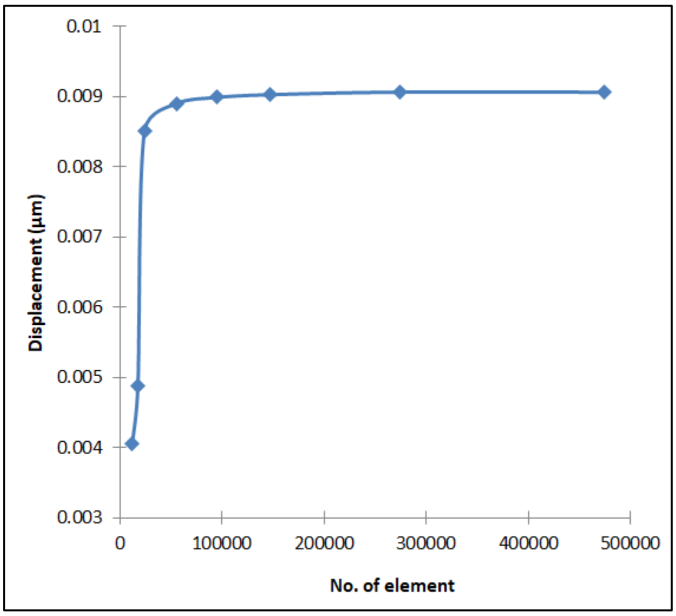

Figure 4.1 Mesh convergence simulation result of 1-D accelerometer

From figure 4.1, we can see that at a number of elements of 94762 elements and more, for the frame structure of the accelerometer, the variation in the proof mass displacements are less than 1%, and then the convergence was achieved.

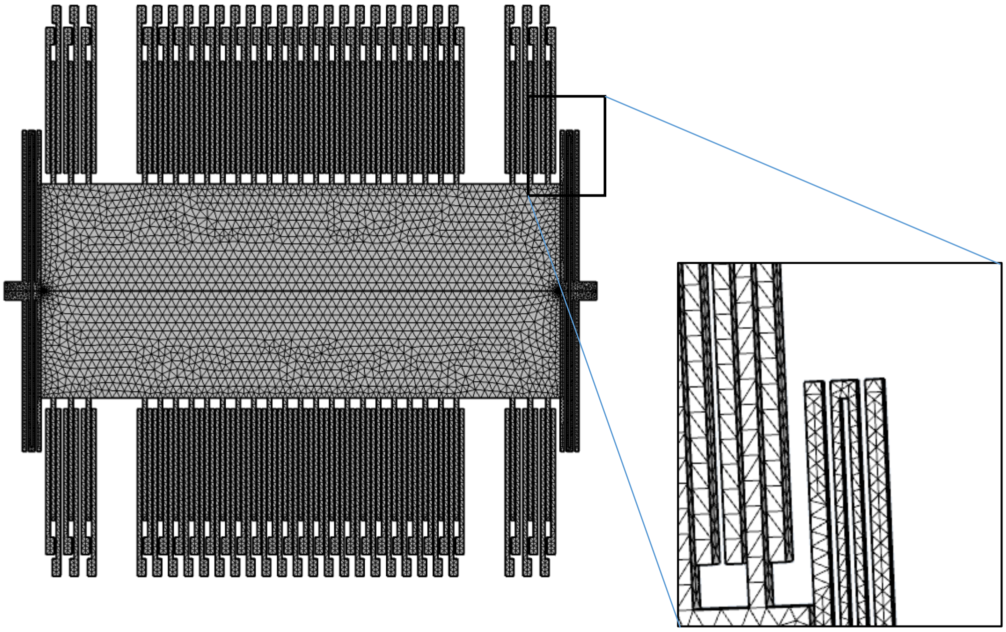

Figure 4.2 Meshed model of 1-D accelerometer structure

4.3.2 Acceleration vs. displacement of the 1-D accelerometer

To simulate the device, acceleration ranges from 0 g to 60 g with a step of 5 g are applied to the 1-D accelerometer. The displacements from 0 g to 60 g on the x-axis were obtained as output. Then acceleration ranges from (-60 g to 0 g) with a step of 5 g are applied to the 1-D accelerometer. The displacements from -60 g to 0 g were obtained as output. The surface displacements of every point of 1-D model at acceleration of 60 g are shown in figure 4.3.

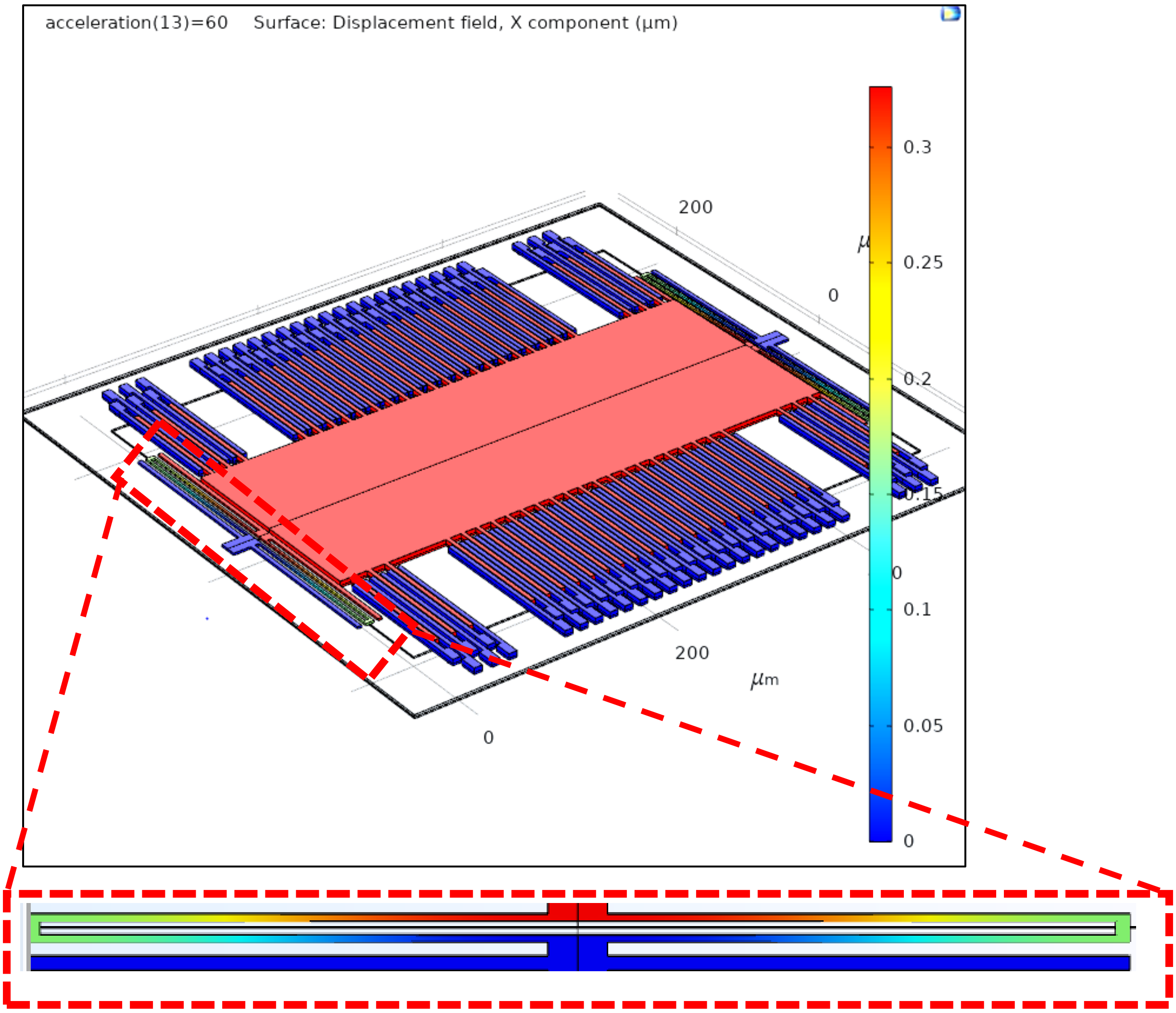

Figure 4.3 Surface displacement of 1-D model at acceleration of 60 g

Table 4.2 and figure 4.4 show the displacement as a function of acceleration x = f(g) and the relationships is linear between acceleration and proof-mass displacement.

Table 4.2 Acceleration vs. displacement of proof-mass of 1-D model

Acceleration (g)	**Displacement (μm)**	**Displacement (μm) at - g**
0	0	0
5	0.027182269	-0.02718
10	0.054364533	-0.05436
15	0.081546792	-0.08155
20	0.108729045	-0.10873
25	0.135911291	-0.13591
30	0.16309353	-0.16309
35	0.190275761	-0.19028
40	0.217457984	-0.21746
45	0.244640198	-0.24464
50	0.271822403	-0.27182
55	0.299004599	-0.299004
60	0.326186785	-0.32619

The maximum displacement equal to 0.326186785 μm at applies acceleration of 60 g.

From equation 2.8

The mechanical sensitivity S= 0.0054

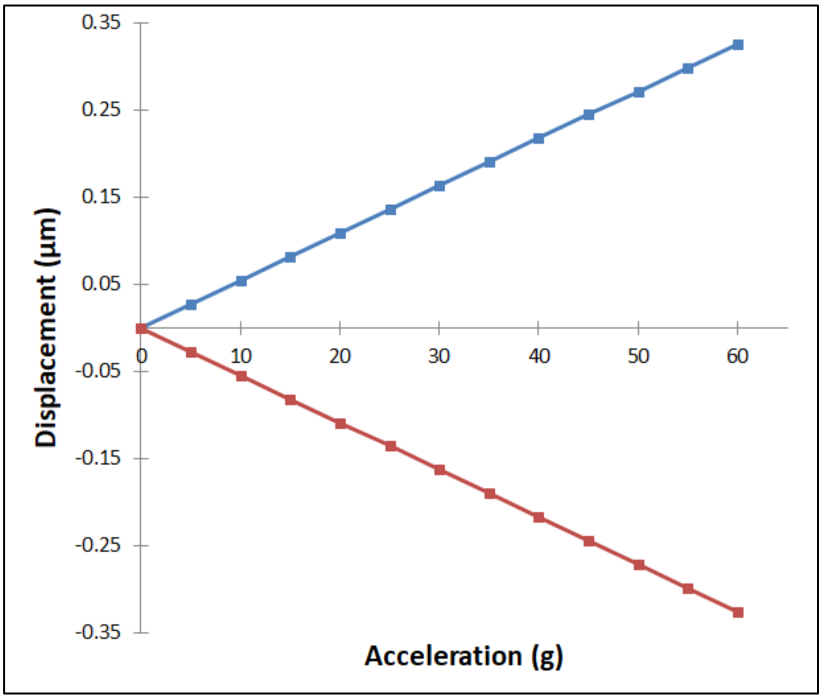

Figure 4.4 Acceleration vs. displacement of the 1-D accelerometer

4.3.3 Acceleration vs. ΔC of the 1-D accelerometer

Accelerometer Sensitivity for 1-D capacitive accelerometer is obtained from difference between tow sided capacitance. The air gap between movable finger and fixed finger is 1 µm and the capacitance for two sided at 0 g are equal and ΔC= 0. When applied acceleration from 0 g to 60 g step 5g to the 1-D accelerometer. For negative acceleration, acceleration from -60g to 0g with step 5g is applied to the 1-D accelerometer. The differences between two sided capacitance ΔC are obtained as output.

The air gap was varied causes the capacitance in one side is increase and capacitance in other side is decrease causes ΔC increase. Table3.5 and figure3.7 below is the simulation results.

Table 4.3 Acceleration and difference capacitance of 1-D accelerometer

Acceleration (g)	**ΔC (fF)**	**ΔC (fF) at -g**
0	0	0
5	12.13318	-12.1332
10	24.32031	-24.3203
15	36.61613	-36.6161
20	49.07704	-49.077
25	61.76192	-61.7619
30	74.73312	-74.7331
35	88.05757	-88.0576
40	101.8079	-101.808
45	116.0641	-116.064
50	130.915	-130.915
55	146.4603	-146.46
60	162.8134	-162.813

From equation 2.15

Capacitance sensitivity $= \Delta c/g$

Capacitance sensitivity $= 2.418 \quad fF/g$

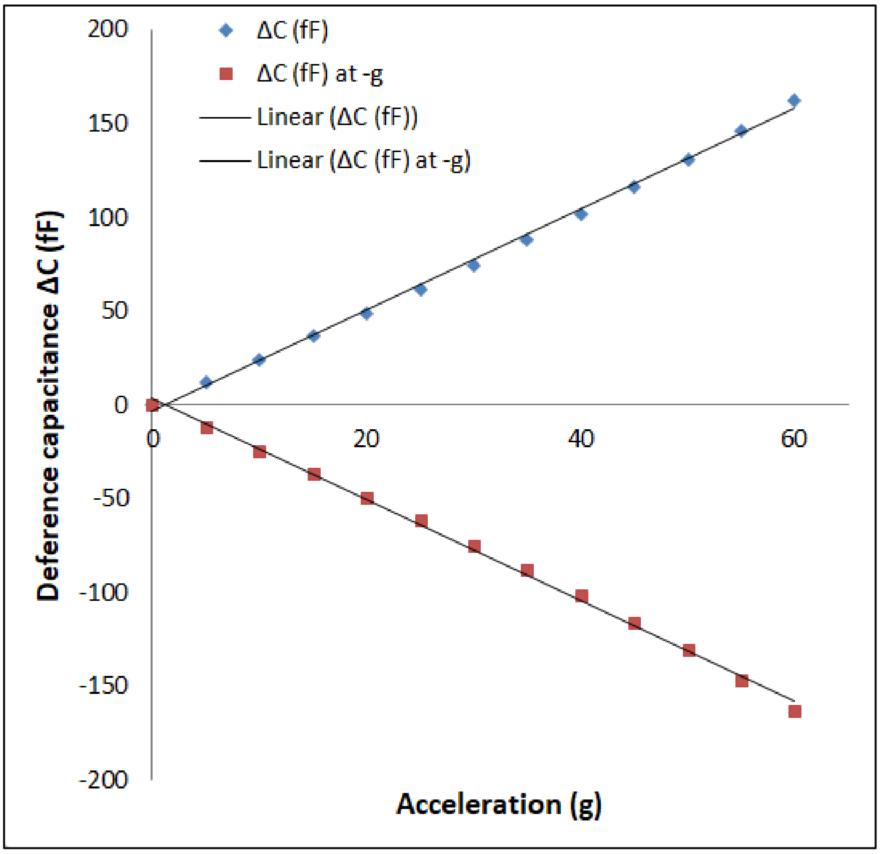

Figure 4.5 Acceleration vs. difference of capacitance of 1-D acceleration

From figure 4.5 it is clear the relationship between acceleration and difference of capacitance is nonlinearity but it is close to a linear relationship.

4.3.4 Bending stress of 1-D accelerometer

Stress in the beams occurs when acceleration is applied to the accelerometer. The stress is distributed irregularly. In a certain areas the stress is relatively high while it is relatively low in others according to the shape of the beams and the direction of acceleration. Calculating the maximum stress is important, as each subject has a certain level of stress tolerance. The model must be designed so that the maximum stress due to acceleration is less than the maximum stress that the material can withstand (UTS). For silicon material UTS is 7000 MPa.

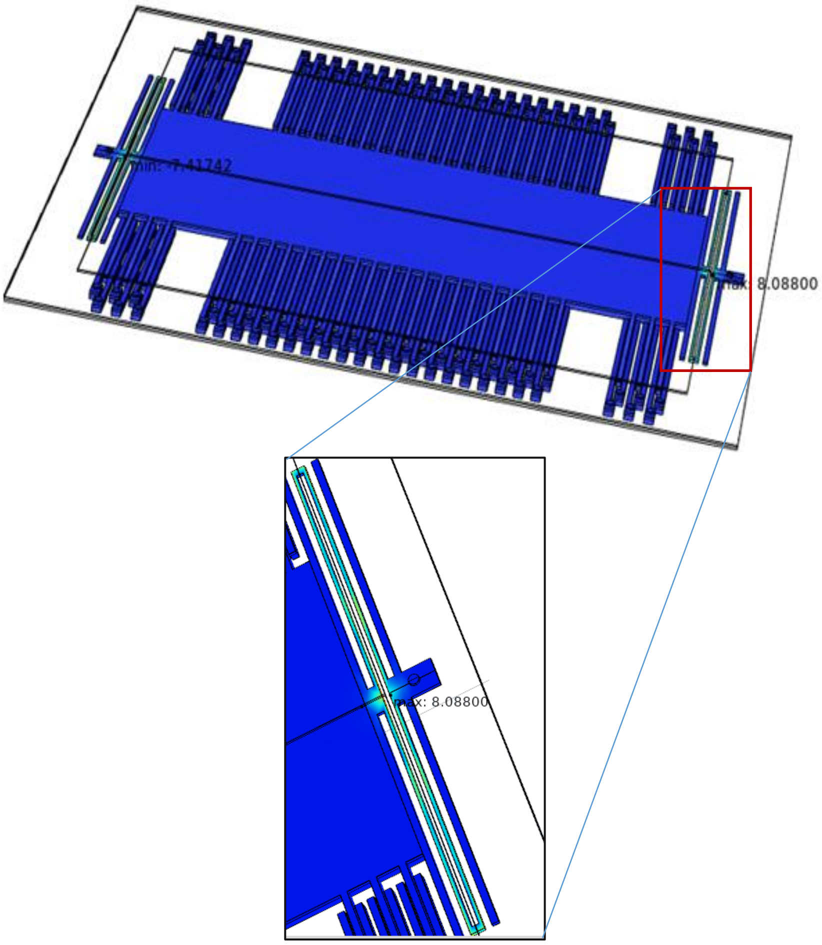

Figure 4.6 Surfaces and max. Stress in 1-D model

From figure 4.6 the simulation result for maximum stress is 8.088 MPa. The maximum stress occurs at corner point of the beam as shown in figure 4.6.

4.3.5 Time response of 1-D accelerometer

Time response is done to estimate the device transient analysis to the applied acceleration input to the model.

4.3.5.1 Time response of low range acceleration input

Low range acceleration (0.01g-1g) is applied on the structure to measure rising time, damping ratio, and resolution. The displacements are calculated in the time from 0 s to 1.2 ms. with step 0.025. Using time-dependent in COMSOL Multiphasic 5.5. Figure 4.2 is the results of time response of the device.

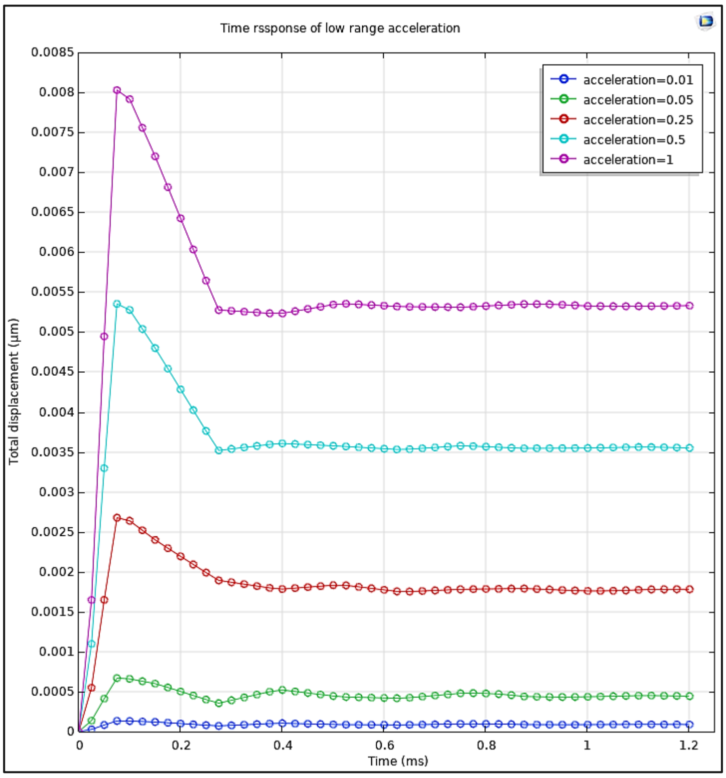

Figure 4.7 Time response of the 1-D device of low range acceleration

Referring to figure 4.7 we obtained:

$\xi = 0.2542$ and $w_n = 42578.4$ rad / s

The rise time =0.05 ms

The device has high resolution approximately 0.05 g

4.3.5.2 Time response of high range acceleration input

High range acceleration input (96 g-118 g) is applied on the 1-D model. In a time from 0 s to 1.2 ms. with step of 0.025 ms by using time-dependent in COMSOLMultiphysics 5.5. The result is shown in figure 4.3 to measure Maximum value of acceleration before the device gets a damaged the results are shown in figure 4.8.

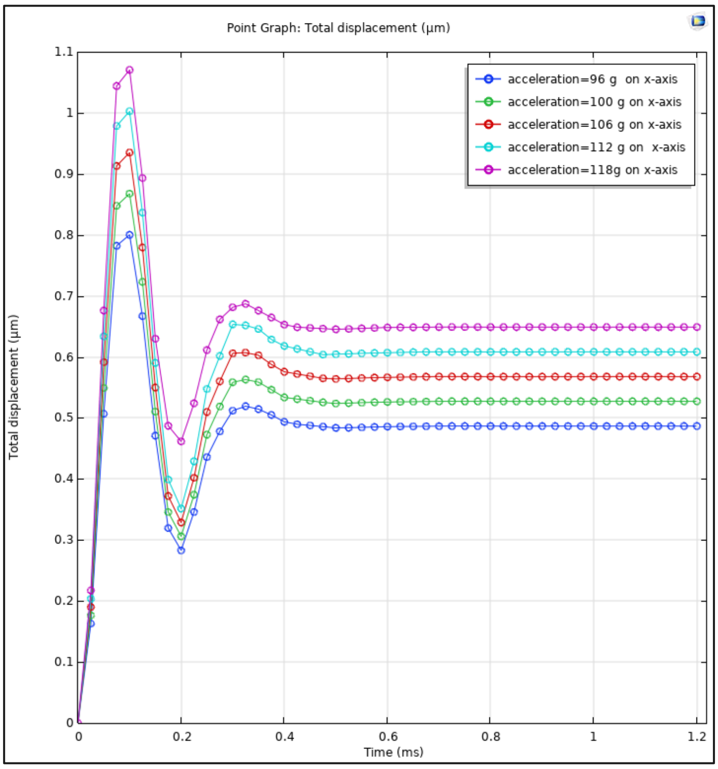

Figure 4.8 Time response of the 1-D device of high range acceleration

The highest acceleration that can be measured before the device gets damage is the acceleration that causes the full displacement. That causes short circuit between the moving fingers and the fixed fingers. From the figure 4.8, when the acceleration is 112 g, the excessive displacement equal to 1 micrometer, which causes the device to get damage and the capacitance equal to zero as shown in Figure 4.9.

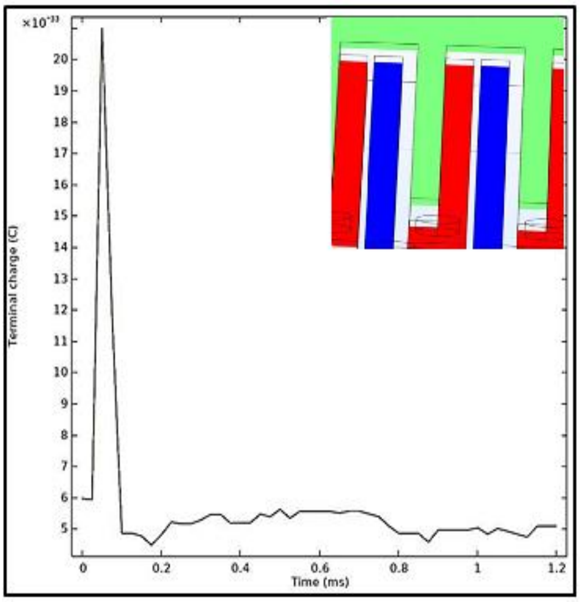

Figure 4.9 Capacitance vs. time in case of very high acceleration. Inset is the snapshot of the 1-D device at the collapse

4.3.6 Frequency response

Frequency response is done to estimate the device sensitivity and frequency to applied acceleration input. Acceleration from 0g to 50g with step of 10g are applied on the 1-D accelerometer with frequency by using frequency domain in COMSOL Multiphasics 5.5. Figure 4.5 is the results of frequency response.

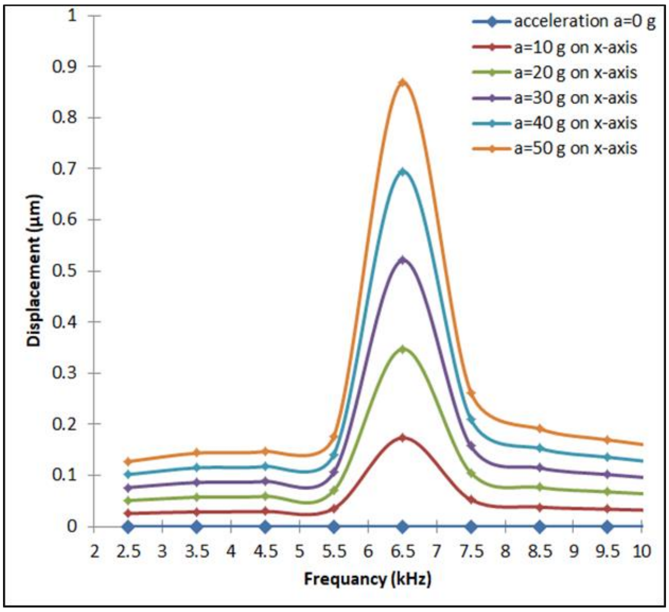

Figure 4.10 Frequency responses of 1-D model

From figure 4.10 center frequency equal to 6.5 kHz with band width approximately more than 1000 ∓ 100 Hz.

4.3.7 Output dc voltages vs. acceleration of 1-D accelerometer

Applying an alternating input voltage on the sensor fingers, for long fingers applied V_{in}, and for short fingers applied $-V_{in}$. The sensing signal is the proof-mass voltage. The amplitude of sensing signal depends on the amount of the acceleration. Therefore, the sensing signal is considered as amplitude modulating AM signal .To find the output dc voltage, coherent detector technique was used. The equivalent electrical circuit of the sensor is shown in figure 4.11.

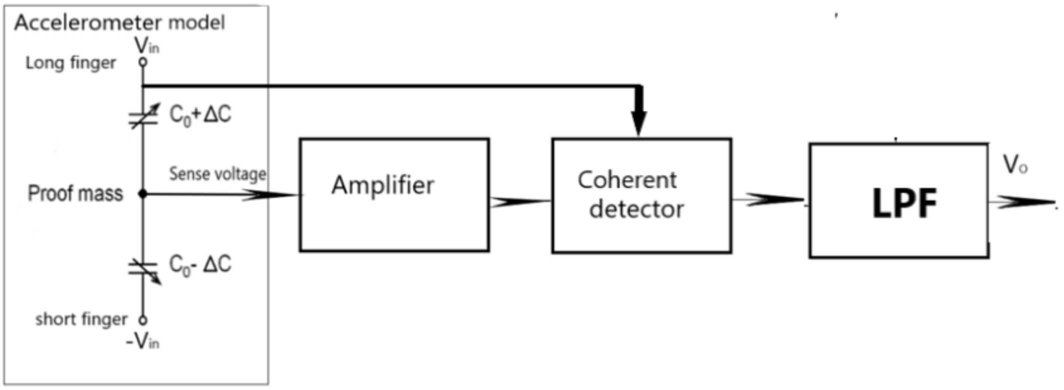

Figure 4.11 The equivalent electrical circuit of the sensor

$$\text{sense voltage} = V_{in}.\frac{\Delta C}{C_1 + C_2}$$

The sensing signal from COMSOL Multiphasics 5.5 of 1-D model, when V_{in} is 2 V (peak voltage) with 300 Hz is shown in figure 4.12.

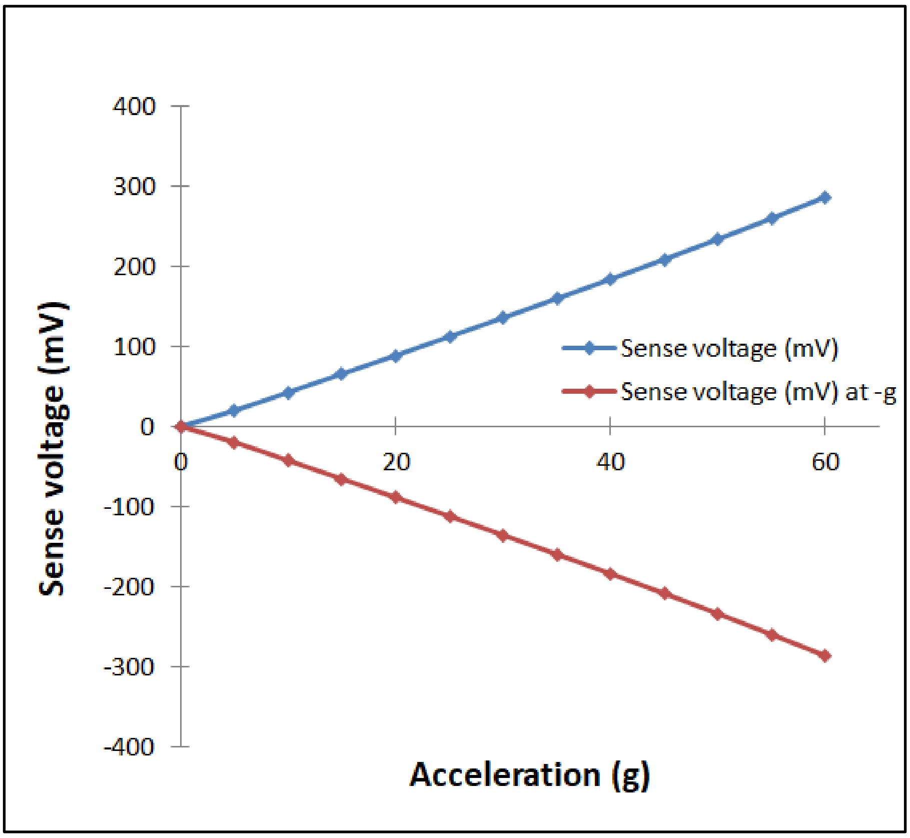

Figure 4.12 The sense voltage vs. acceleration of 1-D model

To complete the simulation result of the output dc voltage, matlab Simulink for amplifier, coherent detector, and LPF circuits were used, as shown in figure 4.13.

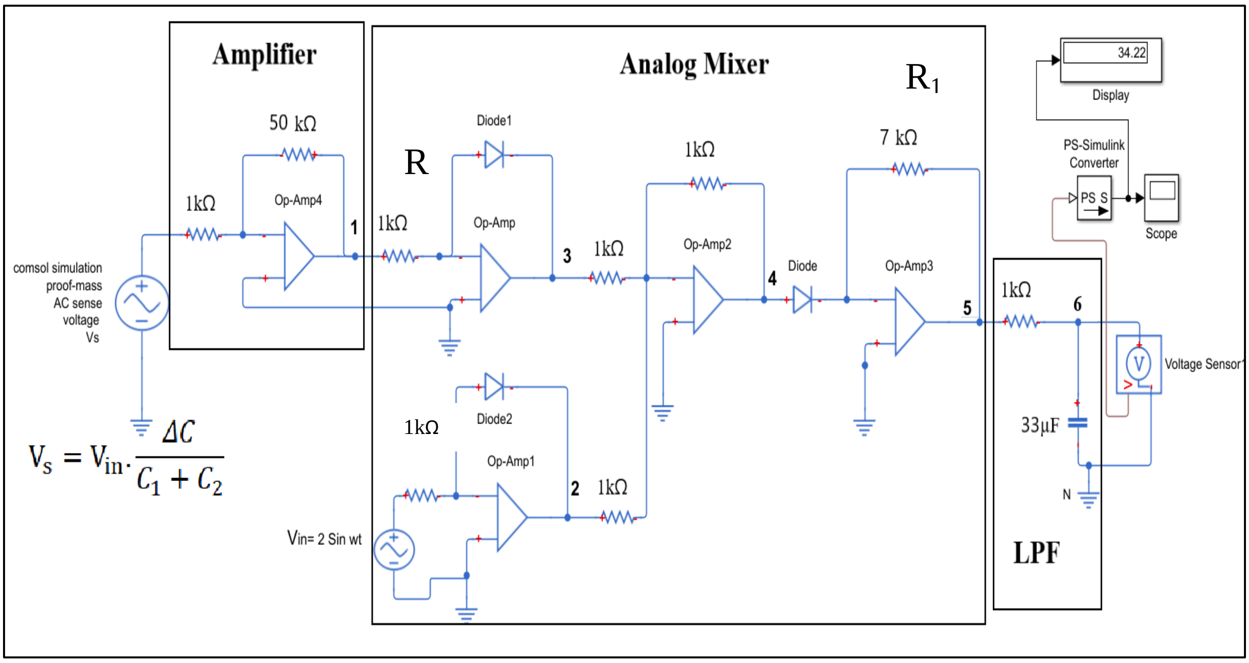

Figure 4.13 Electronic circuit of 1-D accelerometer

$$V_1 = -50\ V_s \quad = -\ \frac{100.\Delta C}{C_1+C_2}\sin wt$$

$$V_2 = -\ V_T\ \ \mathrm{Lin}\ (\frac{2\sin wt}{I_S R})$$

Where, I_S is the reverse bias saturation current,

V_T is the thermal voltage

$$V_3 = -\ V_T\ \mathrm{Lin}\ \left(\frac{-100\times\Delta C}{I_S R(C_1+C_2)}\sin wt\right)$$

$$V_4 = -V_T[\ \mathrm{Lin}\ \left(\frac{-100\times\Delta C}{I_S R(C_1+C_2)}\sin wt\right) +\ \mathrm{Lin}\ (\frac{2\sin wt}{I_S R})]$$

$$V_4 = -V_T \mathrm{Lin}\ \left(\frac{-200\times\Delta C}{R^2 {I_S}^2 (C_1+C_{2)}}\sin^2 wt\right)$$

$$V_5 = -I_S R_1 \mathrm{Lin}^{-1}\left(\frac{V4}{V_T}\right)$$

$$V_5 = I_S R_1 \mathrm{Lin}^{-1}\mathrm{Lin}\ \left(\frac{-200\times\Delta C}{R^2 {I_S}^2 (C_1+C_{2)}}\sin^2 wt\right)$$

$$V_5 = \frac{R_1}{I_S \times R^2}\left(\frac{-200\times\Delta C}{(C_1+C_2)}\sin^2 wt\right)$$

$$I_S = 11\text{mA}$$

$$V_5 = \frac{120\times\Delta C}{C_1+C_2}\left(\frac{1}{2}+\frac{1}{2}\cos 2\,wt\right)$$

LPF is cut the AC part thus;

$$V_0 = V_6 = \frac{60\times\Delta C}{C_1+C_2}$$ It is DC output voltage

The amplifier has overall gain 25 dB at frequency of 100 Hz. The frequency response with gain in (dB) is shown in figure 4.14.

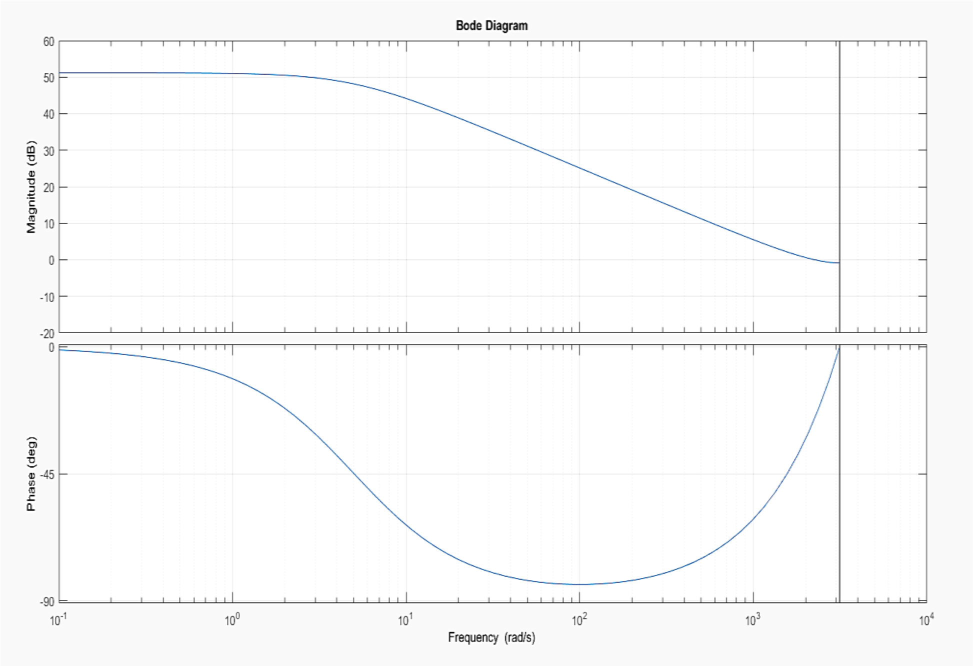

Figure 4.14 Frequency response of electronic circuit

The signals flows in the electronic circuit at acceleration of 60 g are shown in figure 4.15.

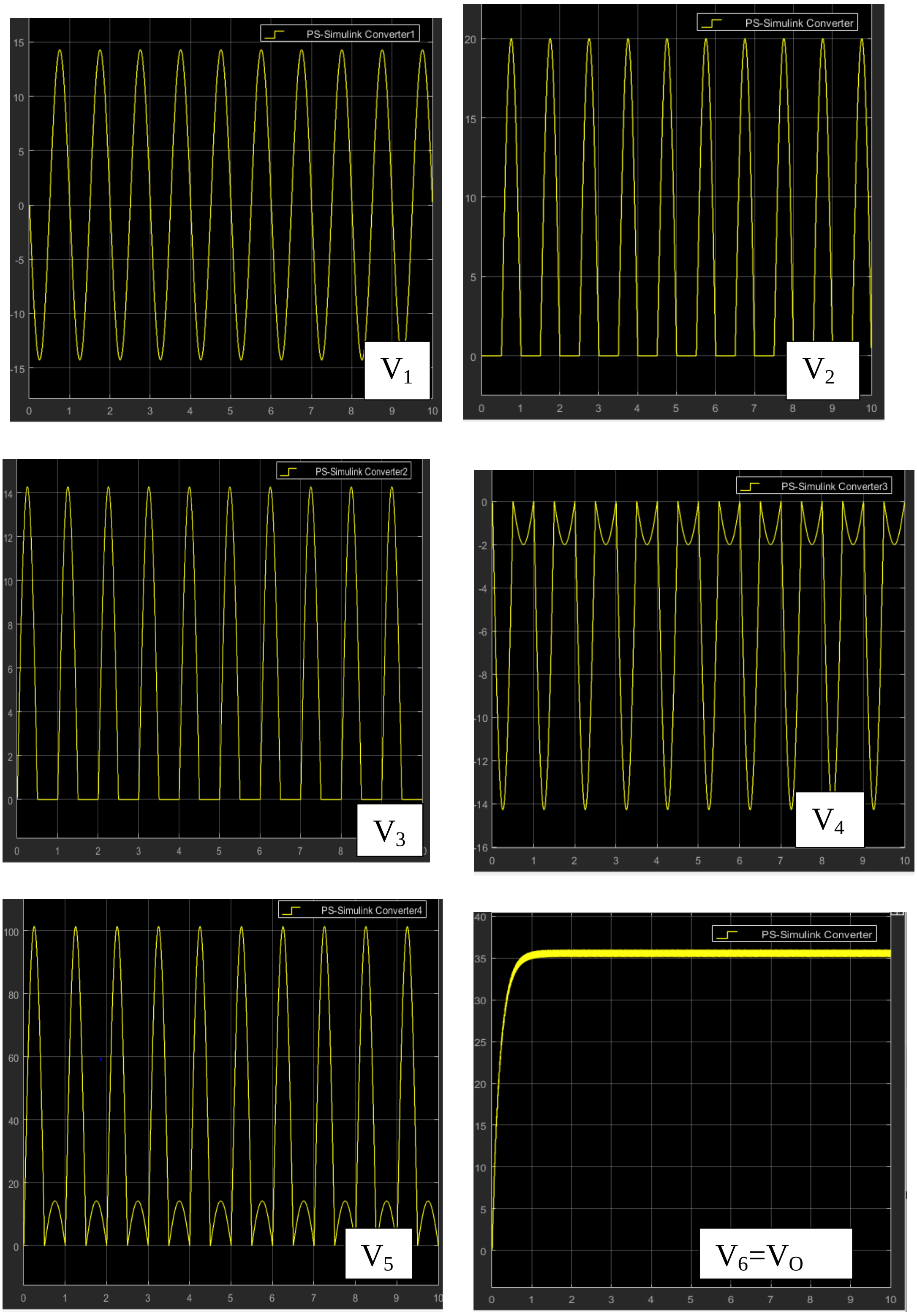

Figure 4.15 The signals flow in the electronic circuit at acceleration of 60 g

The signals flows in the electronic circuit at acceleration of -60 g are shown in figure 4.16.

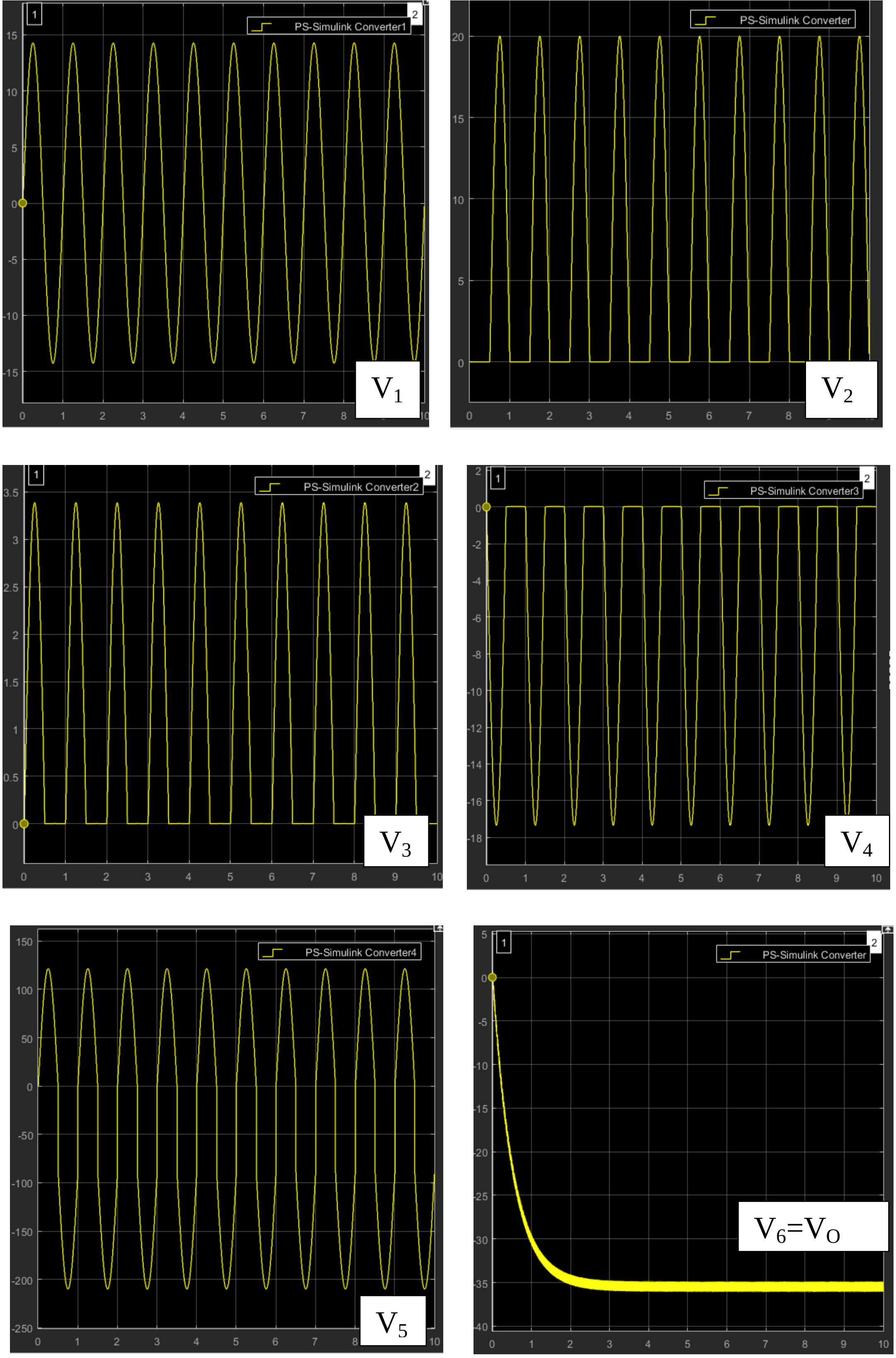

Figure 4.16 The signals flow in the electronic circuit at acceleration of -60g

The output dc voltage vs. acceleration is shown in figure 4.17.

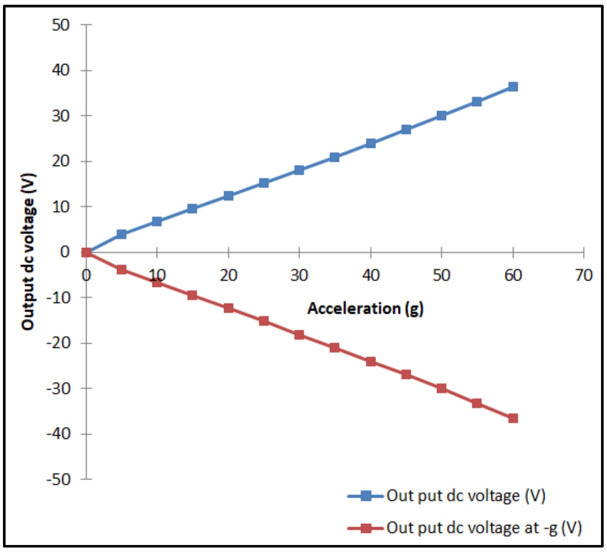

Figure 4.17 Output dc voltages vs. acceleration of 1-D accelerometer

The output dc voltage sensitivity of 1-D accelerometer is equal to 0.607 V/g.

4.4 Simulation design of 2-D accelerometer

4.4.1 Mesh convergence study of 2-D accelerometer

Mesh convergence study of the 2-D model have a mesh parameters as shown in table 4.4. An acceleration of 1g is applied to the model with different mesh parameters, as described in the section 4.2; the proof-mass displacement was calculated for each mesh.

Mesh convergence study of the model have the parameters shown in table 4.4.

Table 4.4 Meshes convergence study for 2-D model.

Max. element (µm)	**Min. element (µm)**	**Growth rate (µm)**	**Curvature factor**	**Resolution of narrow region**	**No. of elements**	**Displacement (µm)**
450	63	2	1	0.1	7724	0.004264
270	48.6	1.85	0.9	0.2	10975	0.004672
171	36	1.7	0.8	0.3	14314	0.005082
135	25.2	1.6	0.7	0.4	22061	0.005293
90	16.2	1.5	0.6	0.5	29327	0.005539
72	9	1.45	0.5	0.6	52240	0.005831
50	3.6	1.4	0.4	0.7	113156	0.005885
31.5	1.35	1.35	0.3	0.85	202472	0.005906
18	0.18	1.3	0.2	1	374834	0.005922

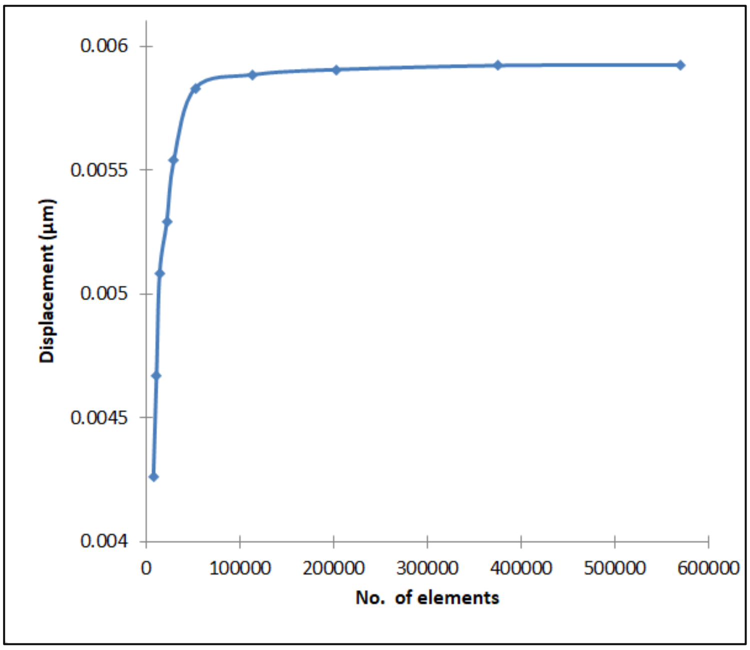

Figure 4.18 Mesh convergence of 2-D model

From figure 4.18, we can see that at a number of elements of 202472 elements and more, for the frame structure of the accelerometer, the variation in the proof mass displacements are less than 1%, and then the convergence was achieved**.**

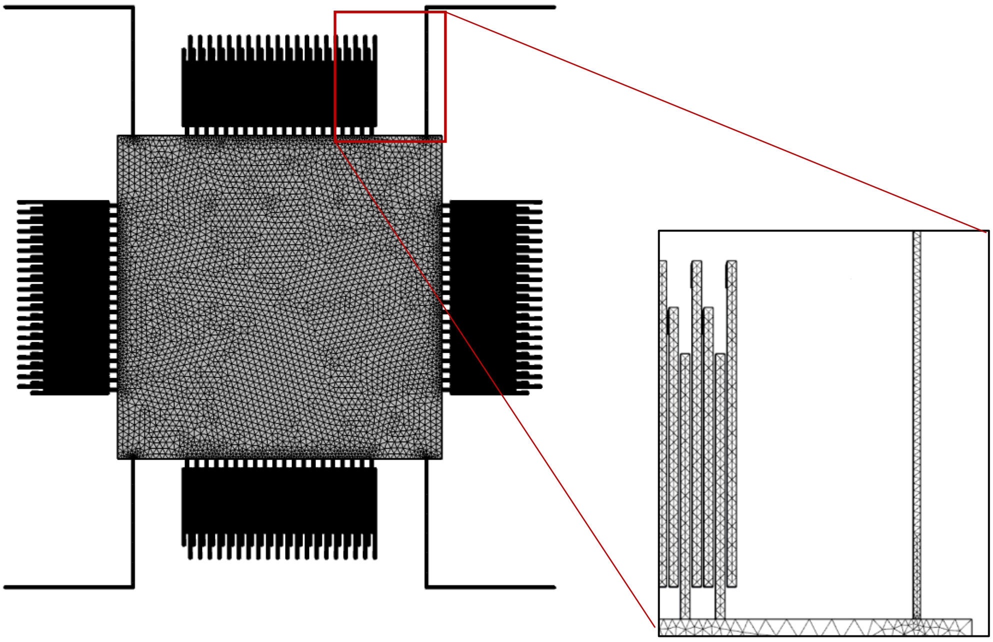

Figure 4.19 Meshed model of 2-D accelerometer structure

The shapes of the elements at mesh density of 202472 elements are tetrahedral elements as shown in figure 4.19. It is clear how elements are distributed. In the effected regions, the elements are small enough with high number of elements as in fingers and beams. While in the other ineffective regions the size of the elements are relatively bigger.

4.4.2 Acceleration vs. displacement of 2-D accelerometer

To simulate the 2-D accelerometer device, acceleration ranges from (0 g to 60) g with a step of 5 g were applied and the displacements from (-60 g to 0 g) on the x-axis were obtained. The same procedures were used for the acceleration on the y-axis.

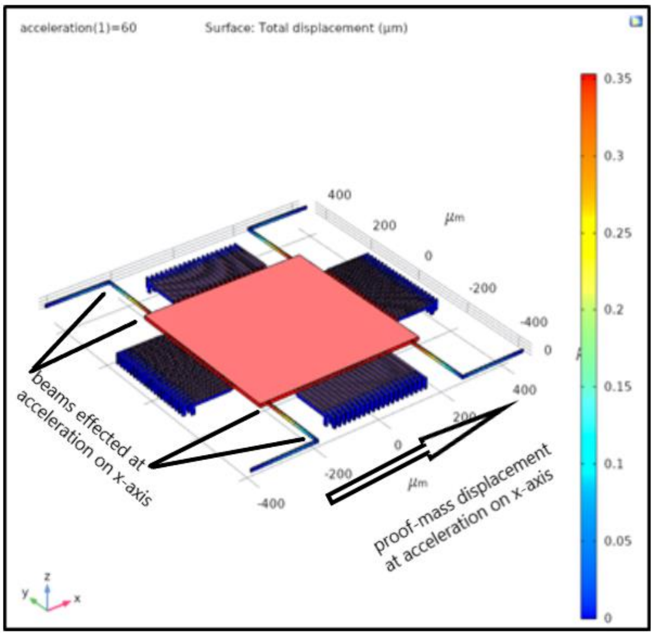

Figure 4.20 Surface displacement when acceleration on the x-axis of 2-D model

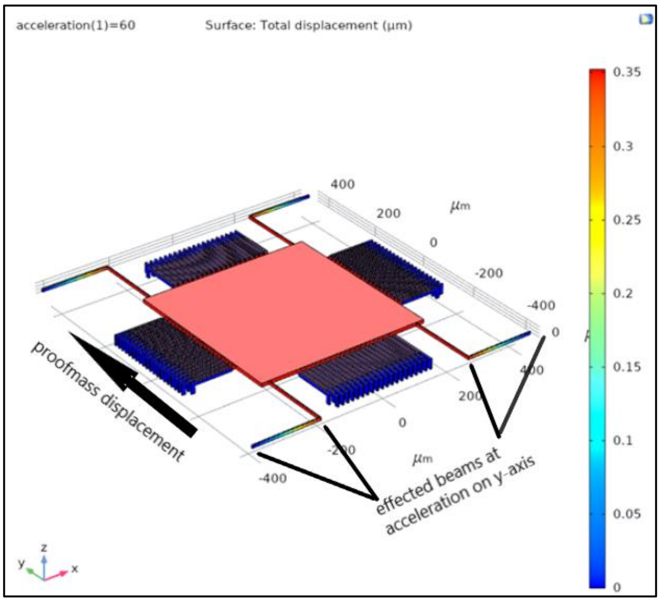

Figure 4.21 Surface displacement when acceleration on the y-axis of 2-D model

From figure 4.20 and 4.21 the beam causing the displacement, which the stress occurs in the perpendicular beam. While the other beam is stay fix without any stress.

When accelerating in the direction on Y axis, the beam causing the displacement and the stress occurs is the horizontal beam, and the other beam continuous to move with proof mass without any stress.

The results of the simulation are shown in figure 4.22, and table 4.5.

Table 4.5 Acceleration on x-axis vs. displacement of proof-mass of 2-D model

Acceleration (g)	**Displacement (µm)**	**Displacement at -g (µm)**
0	0	0
5	0.029415663	-0.029415663
10	0.058831317	-0.058831317
15	0.088246956	-0.088246956
20	0.117662573	-0.117662573
25	0.147078161	-0.147078161
30	0.176493716	-0.176493716
35	0.205909229	-0.205909229
40	0.235324695	-0.235324695
45	0.264740108	-0.264740108
50	0.294155461	-0.294155461
55	0.323571007	-0.323571007
60	0.352986553	-0.352986553

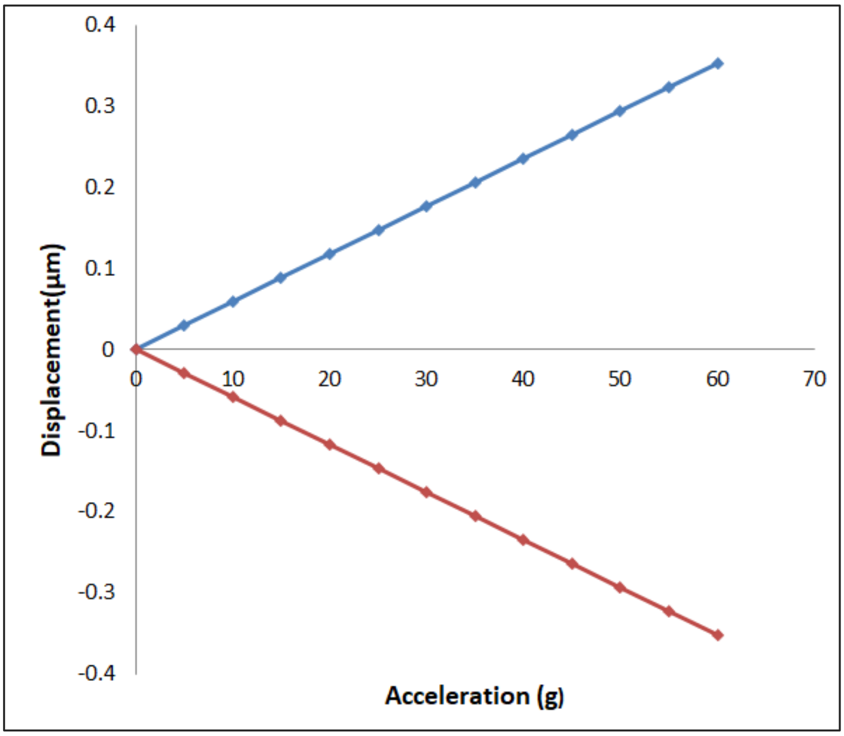

Figure 4.22 Acceleration vs. Proof mass displacement of 2-D model

Table 4.5 and figure 4.22 show the displacement as a function of acceleration X= f(g) and the relationship is a linear between acceleration and proof mass displacement. From equation 4.8:

Mechanical sensitivity S= 0.005436 µm/g

The maximum displacement equal to 0.326186785 µm at applies acceleration of 60 g.

4.4.2 Acceleration vs. capacitance of 2-D accelerometer

The air gap between movable finger and fixed finger is 1 µm and the capacitance for two sided at 0 g are equal and ΔC= 0. When applied acceleration from 0 g to 60 g step 5g as input to the 2-D model. For negative acceleration applied from -60g to 0g with step 5g as input to the

2-D model. The differences between two sided capacitance ΔC are obtained as output.

The air gap was varied causes the capacitance in one side is increase and capacitance in the other side is decrease causes ΔC increase. Table 4.6 are the simulation results.

Table 4.6 Acceleration on x-axis with capacitances and difference capacitance of 2-D model

Acceleration (g)	C_1 (fF)	C_2 (fF)	ΔC(fF)	ΔC at -g (fF)
0	353.89	353.89	0	0
5	364.6154	343.7775552	20.83785	-20.8378
10	376.0112	334.2269862	41.78425	-41.7843
15	388.1424	325.1927314	62.94965	-62.9497
20	401.0824	316.6340259	84.44836	-84.4484
25	414.9149	308.5142861	106.4006	-106.401
30	429.7356	300.8005868	128.9351	-128.935
35	445.6543	293.4632155	152.1911	-152.191
40	462.7977	286.4752897	176.3224	-176.322
45	481.3128	279.8124277	201.5004	-201.5
50	501.371	273.4524643	227.9186	-227.919
55	523.1739	267.3751526	255.7988	-255.799
60	546.9593	261.5620969	285.3972	-285.397

From equation 2.15

Capacitance sensitivity $= \Delta c/g = 4.16 \quad fF/g$

4.4.3 Bending stress of 2-D accelerometer

An acceleration of 60 g in the direction of the x-axis is applied to the 2-D model. The surface stress and maximum stress are shown in Figure 4.23.

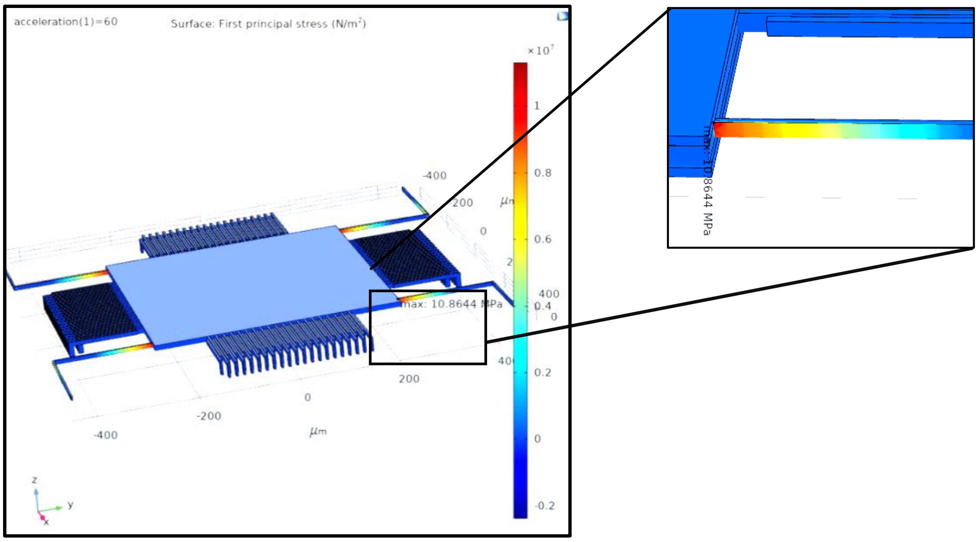

Figure 4.23 Bending stress for x-axis of 2-D accelerometer

From simulation, the maximum stress occurs at the point of contact of the beam with the proof mass, as shown in figure 4.23. The obtained magnitude was 10.8644 MPa, which is very low compared to UTS (7000 MPa). This means that the safety factor is high.

For y-axis, an acceleration of 60 g in along the y-axis was applied to the model. The surface stress and maximum stress are shown in Figure 4.24. The magnitude of maximum stress was 10.7986 MPa, which is equal to the maximum stress when the acceleration was applied on x-axis.

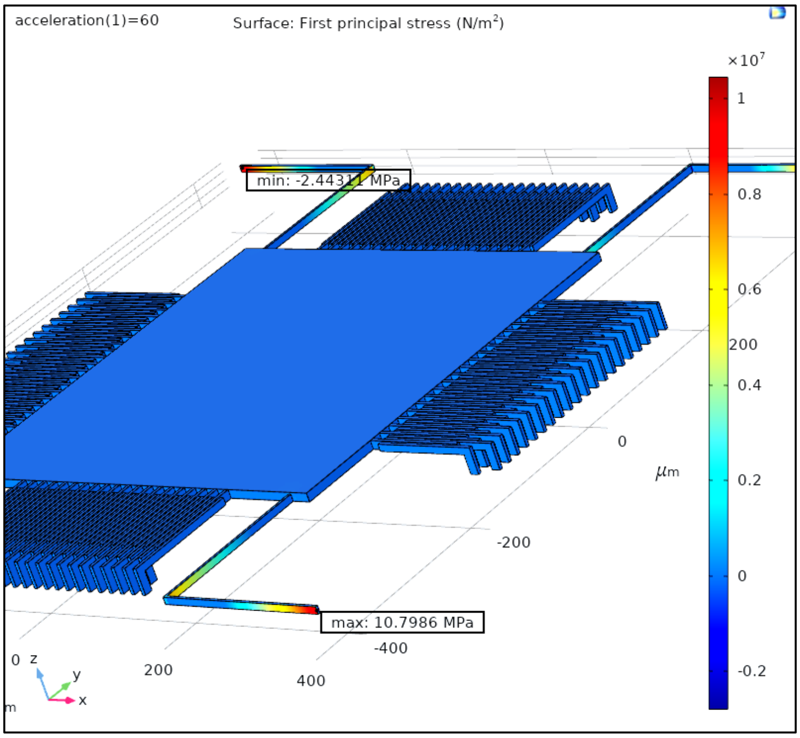

Figure 4.24 Bending stress for y-axis of 2-D accelerometer

From simulation the maximum stress occurs at the point of contact the beam with the anchor plan, as shown in figure 4.24.

4.4.5 Time response of 2-D accelerometer

Time response was done to estimate the 2-D accelerometer transient analysis to the applied acceleration input.

4.4.5.1 Time response of low range acceleration input

Low range acceleration (0.01g-0.5g) is applied on the structure in times from 0 s to 1.2 ms. with step 0.025 ms for x-axis and y-axis to measure rising time, damping ratio, and resolution. To simulation the device for acceleration on x and y axes used time-dependent key in COMSOL Multiphasic 5.5. Because of the lengths of the two beams (Lx, L_Y) are equal, then the same results for the x and y axis. The simulation results are shown in figure 4.25 for acceleration on x and y axes.

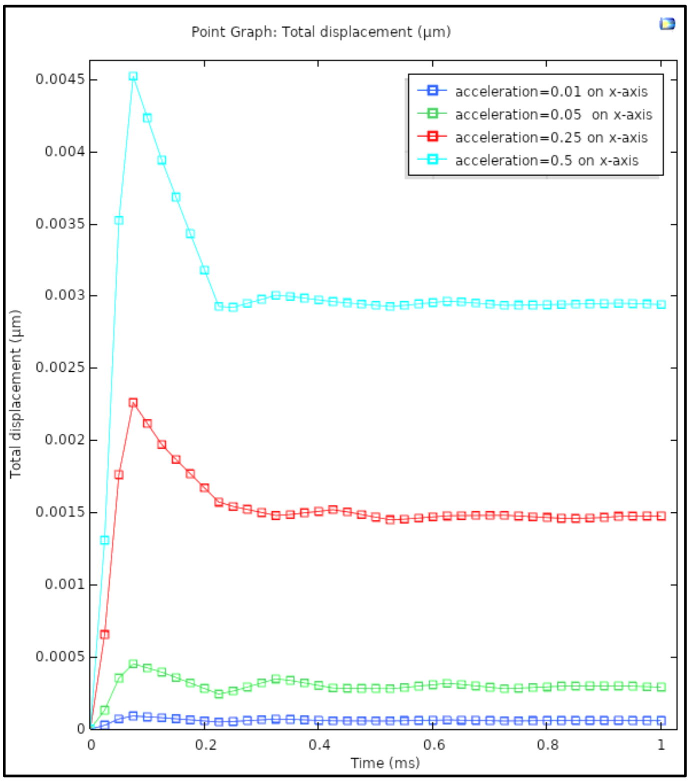

Figure 4.25 Time response of low range acceleration input for 2-D accelerometer

The simulation results are:

$\xi = 0.2251$

$w_n = 42980.32$ Rad/s

And the rise time = 0.035 ms

Device has high resolution approximately 0.05 g

4.4.5.2 Time response of high range acceleration input

High range acceleration input (90 g-96 g) for x and y axis was applied on the structure to measure Maximum value of acceleration before the device gets a damaged. In a time from 0 s to 1.2 ms. with a step 0.025 ms by using time-dependent in COMSOLMultiphysics 5.5. Figure 4.26 and Figure 4.27 are the results of time response of high range acceleration input.

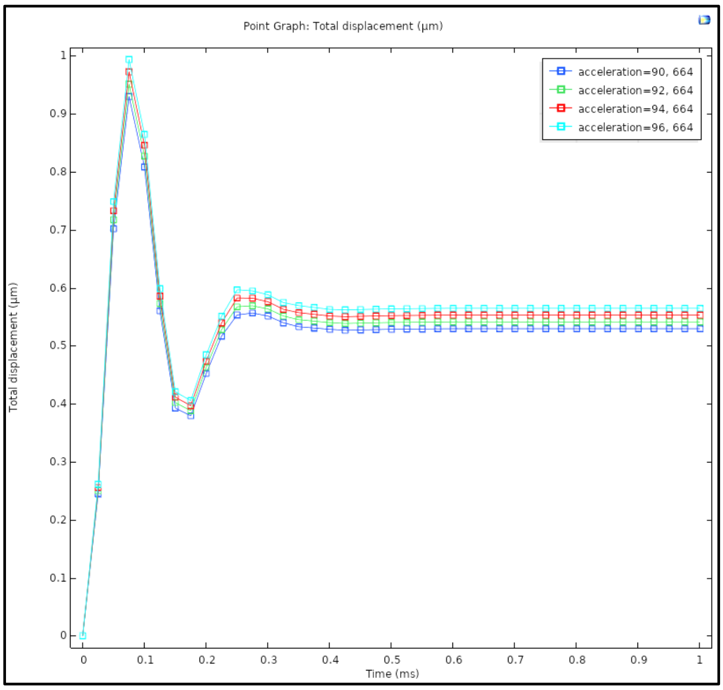

Figure 4.26 Time response of the 2-D device high range of acceleration

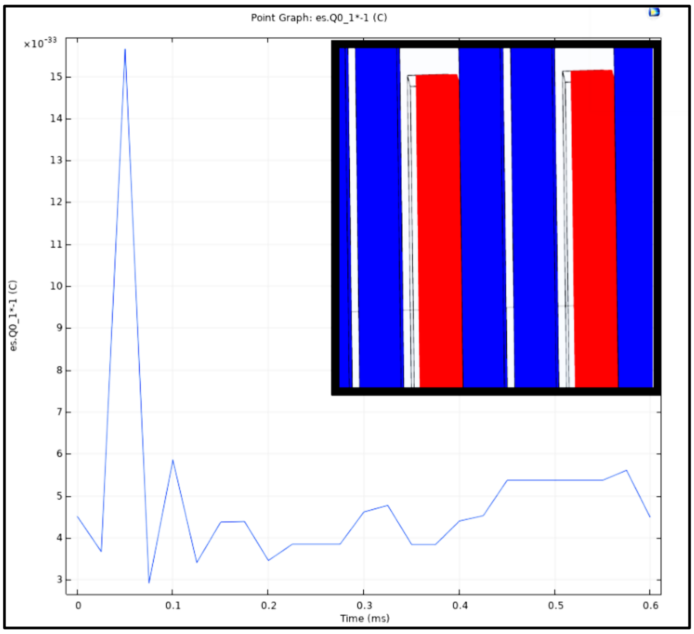

Figure 4.27 Capacitance vs. time in case of very high acceleration. Inset is the snapshot of the 2-D device fingers at the collapse

The highest acceleration that can be measured before the device gets damage is the acceleration that causes the full displacement. That causes short circuit between the moving fingers and the fixed fingers. From the figure 4.26, when the acceleration is 96 g, the excessive displacement equal to 1 micrometer, which causes the device to get damage and the capacitance equal to zero as shown in Figure 4.27.

4.4.6 Frequency response of 2-D accelerometer

Frequency response is done to estimate the device sensitivity and frequency to applied acceleration input. Acceleration from 0g to 50g with step of 10g is applied on the 2-D accelerometer with frequency by using frequency domain in COMSOL Multiphasics 5.5. Because of the beams Lx, L_Y are equal lengths, then the same responses for the x and y axes. Figure 4.28 is the simulation results.

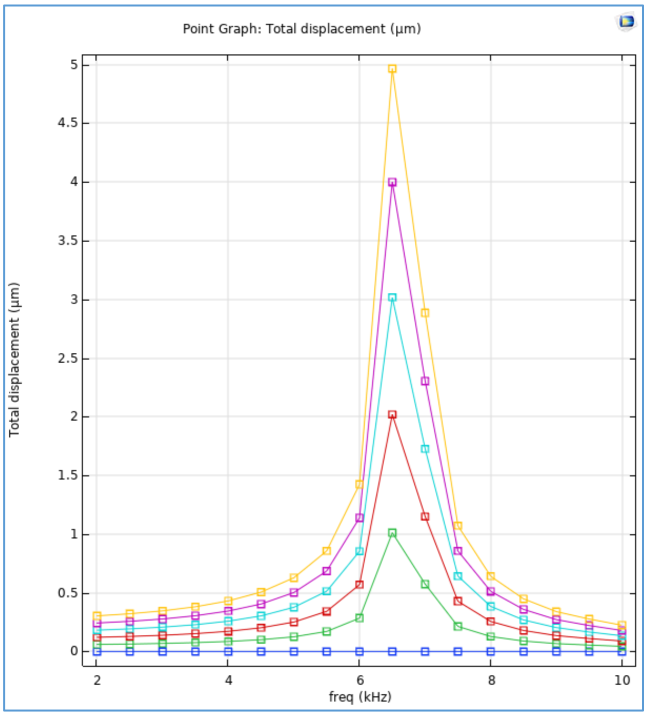

Figure 4.28 Frequency response of 2-D accelerometer

From figure 4.28 the center frequency equal to 6.5 kHz with band width approximately 1000 ∓100 Hz.

4.4.7 Output dc voltages vs. acceleration of 2-D accelerometer

Applying an alternating input voltage on the sensor fingers, for long fingers applied V_{in}, and for short fingers applied $-V_{in}$. The sensing signal is the proof-mass voltage terminal 1for x-axis terminal 2 for x-axis.

The amplitude of sensing signal depends on the amount of the acceleration. Therefore the sensing signal is considered as AM signal .To find output dc voltage using coherent detector (synchronous detector). The simplified equivalent circuit of the device for each axis is shown in figure 4.11.

The sensing signal from COMSOL Multiphasics 5.5 of 2-D model, when V_{in} is 2 V (peak voltage) is shown in figure 4.29.

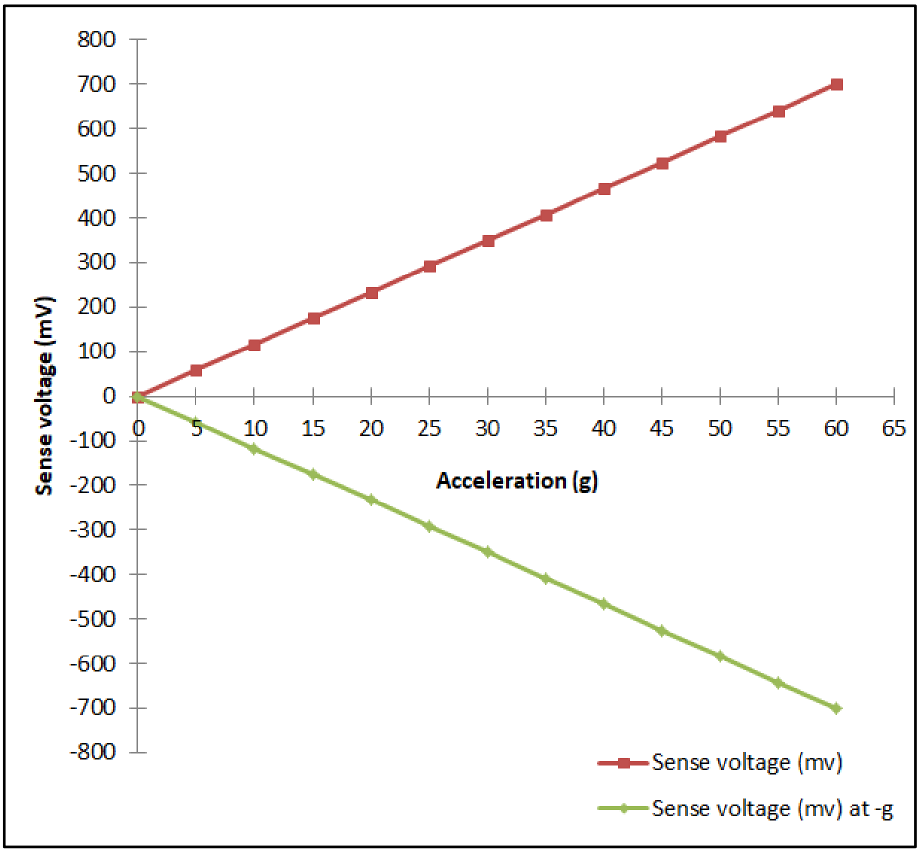

Figure 4.29 The sense voltage vs. acceleration of 2-D model

To complete the simulation result of the output dc voltage using matlab Simulink for amplifier, coherent detector circuits shown in figure 4.13. Using two circuits one for each axis. The output dc voltage vs acceleration for x or y axes is shown in figure 4.30.

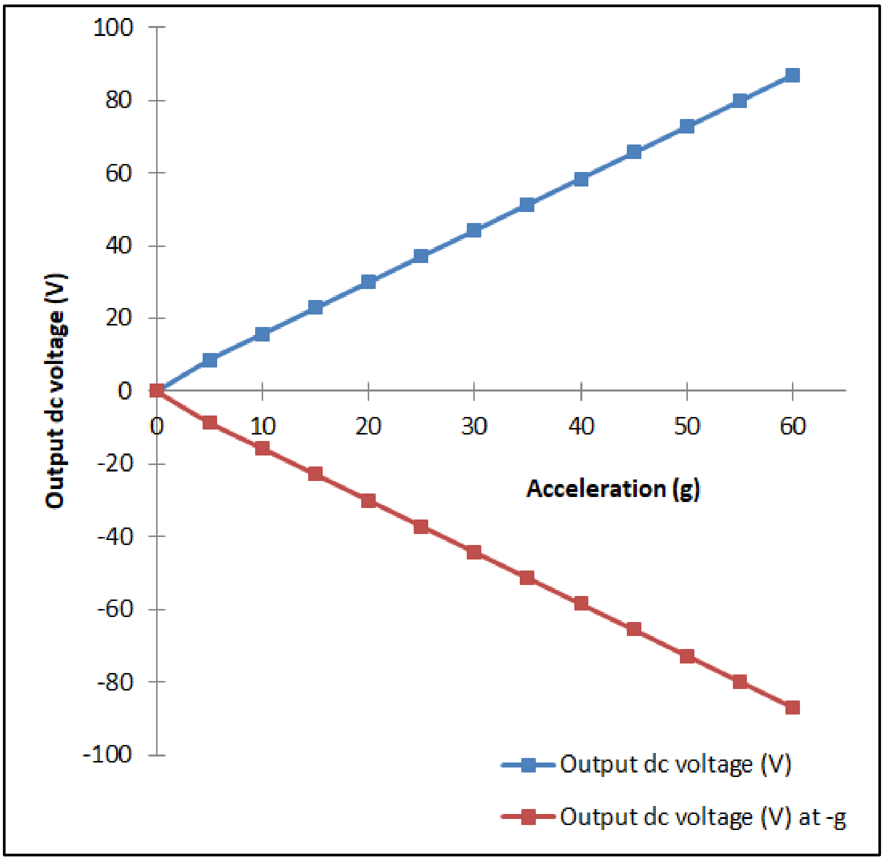

Figure 4.30 Output dc voltages vs. acceleration of 2-D accelerometer

The output dc voltage sensitivity of 2-D accelerometer is equal to 1.45 V/g.

4.5 Simulation design of the 3-D accelerometer

4.5.1 Mesh convergence study of 3-D accelerometer

Mesh convergence study of the model have the parameters shown in table 4.7.

Table 4.7 Meshes convergence study for 3-D model

Max. element (µm)	Min. element (µm)	Growth rate (µm)	Curvature factor	Resolution of narrow region	No. of element	Displacement (µm)
450	63	2	1	0.1	8091	0.004264
270	48.6	1.85	0.9	0.2	12321	0.004672
171	36	1.7	0.8	0.3	16728	0.005082
135	25.2	1.6	0.7	0.4	27190	0.005293
90	16.2	1.5	0.6	0.5	37316	0.005539
72	9	1.45	0.5	0.6	68130	0.005831
50	3.6	1.4	0.4	0.7	128191	0.005885
31.5	1.35	1.35	0.3	0.85	225938	0.005906
18	0.18	1.3	0.2	1	420753	0.005922

When an accelerations of 1g is applied to the model for different mesh according to their parameters. The proof-mass displacement was calculated for each mesh. We noticed that when the density of the mesh is increases, the displacement will be increases too, which means increasing in measurement accuracy. However, at a certain limit of the number of elements, the displacement remains constant, as shown in Figure 4.31.

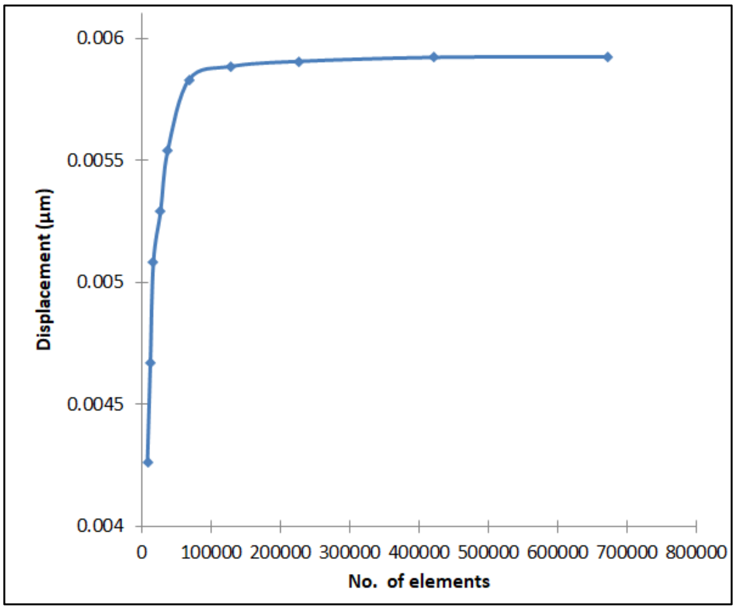

Figure 4.31 Mesh convergence simulation result of 3-D model

From figure 4.31, we can see that at a number of elements of 225938 elements and more, for the frame structure of the accelerometer, the variation in the proof mass displacements are less than 1%, and then the convergence was achieved.

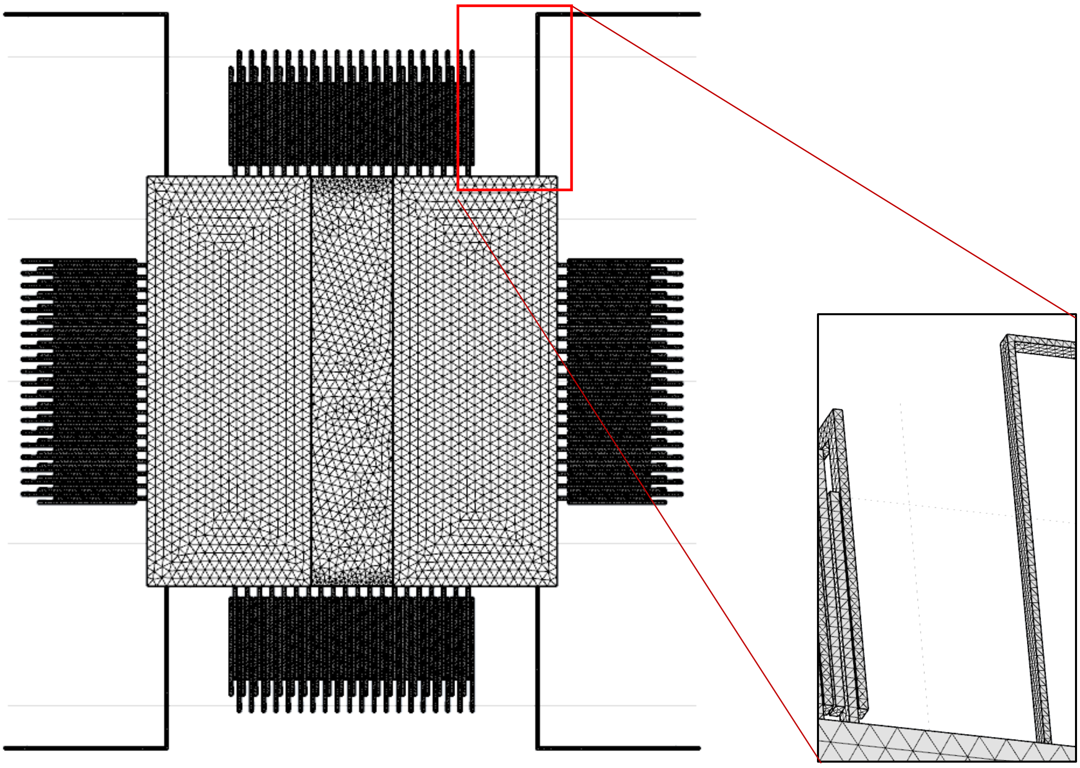

Figure 4.32 Meshed model of 3-D accelerometer structure

The shapes of the elements at mesh density of 225938 elements are tetrahedral elements as shown in figure 4.32. It is clear how elements are distributed. In the effected regions, the elements are small enough with high number of elements as in fingers and beams. While in the other ineffective regions the size of the elements are relatively bigger.

4.5.2 Acceleration vs. displacement of 3-D model

To simulate the device, acceleration ranges from 0 g to 60 g with a step of 5 g are applied and the displacements from -60 g to 0 g on the x-axis were obtained. The same procedure for the acceleration on the y-axis, and z- axis at same range, was obtained.

4.5.2.1 Acceleration on x-axis vs. displacement of 3-D model

Applying acceleration from 0 g to 60 g step 5 g on x direction as input to the model and obtain the proof- mass displacement as output, and for negative acceleration apply from -60g to 0g as input and obtain proof mass displacement as output.

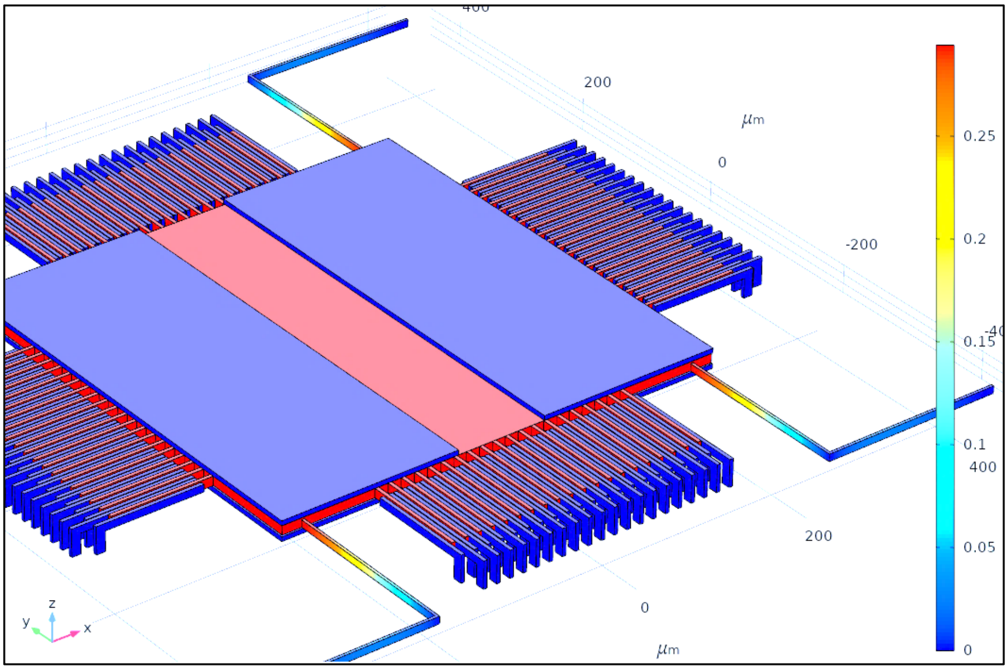

Figure 4.33 Surface displacement when acceleration on x-axis of 3-D model

Figure 4.33 is screen shoot explain the displacement of every point of accelerometer at acceleration of 60 g on the x-axis and explain gradually displacement in beams and explain in which beam the deflection occurs, note that the blue fingers are the fixed fingers and the red fingers are movable fingers. Table 4.8 and figure 4.33 is the result of simulations.

Table 4.8 Acceleration on x-axis Vs. displacement of proof-mass of 3-D model

Acceleration (g)	Displacement X (µm)	Displacement X at -g (µm)
0	0	0
5	0.029415663	-0.029415663
10	0.058831317	-0.058831317
15	0.088246956	-0.088246956
20	0.117662573	-0.117662573
25	0.147078161	-0.147078161
30	0.176493716	-0.176493716
35	0.205909229	-0.205909229
40	0.235324695	-0.235324695
45	0.264740108	-0.264740108
50	0.294155461	-0.294155461
55	0.323571007	-0.323571007
60	0.352986553	-0.352986553

The maximum displacement equal to 0.352986553 µm at apply acceleration of 60 g on x-axis

From equation 2.8

Mechanical sensitivity $S=\frac{X}{g}$

Mechanical sensitivity S= 0.005882 µm/g

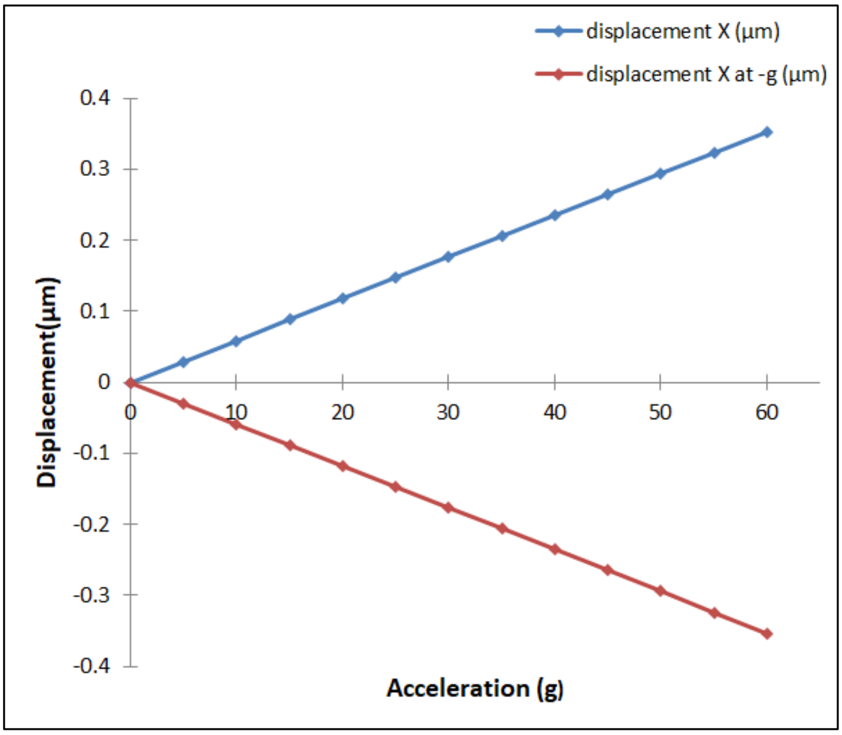

Figure 4.34 Acceleration on x-axis Vs. Proof mass displacement of 3-D model

Table 4.8 and figure 4.34 show the displacement as a function of acceleration on x-axis X= f(g) and the relationships were leaner between acceleration and proof mass displacement.

4.5.2.2 Acceleration on y-axis vs. displacement

For simulation y-axis using same procedure in x-axis and obtain the proof mass displacement. Since beams have equal lengths, the displacement is approximately equal than it was when calculating the acceleration in the x-axis direction, but the beam causing the displacement is the beam perpendicular to the direction of acceleration. As shown in the figure 4.35.

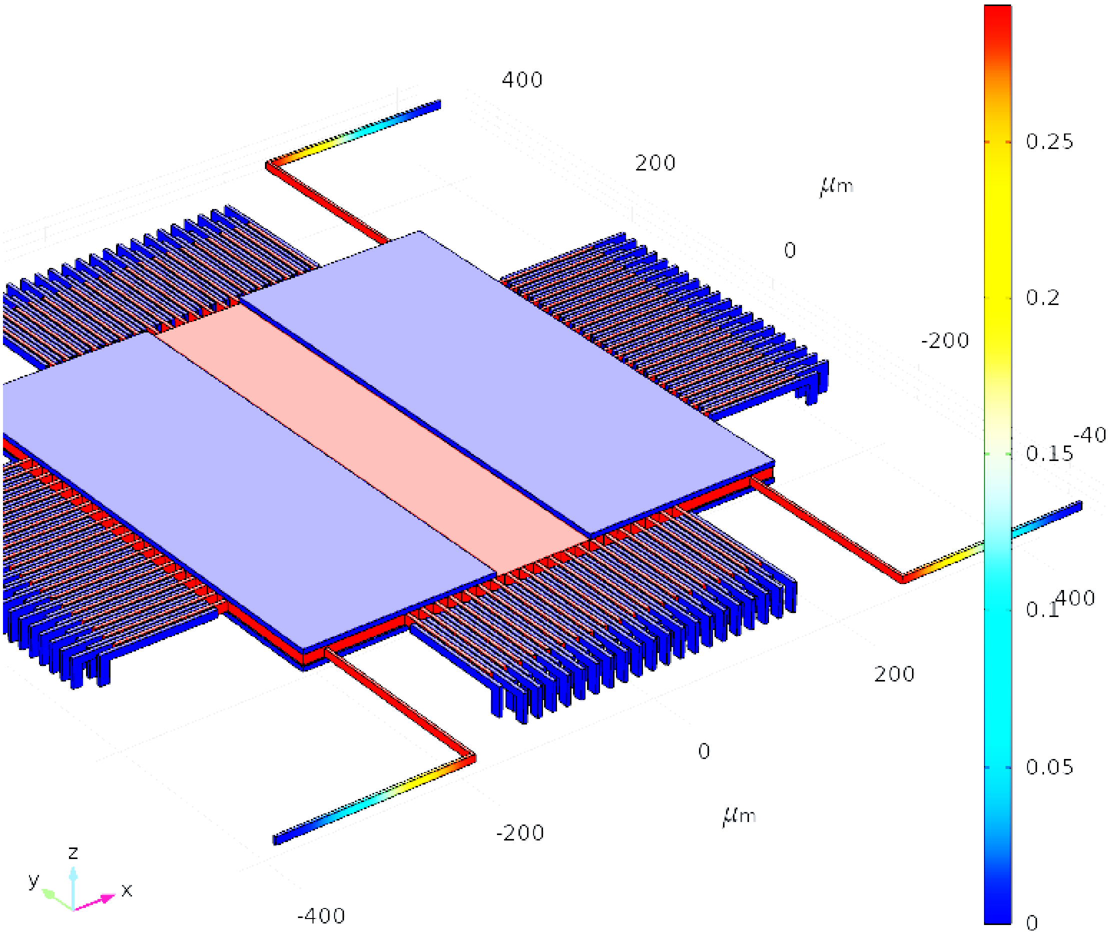

Figure 4.35 Surface displacement when acceleration on y-axis

From Figures 4.33 and 4.35 it can be seen that the beam causing the displacement is the beam perpendicular to the direction of acceleration when the direction of acceleration was in the direction of the x-axis the beam causing the displacement which the stress occurs is the perpendicular beam while the other beam stay fixed with anchor plan without any stress.

When accelerating in the direction of the y axis, the beam causing the displacement with which the stress occurs is the horizontal beam, while the other beam continues to move with the proof mass without any stress.

Table 4.9 Acceleration on y-axis vs. displacement of proof-mass of 3-D model

Acceleration (g)	Displacement y (µm)	Displacement y at -g (µm)
0	0	0
5	0.029173089	-0.029173089
10	0.058346172	-0.058346172
15	0.087519243	-0.087519243
20	0.116692294	-0.116692294
25	0.145865321	-0.145865321
30	0.175038316	-0.175038316
35	0.204211274	-0.204211274
40	0.233384189	-0.233384189
45	0.262557053	-0.262557053
50	0.291729862	-0.291729862
55	0.320903979	-0.320903979
60	0.350077068	-0.350077068

The maximum displacement equal to 0.350077068µm at apply acceleration of 60 g on the y-axis

From equation 2.8

Mechanical sensitivity $S=\frac{X}{g}$

Mechanical sensitivity S= 0.00583462 µm/g

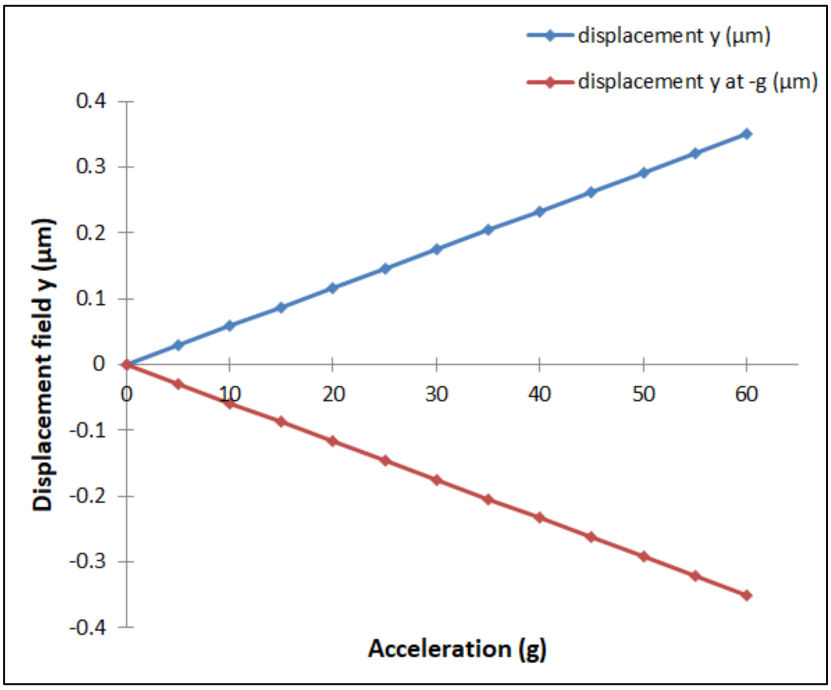

Figure 4.36 Acceleration on y-axis Vs. Proof mass displacement of 3-D model

Table 4.9 and figure 4.36 show the displacement as a function of acceleration on y-axis Y=f (g) and the relationships were linear between acceleration and proof-mass displacement.

4.5.2.3 Acceleration on z-axis vs. displacement

Apply acceleration from 0 g to 60 g step 5 g on z direction as input to the model and obtain proof mass displacement as output, and for negative acceleration apply from -60g to 0g as input and obtain the displacement as output. The results are shown in a table 4.10.

Table 4.10 Acceleration on z-axis Vs. displacement of proof-mass of 3-D model.

Acceleration (g)	**Displacement field Z (µm)**	**Displacement field Z (µm) at -g**
0	0	0
5	0.018918862	-0.018918862
10	0.037837722	-0.037837722
15	0.056756579	-0.056756579
20	0.075675434	-0.075675434
25	0.094594286	-0.094594286
30	0.113513134	-0.113513134
35	0.132431978	-0.132431978
40	0.151350817	-0.151350817
45	0.170269652	-0.170269652
50	0.189188482	-0.189188482
55	0.208107428	-0.208107428
60	0.227026344	-0.227026344

The maximum displacement equal to 0.227026344µm at apply acceleration of 60 g on the z-axis

From equation 2.8

Mechanical sensitivity $S = \frac{X}{g}$

Mechanical sensitivity S= 0.003783 µm/g

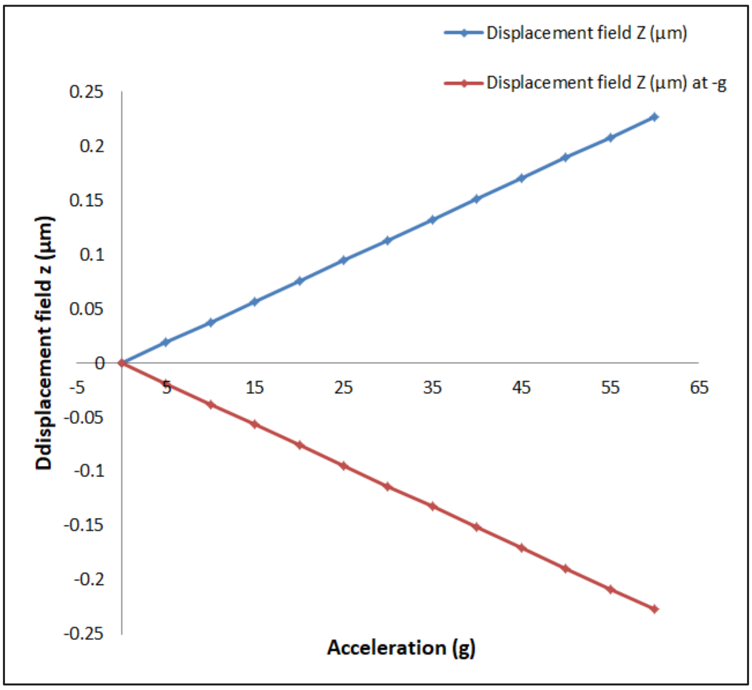

Figure 4.37 Acceleration on z-axis Vs. Proof mass displacement of 3-D model

Table 4.10 and figure 4.37 show the displacement as a function of acceleration on z-axis z=f (g) and the relationships were linear between acceleration and proof-mass displacement.

4.5.3 Acceleration vs. capacitance of 3-D model

Accelerometer Sensitivity for capacitive accelerometer is obtained from difference between two sided capacitance. The air gap between movable finger and fixed finger is 1 µm and the capacitance for two sided are equal and ΔC= 0 when applied acceleration from 0 g to 60 g step 5 g on as input to the model and obtain difference between tow sided capacitance ΔC as output, and for negative acceleration apply from -60g to 0g as input and obtain ΔC as output. Use this procedure three times for each axis x, y, and z.

4.5.3.1 Acceleration on the x-axis vs. difference of capacitance

The air gap was varied causes the capacitance in one side is increase and capacitance in other side is decrease causes ΔC increase. Table 4.11 and figure 4.38 is the simulation results.

Table 4.11 Acceleration on x-axis with capacitances and difference capacitance of 3-D model.

Acceleration (g)	**C_1 (fF)**	**C_2 (fF)**	**ΔC(fF)**	**ΔC at -g (fF)**
0	353.89	353.89	0	0
5	364.6154	343.7775552	20.83785	-20.8378
10	376.0112	334.2269862	41.78425	-41.7843
15	388.1424	325.1927314	62.94965	-62.9497
20	401.0824	316.6340259	84.44836	-84.4484
25	414.9149	308.5142861	106.4006	-106.401
30	429.7356	300.8005868	128.9351	-128.935
35	445.6543	293.4632155	152.1911	-152.191
40	462.7977	286.4752897	176.3224	-176.322
45	481.3128	279.8124277	201.5004	-201.5
50	501.371	273.4524643	227.9186	-227.919
55	523.1739	267.3751526	255.7988	-255.799
60	546.9593	261.5620969	285.3972	-285.397

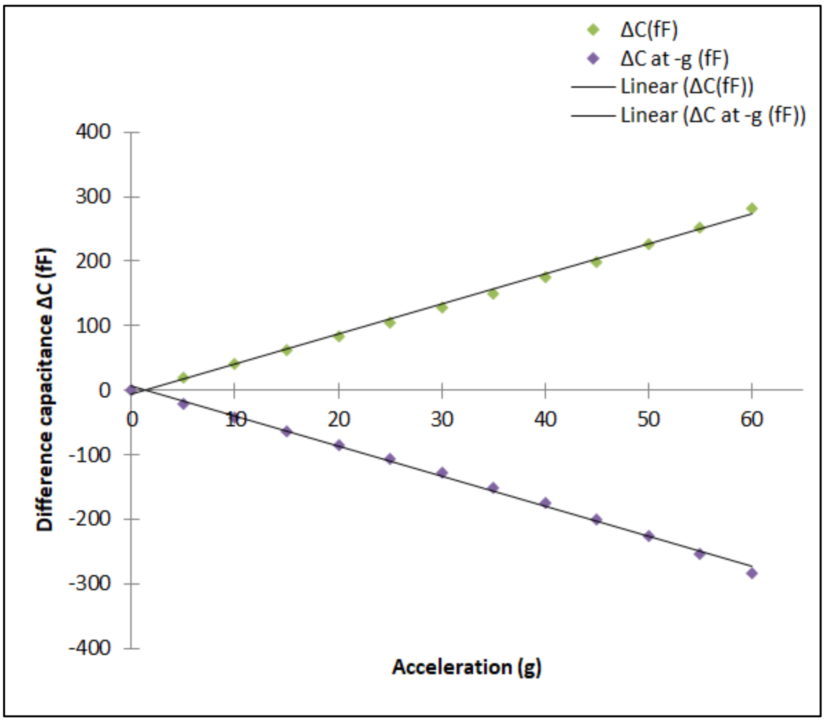

Figure 4.38 Acceleration on the x-axis vs. difference of capacitance of 3-D model

From figure 4.38 it is clear the relationship between acceleration and difference of capacitance is nonlinearity. But it is close to a linear relationship .From equation 2.15

Capacitance sensitivity $= \Delta c/g$

Capacitance sensitivity when acceleration on x-axis equal to:

Capacitance sensitivity $= 3.6478 \quad fF/g$

4.5.3.2 Acceleration on the y-axis vs. difference of capacitance

By using same procedure of simulations when acceleration on x-axis to acceleration on y-axis and obtain difference of capacitance. The results are shown in figure 4.39 and table 4.12.

Table 4.12 Acceleration on y-axis with capacitances and difference capacitance for 3-D model

Acceleration (g)	**C_1 (fF)**	**C_2 (fF)**	**ΔC(fF)**	**ΔC at -g (fF)**
0	353.89	353.89	0	0
5	364.5243	343.8585829	20.66572	-20.6657
10	375.8175	334.3801955	41.43732	-41.4373
15	387.8328	325.4103341	62.4225	-62.4225
20	400.6418	316.9091449	83.73267	-83.7327
25	414.3258	308.8408329	105.4849	-105.485
30	428.9775	301.1731576	127.8043	-127.804
35	444.7035	293.8770028	150.8265	-150.826
40	461.6263	286.9260067	174.7003	-174.7
45	479.888	280.2962441	199.5917	-199.592
50	499.654	273.9659509	225.688	-225.688
55	521.1192	267.9150079	253.2042	-253.204
60	544.5107	262.1257767	282.3849	-282.385

From equation 2.15

Capacitance sensitivity $= \Delta c/g$

Capacitance sensitivity when acceleration on y-axis equal to:

Capacitance sensitivity $= 3.612 \quad \mathrm{fF/g}$

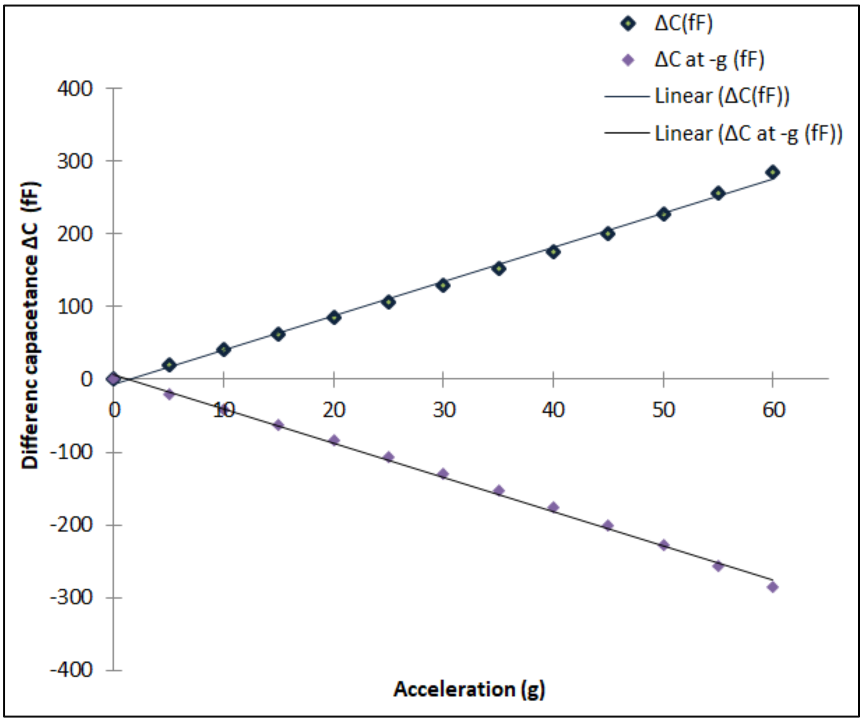

Figure 4.39 Acceleration on the y-axis vs. difference of capacitance

From figure 4.39 it is clear the relationship between acceleration and difference of capacitance is nonlinearity but it is close to a linear relationship as it is at the x-axis.

4.5.3.3 Acceleration on the z-axis vs. difference of capacitance

Repeat procedure to simulate model when acceleration direction on z-axis and obtain the difference of capacitance. The results are shown in figure 4.40 and table 4.13.

Table 4.13 Acceleration on z-axis with capacitances and difference capacitance.

Acceleration (g)	C_1 (fF)	C_2 (fF)	ΔC(fF)	ΔC at -g (fF)
0	884.7	884.7	0	0
5	901.7603	868.2732582	33.49837526	-33.49837526
10	919.4915	852.4454079	67.0687893	-67.0687893
15	937.9339	837.1842839	100.783801	-100.783801
20	957.1313	822.4599838	134.7170116	-134.7170116
25	977.131	808.2446727	168.9436061	-168.9436061
30	997.9843	794.512407	203.5409182	-203.5409182
35	1019.747	781.2389773	238.5890292	-238.5890292
40	1042.48	768.4017649	274.1714101	-274.1714101
45	1066.25	755.9796141	310.3756179	-310.3756179
50	1091.129	743.9527153	347.2940594	-347.2940594
55	1117.197	732.3024257	385.025084	-385.025084
60	1144.541	721.0114146	423.6731501	-423.6731501

From equation 2.15

Capacitance sensitivity $= \Delta c/g$

Capacitance sensitivity when acceleration on z-axis equal to:

Capacitance sensitivity $= 6.9458 \quad \mathrm{fF/g}$

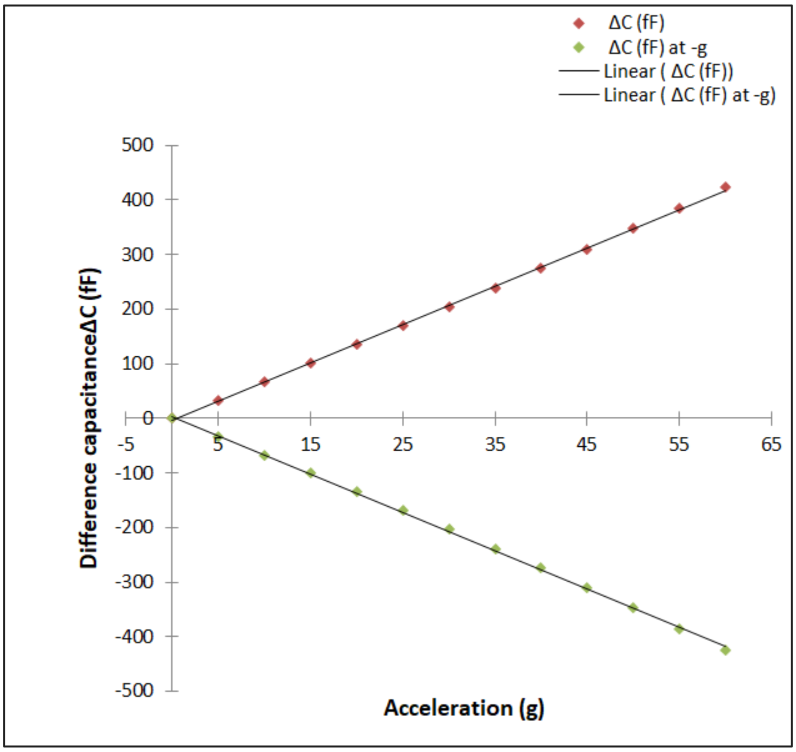

Figure 4.40 Acceleration on the Z-axis vs. difference of capacitance

From figure 4.40 it is clear the relationship between acceleration and difference of capacitance is nonlinearity but it is close to a linear relationship as it is at the x-axis and y-axis.

4.5.4 Bending stress of 3-D accelerometer

4.5.4.1 Bending stress for x-axis of 3-D accelerometer

An acceleration 0f 60 g in the direction of the x-axis is applied to the model. The stress was as shown in Figure 4.41.

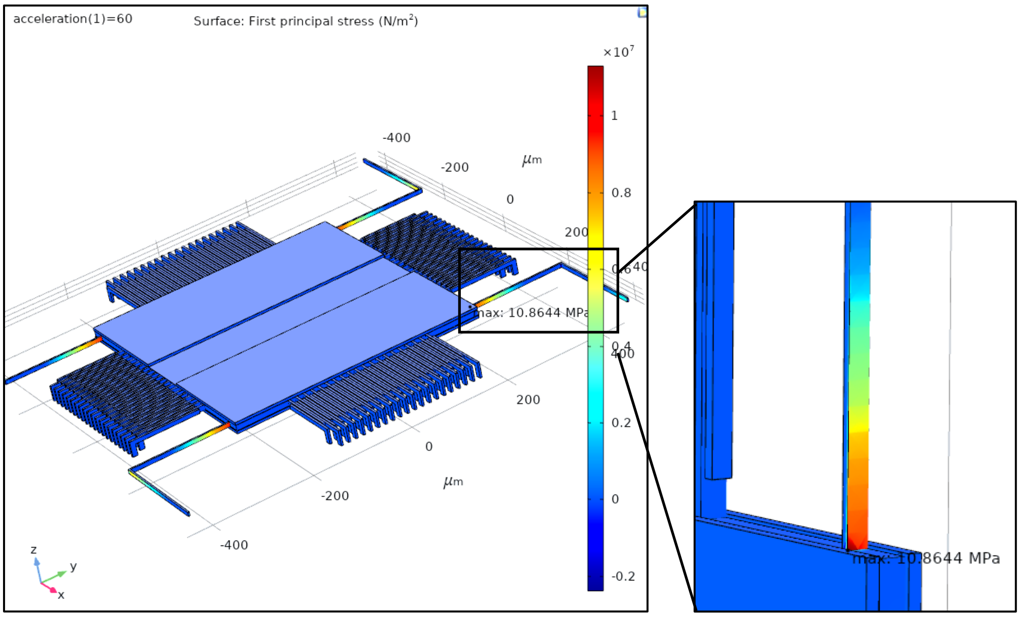

Figure 4.41 Bending stress for x-axis of 3-D accelerometer

From simulation the maximum stress occurs at the point of contact the proof mass with the beam as shown in figure. 4.41. The magnitude of maximum stress is 10.8644 MPa. It is very low in relation to UTS is 7000 MPa, which makes the safety factor high.

4.5.4.2 Bending stress for y-axis of 3-D accelerometer

When an acceleration of 60 g along the y-axis was applied to the model, the stress was as shown in Figure 4.42.

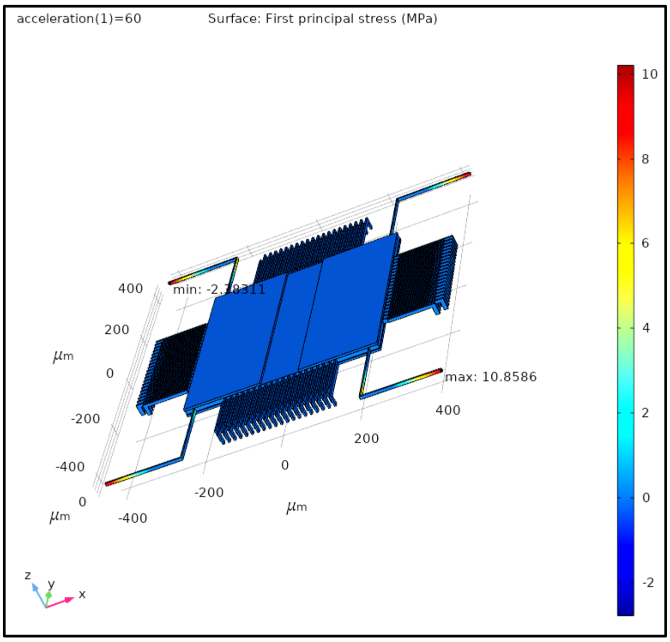

Figure 4.42 Bending stress for y-axis of 3-D accelerometer

From simulation the maximum stress occurs at the point of contact the beam with the anchor plan as shown in Figure 4.42. It is opposite when simulation the acceleration on x-axis. The magnitude of maximum stress is 10.8586 MPa at acceleration of 60 g. It is very low in relation to UTS is 7000 MPa, which makes the safety factor high as when simulation the x-axis.

4.5.4.3 Bending stress for z-axis of 3-D accelerometer

When an acceleration 0f 60 g in the direction of the z-axis is applied to the model. The stress was as shown in Figure 4.43.

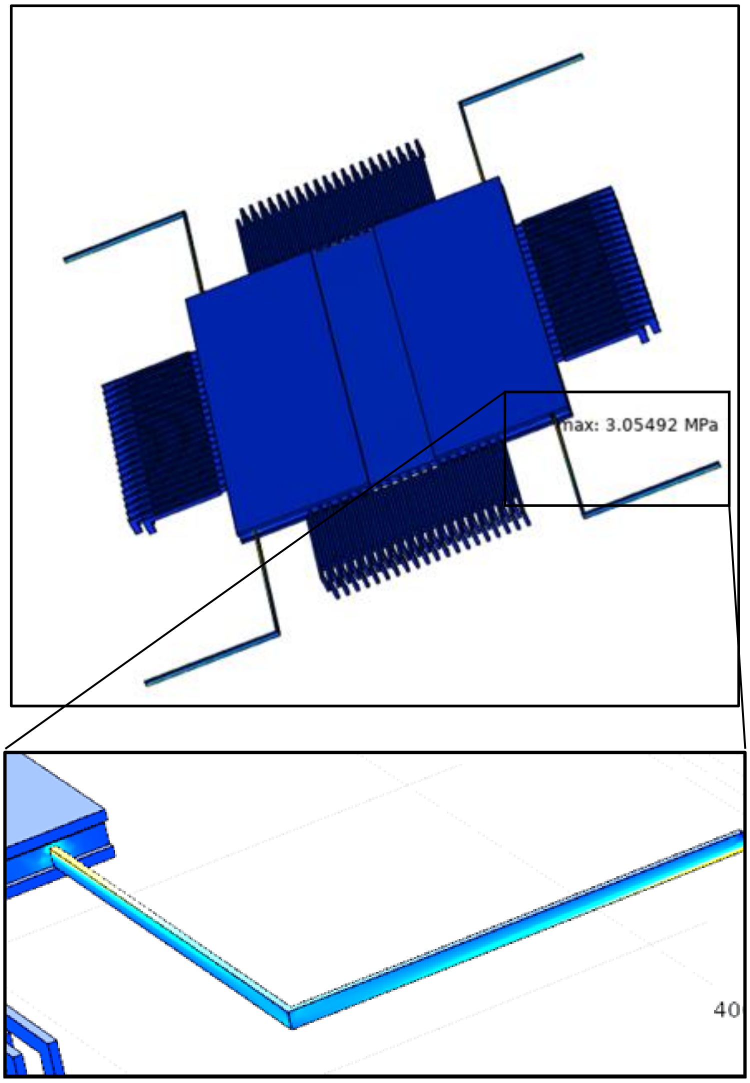

Figure 4.43 Bending stress for z-axis of 3-D accelerometer

From simulation the maximum stress occurs at the point of contact the proof mass with the beam as shown in figure 4.43. The stress is concentrated on the upper surface of the first beam and the lower surface of the second beam. The magnitude of maximum stress is 3.0549 MPa.

4.5.5 Time response of 3-D accelerometer

Time response is done to estimate the device transient analysis to the applied acceleration input

.

4.5.5.1 Time response of low range acceleration input

Low range acceleration (0.01g-0.5g) is applied on the structure to measure rising time, damping ratio, and resolution. In a time from 0 s to 1.2 ms. with step 0.025 ms for x-axis and y-axis. A time from 0 s to 1s step 0.015 ms for z-axis by using time-dependent in COMSOL Multiphasic 5.5 the results are shown in figure 4.44 for acceleration on x and y axis, and figure 4.45 for acceleration on the z-axis.

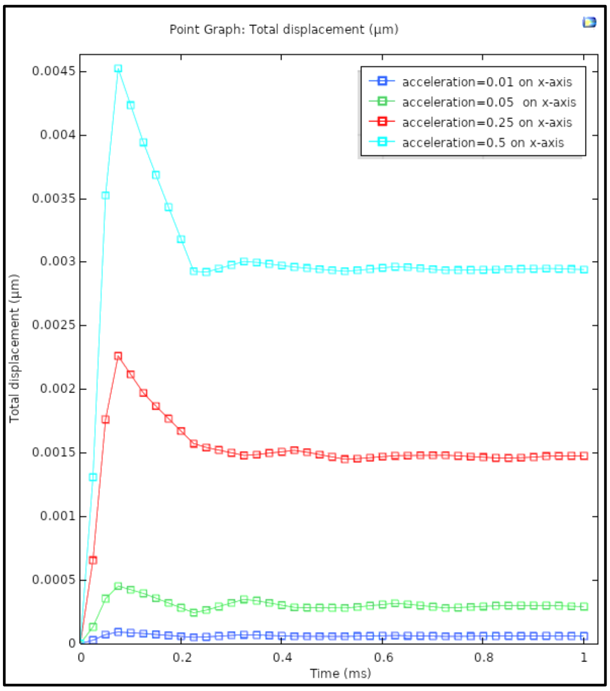

Figure 4.44 Time response of low range acceleration input on x and y axis of 3-D accelerometer

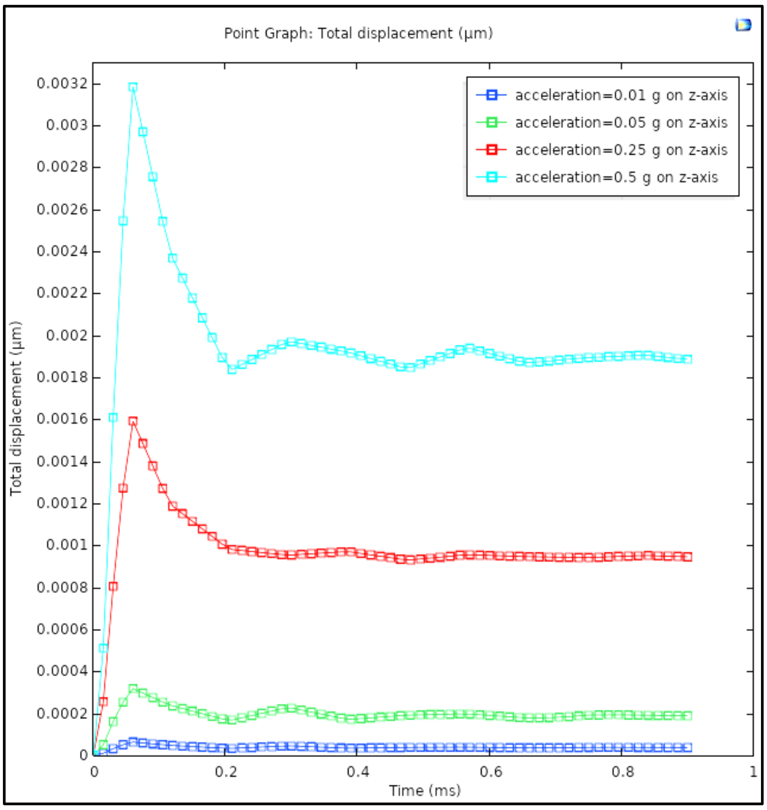

Figure 4.45 Time response low range acceleration input on z-axis of 3-D accelerometer

From figure 4.44 obtain

$\xi = 0.2251$

$w_n = 42980.32$ rad/s

And the rise time for x and y axes =0.035 ms

Referring with Figure 4.45 obtain

$\xi = 0.2$

$w_n = 48073.4$ rad/s

And the rise time for z-axis =0.035 ms

Device has minimum resolution approximately 0.05 g

4.5.5.2 Time response of high range acceleration input

High range acceleration input (90 g-96 g) on the x and y axes are applied on the structure to measure Maximum value of acceleration on x and y axis before the device gets a damaged. High range acceleration input (145 g - 165 g) on the z-axis is applied on the structure to measure Maximum value of acceleration on the z-axis before the device gets a damaged. In a time from 0 s to 1.2 ms. with stage 0.025 ms by using time-dependent in COMSOLMultiphysics 5.5. The result is shown in figure 4.46 for acceleration on x and y axis and figure 4.47 for acceleration on the z-axis.

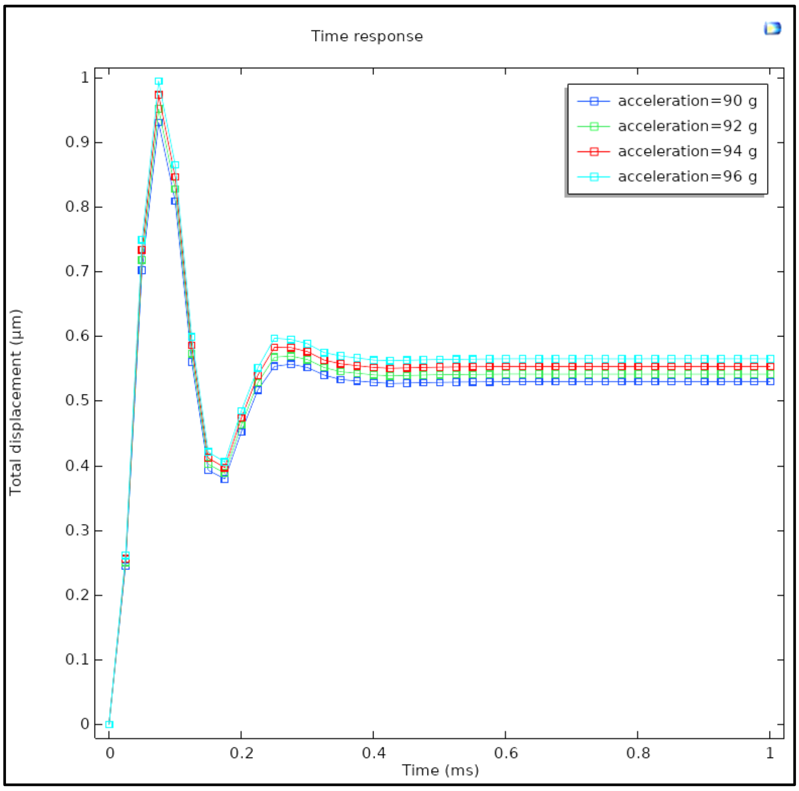

Figure 4.46 Time response of high range acceleration input on x and y axis of 3-D accelerometer

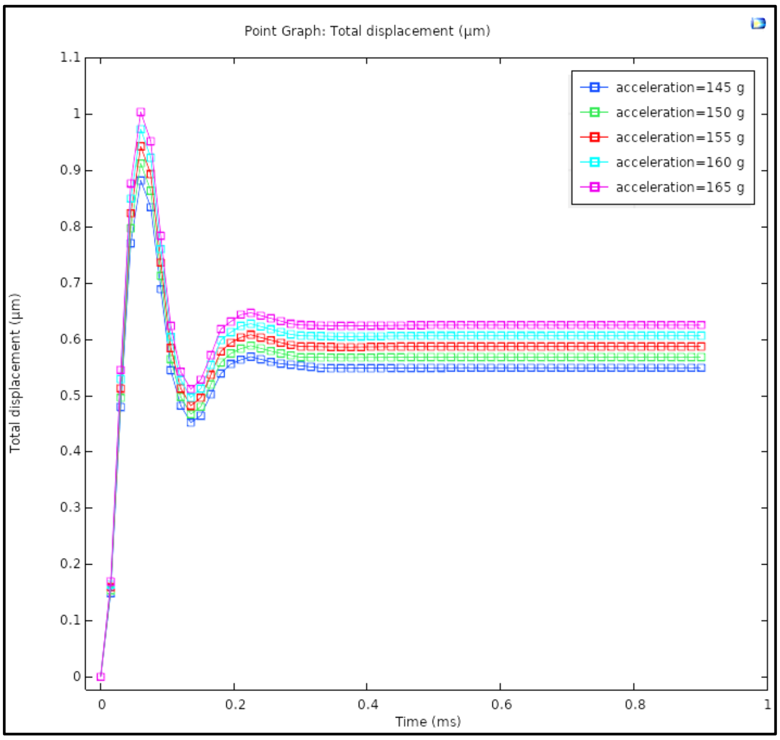

Figure 4.47 Time response of high range acceleration input on z-axis of 3-D accelerometer

The Maximum value of acceleration on x and y axis can be measured before the device gets a damaged is 96 g. The Maximum value of acceleration on z-axis can be measured before the device gets a damaged is 165 g.

4.5.6 Frequency response of 3-D accelerometer

Frequency response is done to estimate the device sensitivity with frequency to applied acceleration input. Acceleration from 0g to 50g on x, y, and z-axes with step of 10g is applied on the 3-D accelerometer using frequency domain in COMSOL Multiphasics 5.5. Because of the beams Lx, L_Y are equal lengths, then the same responses for the x and y axis. Figure 4.48 is the simulation results for x and y axes and figure 4.49 for z-axis.

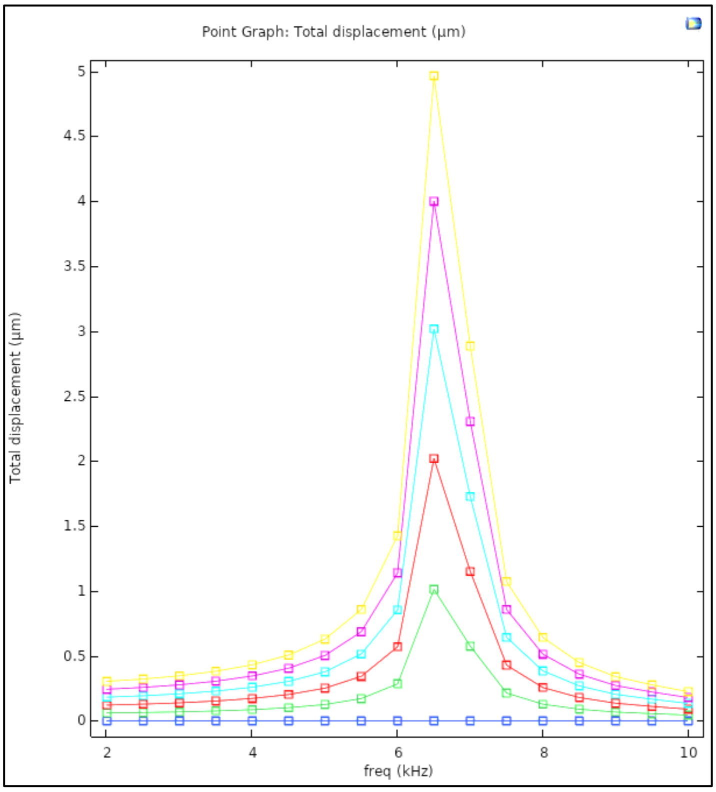

Figure 4.48 Frequency response of 3-D accelerometer for x and y axes

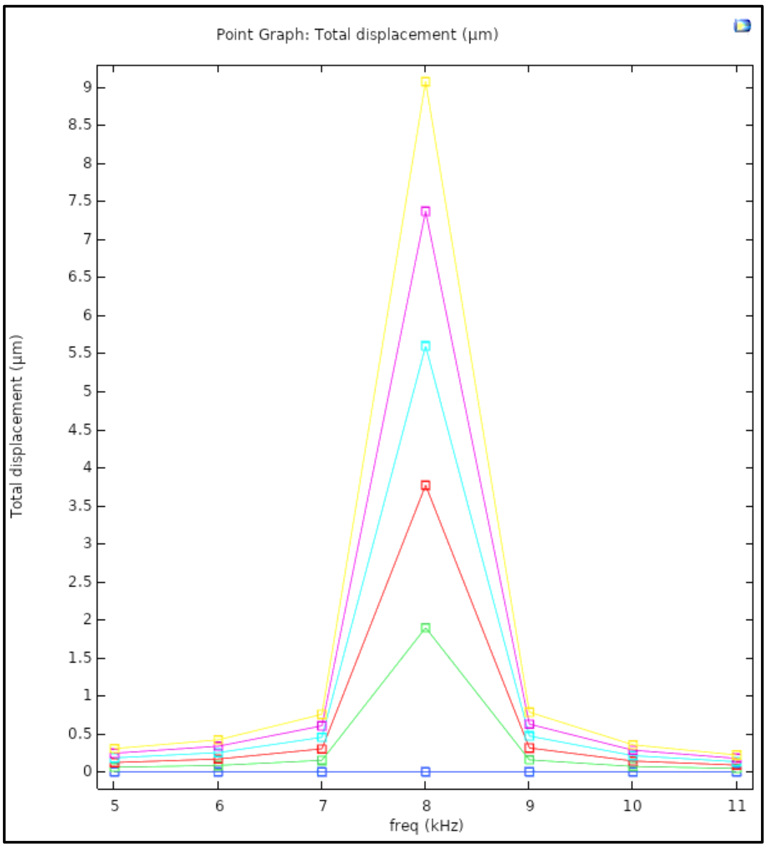

Figure 4.49 Frequency response of 3-D accelerometer for z-axis

From figure 4.48, the center frequency equal to 6.5 kHz with band width approximately 1000 ∓100 Hz for x and y axes. From figure 4.49, the center frequency equal to 8 kHz with band width approximately 1000 ∓100 Hz for z-axis.

4.5.7 Output dc voltages vs. acceleration of 3-D accelerometer

Applying an alternating input voltage on the sensor fingers, for long fingers applied V_{in}, and for short fingers applied $-V_{in}$. The sensing signal is the proof-mass voltage terminal 1for x-axis, terminal 2 for y-axis. Applying an alternating input voltage on the sensor electrodes, for top electrodes applied V_{in}, and for bottom electrodes applied $-V_{in}$. The sensing signal is the proof-mass voltage terminal 3 for z-axis. Figure 4.50 is the simulation results of x and y axes and figure 4.51 for z-axis.

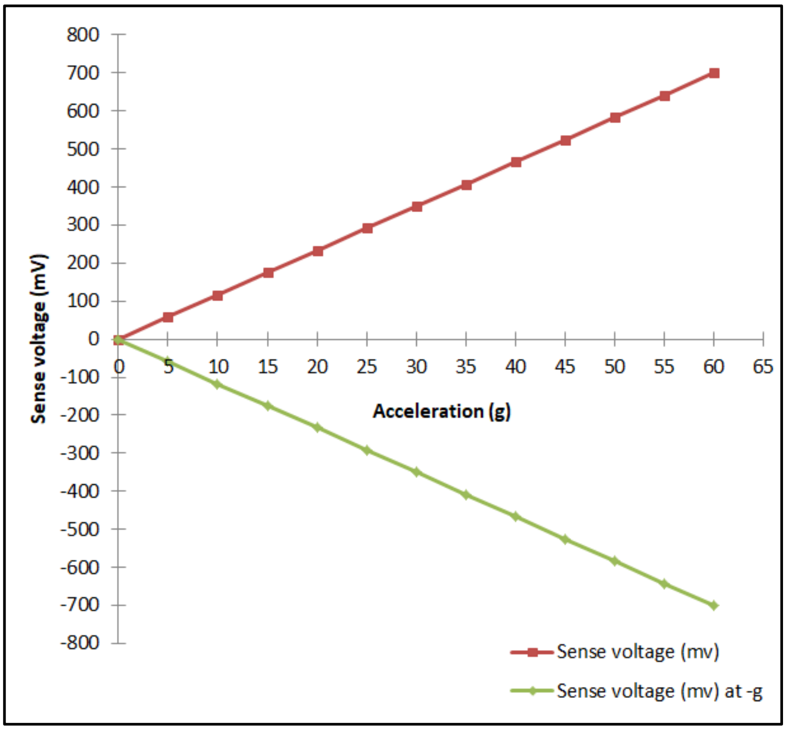

Figure 4.50 The sense voltage vs. acceleration of 3-D model for x and y axes

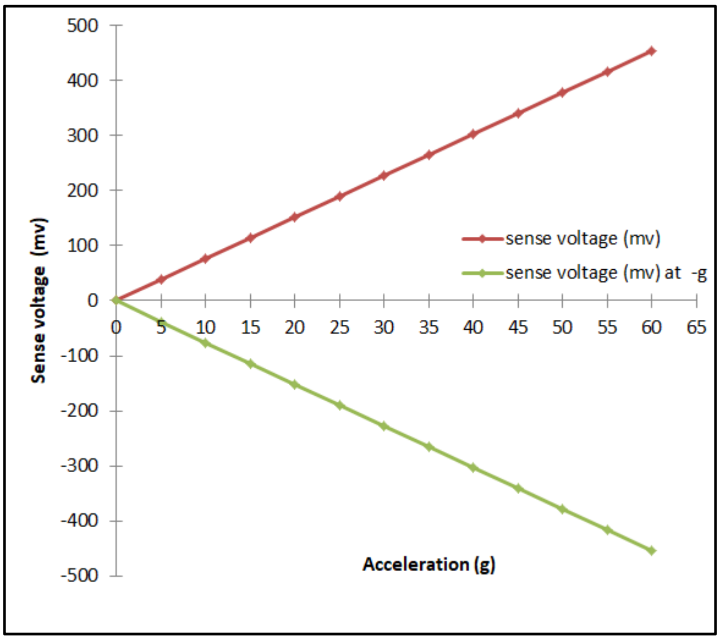

Figure 4.51 The sense voltage vs. acceleration of 3-D model for z-axis

Three electric circuits shown in figure 4.13 are used one circuit for each axis. The inputs of the circuits are the sensing voltage above, by using Matlab simulation. Figure 4.52 is the output dc voltage for x and y axes, and figure 4.53 for z-axis.

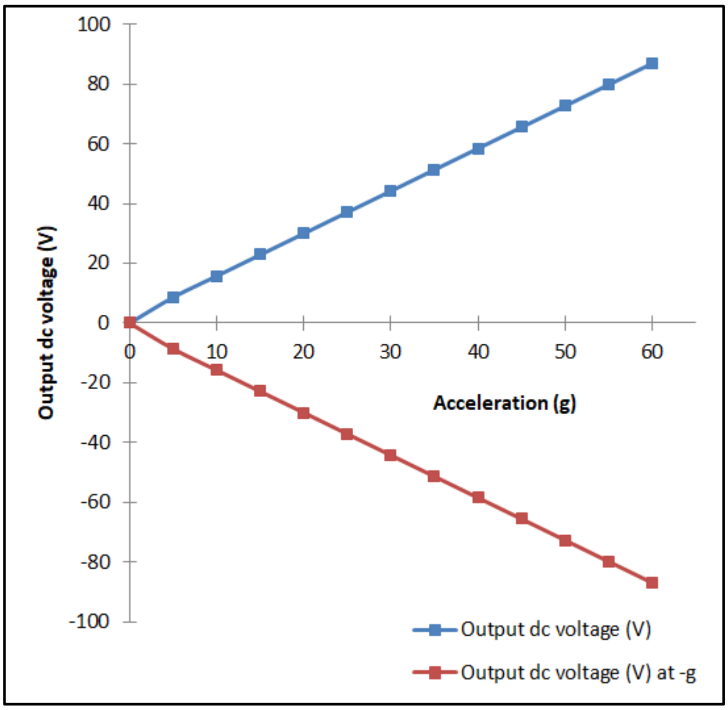

Figure 4.52 Output dc voltages vs. acceleration of 3-D accelerometer for x and y axes

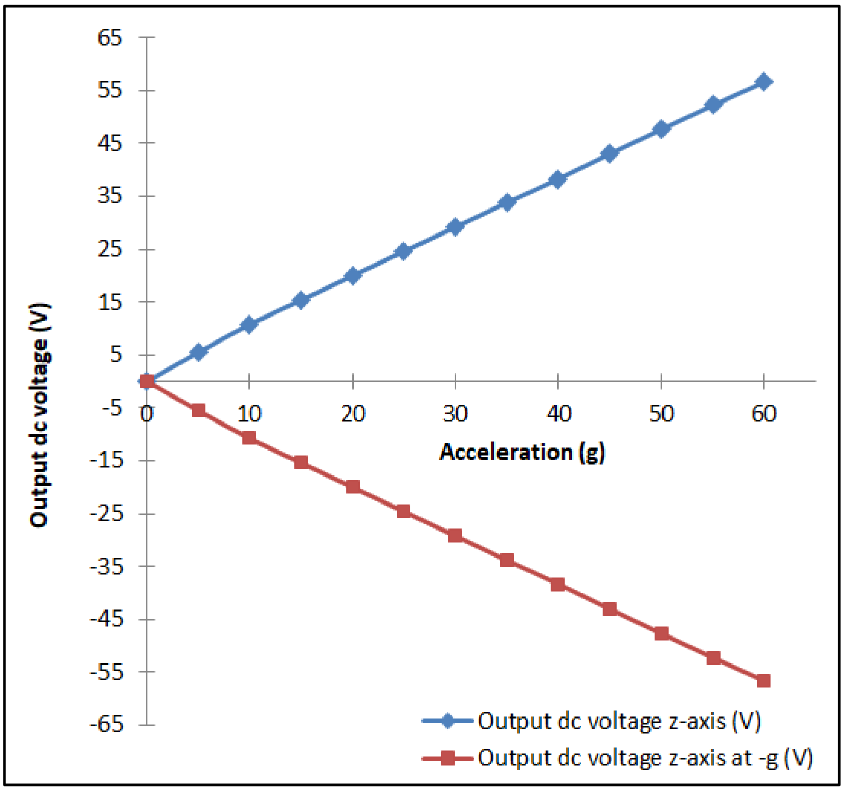

Figure 4.53 Output dc voltages vs. acceleration of 3-D accelerometer for z-axis

The output dc voltage sensitivities of 3-D accelerometer are shown in table 4.14.

Table 4.14 The output dc voltage sensitivities of 3-D accelerometer

Axes	x-axis	y-axis	z-axis
Output dc voltage sensitivities	1.45 V/g	1.45 V/g	0.94444 V/g

Table 4.15 Comparison of present accelerometer with those reported in the literature of the surface accelerometer

Ref.	Year	Device Size [mm × mm]	Range X, Y, Z [±g]	Sensitivity X, Y, Z
[19]	**2013**	**0.4×0.3**	10	1.29 fF /g, 0.1555 µm/g
[38]	**2015**	12 × 7	**10** **10** +12,-7	
[11]	**2018**	**3.95×6.55**	2.85, 2.94, 4.03	13.15 fF/g,701 mV/g 0.85 fF/g, 496 mV/g 0.31 fF/g,680 mV/g
[36]	**2020**	1.4 × 1.4	5	35nm/ g, 5.3mV g
[10]	**2021**	0.1×0.1	Crash at	4.87V, 3.14fF/g
This study 1-D	**2022**	6.2 × 5.3	60	5.436nm/ g, 2.418 fF/g, 0.607 V/g
This study 2-D	**2022**	1.2×1	60 60	5.88nm/ g, 3.6478 fF/g, 1.45V/g 5.88nm/ g, 3.6478 fF/g, 1.45V/g
This study 3-D	**2022**	1.2×1	60 60 60	5.882nm/ g, 3.612 fF/g, 1.45 V/g 5.882nm/ g, 3.6412 fF/g, 1.45 V/g 5.436nm/ g, 6.9458fF/g, 0.944 V/g

5

Chapter Five

CONCLUSION & FUTURE WORK

CHAPTER FIVE

CONCLUSION & FUTURE WORK

5.1 Conclusion

- This work adopted a dimension adjustment technique to improve the characteristics of a proposed MEMS accelerometer. The method of optimizing the spacing between fingers displays a low mechanical sensitivity but high capacitive sensitivity. While the method of adjusting the overlapping area revealed high mechanical sensitivity but low capacitive sensitivity. This indicates that the use of the first method is more applicable than the second method.

- Results demonstrated the impact of the proof mass dimension and fingers spacing upon the accelerometer properties, particularly its sensitivity. However, the improvement in the device sensitivity is limited by the linearity of the three models.

- The output signal from the device is AM signal. But we cannot use envelop detector, because this technique is unipolar, that is the output voltage would be only positive acceleration value. Therefore, coherent technique was used to obtain both positive and negative acceleration outputs.

5.2 Future work

- Devices fabrication using microfabrication technology.

- Constructing a practical testing setup to measure all parameters which obtained from fabrication and compared with the simulation results.

- Modification of the structure of the innovative devices in this thesis to obtain better results.

- Modification of the electronic circuit used in this work to obtain more suitable output voltage sensitivity and a smaller size.

REFERENCES

References

1. Rakhmatulin, A.S. and V. Popov. Integral microaccelerometer based on GaAs/InAs. in 2019 International Seminar on Electron Devices Design and Production (SED). 2019. IEEE.
2. Srivastava, S., Unit-10 Sensors. 2021, Indira Gandhi National Open University, New Delhi.
3. Parmar, Y., et al., Characterization of SOI technology based MEMS differential capacitive accelerometer and its estimation of resolution by near vertical tilt angle measurements. 2020. 26(3): p. 701-706.
4. Karlgaard, C.D., J. Tynis, and C. O'Farrell. Reconstruction of the Advanced Supersonic Parachute Inflation Research Experiment Sounding Rocket Flight Test. in 2018 Atmospheric Flight Mechanics Conference. 2018.
5. Gomathi, K., et al., Design, Fabrication, and Performance Analysis of Intelligent Mesoscale Capacitive Accelerometer for Vibration Measurement. 2020. 49(4).
6. Dadhich, T. and S. Gupta. Detecting Aggressive Driving Behavior Using Spectral Kurtosis and MEMS Accelerometers. in Proceedings of the Second International Conference on Information Management and Machine Intelligence. 2021. Springer.
7. Liu, S.Q., et al., A wearable flow-MIMU device for monitoring human dynamic motion. 2020. 28(3): p. 637-645.
8. Martínez, J., D. Asiain, and J.R.J.S. Beltrán, Lightweight Thermal Compensation Technique for MEMS Capacitive Accelerometer Oriented to Quasi-Static Measurements. 2021. 21(9): p. 3117.

9. Pieri, F., et al., Is consumer electronics redesigning our cars?: Challenges of integrated technologies for sensing, computing, and storage. 2018. 7(5): p. 8-17.
10. Santosh, G.S.K., et al., Design and simulation of spinning wheel type crash sensor for the airbag system in car. 2018. 7(1.5): p. 7-12.
11. Mohammed, Z., et al., An optimization technique for performance improvement of gap-changeable MEMS accelerometers. 2018. 54: p. 203-216.
12. Szermer, M., et al., A Capacitive 3-Axis MEMS Accelerometer for Medipost: A Portable System Dedicated to Monitoring Imbalance Disorders. 2021. 21(10): p. 3564.
13. Liu, Y., Y. Xiao, and Q.J.I.E.E. Fu, A low power consumption inverter-based ΣΔ interface for capacitive accelerometer. 2018. 15(1): p. 20171152-20171152.
14. He, J., et al., Structural designing of a MEMS capacitive accelerometer for low temperature coefficient and high linearity. 2018. 18(2): p. 643.
15. Wood, N., Characterization and Measurement Circuit Design for a Novel Low Noise and High Sensitivity MEMS Capacitive Accelerometer. 2018.
16. Ruzza, G., et al., Thermal compensation of low-cost MEMS accelerometers for tilt measurements. 2018. 18(8): p. 2536.
17. Alfaifi, A., et al., In-plane high-sensitivity capacitive accelerometer in a 3-D CMOS-compatible surface micromachining process. 2018. 28(1): p. 14-24.
18. Fic, K., et al., Sustainable materials for electrochemical capacitors. 2018. 21(4): p. 437-454.

19. Wong, W.C., I.A. Azid, and B.Y.J.S.v.-J.o.M.E. Majlis, Theoretical analysis of stiffness constant and effective mass for a round-folded beam in MEMS accelerometer. 2011. 57(6): p. 517-525.
20. Benmessaoud, M. and M.M.J.M.t. Nasreddine, Optimization of MEMS capacitive accelerometer. 2013. 19(5): p. 713-720.
21. Jun, J., et al., An SC Interface With Programmable-Gain Embedded $\Delta\Sigma $ ADC for Monolithic Three-Axis 3-D Stacked Capacitive MEMS Accelerometer. 2017. 17(17): p. 5558-5568.
22. Xu, W., et al., Design and fabrication of a slanted-beam MEMS accelerometer. 2017. 8(3): p. 77.
23. Mohammed, Z., I.A.M. Elfadel, and M.J.M. Rasras, Monolithic multi degree of freedom (MDoF) capacitive MEMS accelerometers. 2018. 9(11): p. 602.
24. Sarode, N., et al., Implementation of Time based 3-Axis Capacitive Accelerometer using COMSOL Multiphysics.
25. Ganji, B.A. and K.D.J.I.M. Hemmati, A New Design and Optimization of a Three-Axis MEMS Capacitive Accelerometer with High Dy-namic Range and Sensitivity. 2020. 50(1): p. 55-66.
26. Wang, Y., X. Zhao, and D.J.S. Wen, Fabrication and Characteristics of a Three-Axis Accelerometer with Double L-Shaped Beams. 2020. 20(6): p. 1780.
27. Benmoussa, N., et al., Design and modeling of a three-axis piezoresistive microelectronic accelerometer. 2014. 55: p. 106-112.
28. Hari, K., et al., Out-of-plane dual flexure MEMS piezoresistive accelerometer with low cross axis sensitivity. 2018. 24(5): p. 2437-2444.

29. Gesing, A.L., et al., Middle ear ossicular chain vibration detection by means of an optimized MEMS piezoelectric accelerometer. 2018. 19(6): p. 2079-2086.
30. Wang, Y.-H., et al., A paper-based piezoelectric accelerometer. 2018. 9(1): p. 19.
31. Haub, M., et al. Novel Design of an Extremely Miniaturized Accelerometer Based on Quantum Tunneling Effect. in Multidisciplinary Digital Publishing Institute Proceedings. 2018.
32. Yang, B., et al., Design of a Micromachined Z-axis Tunneling Magnetoresistive Accelerometer with Electrostatic Force Feedback. 2019. 10(2): p. 158.
33. Li, R.-J., et al., Development of a high-sensitivity optical accelerometer for low-frequency vibration measurement. 2018. 18(9): p. 2910.
34. Afshar, B.H. and M.J.J.O.L. Digonnet, Compact diaphragm-based optical accelerometers with μg/√ Hz resolution. 2020. 45(14): p. 3933-3936.
35. Terzioglu, Y., et al. A capacitive MEMS accelerometer readout with concurrent detection and feedback using discrete components. in 2014 IEEE/ION Position, Location and Navigation Symposium-PLANS 2014. 2014. IEEE.
36. Utz, A., et al., A high-precision and high-bandwidth MEMS-based capacitive accelerometer. 2018. 18(16): p. 6533-6539.
37. Preeti, M., et al., Analysis of a Proof mass Structure of a Capacitive Accelerometer as Wearable Sensor for Health Monitoring, in Micro and Nanoelectronics Devices, Circuits and Systems. 2022, Springer. p. 315-327.

38. Hemmati, K.D. and B.A.J.M.T. Ganji, A new structure and modeling of a three-axis MEMS capacitive accelerometer with high dynamic range and sensitivity. 2021. 27(1): p. 133-143.
39. Lin, C.-H., K.-A.J.J.o.N. Wen, and Optoelectronics, Power Pad Based on Structure Stacking for Ultralow-Power Three-Axis Capacitive Sensing Applications. 2021. 16(4): p. 630-641.
40. Fernandes, J., J. Chen, and H.J.J.o.M.S. Jiang, Three-Axis Capacitive Sensor Arrays for Local and Global Shear Force Detection. 2021. 30(5): p. 799-813.
41. Ichikawa, T., et al. A 3-D Capacitive-Detection Electrode for a Single Gold Proof-Mass Three-Axis MEMS Accelerometer. in 2021 IEEE International Symposium on Inertial Sensors and Systems (INERTIAL). 2021. IEEE.
42. Mukhiya, R., et al., Design, modelling and system level simulations of DRIE-based MEMS differential capacitive accelerometer. 2019. 25(9): p. 3521-3532.
43. Rao, K., et al., A MEMS micro-g capacitive accelerometer based on through-silicon-wafer-etching process. 2019. 10(6): p. 380.
44. Gupta, N., et al., Design and fabrication of SOI technology based MEMS differential capacitive accelerometer structure. 2019. 30(16): p. 15705-15714.
45. Ghemari, Z., S.J.A.I.C. Saad, and S. Processing, Parameters improvement and suggestion of new design of capacitive accelerometer. 2017. 92(3): p. 443-451.
46. Song, S., et al., Performance improvement of miniaturized ZnO nanowire accelerometer fabricated by refresh hydrothermal synthesis. 2017. 4(9): p. 170557.

47. Son, J.-D., et al., An availability of MEMS-based accelerometers and current sensors in machinery fault diagnosis. 2016. 94: p. 680-691.
48. Sun, Y.-C., et al. Performance improvement of CMOS-MEMS Pirani vacuum gauge with hollow heater design. in 2015 Transducers-2015 18th International Conference on Solid-State Sensors, Actuators and Microsystems (TRANSDUCERS). 2015. IEEE.
49. Tsuchiya, T., et al. Thermomechanical noise of arrayed capacitive accelerometers with 300-NM-gap sensing electrodes. in 2017 19th International Conference on Solid-State Sensors, Actuators and Microsystems (TRANSDUCERS). 2017. IEEE.
50. Jankowski, M., et al. CMOS Interface for Capacitive Sensors with Custom Fully-Differential Amplifiers. in 2020 27th International Conference on Mixed Design of Integrated Circuits and System (MIXDES). 2020. IEEE.
51. Islam, M.S., et al., A digitally programmable CMOS feedback ASIC for highly stable MEMS-referenced oscillators. 2019. 66(11): p. 4158-4171.
52. Lu, C.-L. and M.-K.J.M.I. Yeh, Stress analysis of shielding electrode in chip with pressure sensor embedded in accelerometer. 2019.
53. Peng, Y., et al., Recent advancements in inertial micro-switches. 2019. 8(6): p. 648.
54. Almabrouk, H., et al., Geometry Investigation and Performance Optimization of a Single-Mass Piezoelectric 6-DOF IMU. 2020. 10(5): p. 6282-6289.

55. Cao, L.-m., et al., Research on an anchor point lever beam coupling type tuning fork micro-gyroscope. 2020. 21(6): p. 1099-1111.
56. Karpman, M., A High-Performance Tunneling Accelerometer.
57. Nawaz, F., et al. System Model Extraction of MEMS Beam Resonator for Colpitts Crystal Oscillator. in 2020 International Conference on Engineering and Emerging Technologies (ICEET). 2020. IEEE.
58. TK, S. and S. NO, Mathematics for Engineers (Common to AL, CU and PD).
59. Joshi, P., et al. Emulation of MEMS Capacitive Sensor for CMOS Interface Circuit Validation. in 2020 IEEE 17th India Council International Conference (INDICON). 2020. IEEE.
60. Islam, M.S., Reconfigurable RF and Wireless Architectures Using Ultra-stable Micro-and Nano-electromechanical Oscillators: Emerging Devices, Circuits, and Systems. 2020, Case Western Reserve University.
61. Charan, Y.S. and A.D. Sundararajan, Integrated MEMS capacitive pressure sensor with on-chip CDC for a wide operating temperature range, in Nanoelectronic Materials and Devices. 2018, Springer. p. 61-79.

خلاصة

تم تصميم ومحاكاة وتمييزثلاث مقاييس التسارع السعوية محسنة . تم استخدام COMSOL Multiphasics5.5 لمحاكاة تشغيل الجهاز. أظهر العمل كيفية تحسين الحساسية السعوية لمقياس التسارع من خلال تحسين أبعاد كتلة الإثبات واصابع الاستشعار للهيكل المصمم. ومع ذلك ، لاحظنا أن تحسين الحساسية السعوية بهذه الطريقة مقيد بخطية مقياس التسارع.

النموذج أحادي البعد يبلغ طوله وعرضه وسمكه 620 ميكرومتر و 558 ميكرومتر و 30 ميكرومتر على التوالي. الجهاز لديه نسبة تخميد سريعة 0.265 ، تردد طبيعي غير مخمد 42578.4 دوره \ ثانية ، وزمن الوصول 0.05 مللي ثانية. الجهاز لديه تردد رنين مقبول 6500 هرتز وعرض نطاق من 3- ديسيبل 1200 هرتز. الجهاز بدقة 0.05 g. تم قياس حساسية جهد الخرج بتيار المستمر للنموذج احادي البعد لتكون 0.607 فولت \g أقصى تسارع تم قياسه قبل انهيار الجهاز كان 112 g

يبلغ طول النموذج ثنائي الأبعاد وعرضه وسمكه 1200 ميكرومتر و 1000 ميكرومتر و 30 ميكرومتر على التوالي. الجهاز لديه معدل التخميد السريع 0.2251 ، التردد الطبيعي الغير مخمد 42980.32 دوره / ثانية ، وزمن الوصول 0.05 مللي ثانية. الجهتاز لديه تردد رنين مقبول 6500 هرتز وعرض النطاق الترددي عند 3- ديسيبل 1200 هرتز. دقة الجهاز لكل محور وأقصى تسارع تم قياسه قبل انهيار الجهاز كان 96 g تم قياس حساسية جهد 0.05 الخرج للتيار المستمر لمقاييس التسارع ثنائية الأبعاد لتكون 1.45 فولت\g.

يبلغ طول النموذج ثلاثي الأبعاد وعرضه وسمكه 1200 ميكرومتر و 1000 ميكرومتر و 30 ميكرومتر على التوالي . الجهاز لديه نسبة التخميد سريعة 0.2251 ، التردد الطبيعي غير المخمد 42980.32 دوره\ ثانية ، وزمن الوصول 0.05 مللي ثانية للمحورين x وy. نسبة التخميد 0.2 ، التردد الطبيعي غير المخمد 48073.4 دوره\ ثانية ، وزمن الوصول 0.035 مللي ثانية للمحور z . للجهاز تردد رنين مقبول 6500 هرتز وعرض النطاق الترددي عند 3- ديسيبل 1200 هرتز للمحورين x وy ، وتردد الرنين 8000 هرتز وعرض النطاق الترددي عند 3- ديسيبل 1000 هرتز للمحور z. دقة الجهاز 0.05 g لكل المحاور وكان الحد الأقصى للتسارع الذي تم قياسه قبل انهيار الجهاز 96 g للمحورين x وy بينما كان 165 g للمحور z. تم قياس حساسية جهد الخرج المستمر لمقياس التسارع ثلاثي الأبعاد لتتكون 1.45 فولت \ g للمحورين x وy و 0.944 فولت \ g للمحور z.

جمهورية العراق
وزارة التعليم العالي والبحث العلمي
جامعة بابل
كلية الهندسة
قسم الهندسة الكهربائية

مقياس التسارع (MEMS) تصميم وتوصيف

رسالة
مقدمة الى كلية الهندسة في جامعة بابل كجزء من متطلبات نيل درجة الماجستير
في الهندسة / الهندسة الكهربائية / الكترونيك صناعي

من قبل

ادريس احمد مريعي سلمان النصاري

بأشراف
الأستاذ المساعد

د .حيدر صاحب المؤمن

1443 A.H
2022 A.D.